Title

Investigating the Importance of Condensational Heating of a Snowpack During Atmospheric Rivers at Mammoth Mountain, CA

Author

Roj, Shawn C

Publication Date

2021

Peer reviewed|Thesis/dissertation

UNIVERSITY OF CALIFORNIA SAN DIEGO

Investigating the Importance of Condensational Heating of a Snowpack During Atmospheric Rivers at Mammoth Mountain, CA

A thesis submitted in partial satisfaction of the requirements for the
Master of Science Degree

in

Earth Sciences

by

Shawn Christopher Roj

Committee in charge:

Joel Norris, Chair
Alexander Gershunov
F. Martin Ralph

2021

The thesis of Shawn Christopher Roj is approved, and it is acceptable in quality and form for publication on microfilm and electronically:

University of California San Diego

2021

DEDICATION

To my parents: Bruno and Angela Roj

And to anyone who has ever had the urge to pursue a new direction in life, do it.

EPIGRAPH

"Your work is going to fill a large part of your life, and the only way to be truly satisfied is to do what you believe is great work. And the only way to do great work is to love what you do. If you haven't found it yet, keep looking. Don't settle. As with all matters of the heart, you'll know when you find it."

Steve Jobs

"If you're laughing and smiling, you're the winner in life."

Rodney Wiley (DJ Rodney-O)

TABLE OF CONTENTS

LIST OF FIGURES

LIST OF TABLES

ABSTRACT OF THE THESIS

Investigating the Importance of Condensational Heating of a Snowpack During Atmospheric Rivers at Mammoth Mountain, CA

By

Shawn Christopher Roj

Master of Science in Earth Sciences

University of California San Diego, 2021

Professor Joel Norris, Chair

Atmospheric rivers bring warm, moist, and windy conditions to the Sierra Nevada Mountains of California. With warm air and an ample supply of water vapor flowing over an existing snowpack, condensation may occur directly on the snow possibly releasing large amounts of latent heat into the snowpack. Heat supplied to the snowpack can warm the snow and, if isothermal at 0° C, may lead to substantial snowmelt and the possibility of downstream flooding.

Full energy balance measurements at a single location are not readily available on the windward side of the Sierra where most large flooding events have occurred in the past.

Therefore, an energy balance study site, known as CUES, located on Mammoth Mountain Ski Area, California was utilized. The bulk-aerodynamic method was used to estimate turbulent heat fluxes over snow and identify times of large downward latent heat flux. When snow was present at CUES, daily mean downward latent heat flux occurred 25% of the time with a daily mean value of 3.0 W m^{-2}. An hourly composite plot of integrated water vapor transport when daily mean values of latent heat flux were greater than the 95th percentile show that the largest downward latent heat flux values occur when integrated water vapor transport is well below the typical atmospheric river threshold of 250 kg m^{-1} s^{-1}. This signifies that downward latent heat flux is not a significant source of energy into the snowpack during atmospheric rivers at CUES.

1. Introduction

An atmospheric river (AR) is a long, narrow corridor of enhanced atmospheric moisture transport (Ralph et al. 2004) that has large implications for the hydrology of the western U.S. (Dettinger et al., 2011). ARs can bring strong winds, heavy precipitation, a heightened threat of costly disasters, and have been responsible for many large flood events in the western U.S. (Dettinger et al., 2011; Henn et al., 2020; Ralph, 2006). Because ARs are typically associated with the warm sector of an extratropical cyclone, snow levels can be much higher than normal when affecting the Sierra Nevada Mountains of California. Warm ARs bring the threat of rain on snow events (Guan et al., 2016; Kim et al., 2013, Neiman et al., 2008) which have been studied extensively throughout the western U.S. (Guan et al., 2016; Jennings and Jones, 2015; Kattelmann, 1996; Li et al., 2019; Marks et al., 1998). In addition to runoff generated from the rain itself, snowmelt can add to the threat of downstream flooding. Such was the case during a series of powerful ARs that made landfall in northern California just before the Lake Oroville spillway incident (Henn et al., 2020) and helps to motive this study. Additionally, Henn et al., 2020 found that these landfalling ARs brought nearly 4 days of warm, moist, and windy conditions; enough to deplete the lower elevation antecedent snowpack of its cold content, causing massive amounts of snowmelt runoff. Marks et al., 1998, and Moore and Owens, 1984 found that warm air and condensation of water vapor directly onto the snow surface can release large amounts of sensible and latent heat into the snowpack which is then used for warming and melting snow. Many studies have shown that heat added to the snowpack from rain is negligible in comparison to other heat transfer mechanisms (Li et al., 2019; Marks et al., 1998; Prowse and Owens, 1982). However, Jennings 2015 showed that precipitation enhanced snowmelt occurred when a snowpack was close to 0° C.

Energy is transferred to the snow surface from above by radiation, precipitation, and the turbulent heat fluxes of sensible and latent heat. Both turbulent heat fluxes can introduce large amounts of energy into the snowpack. At higher elevations, and depending on the time of year, the temperature of the snowpack itself will play a large role in the amount of energy needed for substantial melt. If the snowpack is very cold, a large energy input is needed to decrease its overall cold content (Jennings et al., 2018). Once the snowpack is isothermal at 0° C, additional energy input could lead to significant snowmelt. The amount of snowmelt will depend on the magnitude of the energy flux and the length of time the snowpack was exposed to this flux. Other factors that may limit the amount of runoff include snow depth and snow density (Trubilowicz & Moore, 2017).

1.1 Surface Turbulent Heat Flux

Fluxes of sensible and latent heat compose surface turbulent heat fluxes. For the purposes of this study, SHF is the transfer of heat energy due to a difference in temperature between the air and snow surface without a phase change. LHF is a hidden heat energy that is transferred during a phase change without a change in temperature. Latent heat is heat released into the environment during condensation of water vapor or heat taken from the environment during evaporation of water or snow. Condensational heating of a snowpack, otherwise known as “dew on snow”, is achieved when the flux of latent heat, the amount of latent heat energy released or taken, is directed toward the snow. This signifies that water vapor is condensing directly onto the snow and releasing energy into the snowpack. The specific heat of dry air at constant pressure, used for calculating the SHF, is 1,004 J K^{-1} kg^{-1}. The specific heat of ice is approximately 2,100 J K^{-1} kg^{-1}. The latent heat of vaporization/condensation, used for calculating the LHF, is approximately 2.5 x

10^6 J kg^{-1}. Clearly, a LHF directed towards a snowpack will release large amounts of energy which is then used to warm the snowpack.

LHF occurs when there is a vapor pressure difference between the air and snow surface (Δe). The vapor pressure of the air is calculated from the dewpoint temperature (T_d) while the vapor pressure at the snow surface is the saturation vapor pressure at the snow surface temperature (T_{snow}). If the vapor pressure at the snow surface is greater than in the air, sublimation will occur, removing mass, transferring energy to the atmosphere, and cooling the snow surface. If the vapor pressure in the air is greater than at the snow surface, condensation will occur, adding mass, transferring energy into the snowpack, and warming the snow surface. Turbulence supplied by wind and the stability of the atmosphere near the surface control the magnitude of the LHF. Because the snow surface cannot be warmer than 0° C the saturation vapor pressure is limited to a maximum of 611.24 Pa. Therefore, large values of downward LHF (DLHF) are possible if T_d is above 0° C and relative humidity (RH) levels are large enough such that the vapor pressure above the snow surface is larger than at the snow surface.

To calculate turbulent heat fluxes for this study I used the bulk-aerodynamic (bulk) method, more fully described in Section 3. This method is still commonly used in energy balance models, especially in the hydrology community (Lapo et al., 2019). The Eddy Covariance (EC) method (Baldocchi et al., 1988) is a more direct way to measure turbulent heat fluxes. Many difficulties exist when measuring turbulent heat fluxes in complex terrain using these methods (Goulden et al., 2012; Prueger and Kustas, 2005; Reba et al., 2014; Sexstone et al., 2016). When looking at data from an EC tower in the southern Sierra, most AR days were missing turbulent heat flux data, signifying that these towers may be unreliable during stormy conditions.

1.2 Objectives

Objectives for this study are as follows:

1. Identify typical air and dewpoint temperatures during atmospheric river events in the Feather and Yuba River watersheds located in the northern Sierra Nevada Mountains of California

2. Identify the importance of condensational heating of a snowpack by estimating the downward latent heat flux during atmospheric rivers at CUES:
    - How frequently does DLHF occur?
    - How important is DLHF to the total surface energy flux (SEF)?
    - How often is DLHF the most important term in the total SEF?
    - What meteorological conditions are typically associated with DLHF?
    - Are there certain meteorological thresholds when DLHF is important?
    - How does DLHF change when temperatures are raised to be more consistent with the Feather and Yuba River watersheds?

HYPOTHESIS: Atmospheric rivers, with their warm, moist, and windy conditions, increase the likelihood of condensational heating of a snowpack that may lead to significant snowmelt, enhancing the already elevated risk of downstream flooding.

2 Data

2.1 CUES Research Facility

Meteorological measurements are extensive throughout the Sierra Nevada Mountains of California. However, it was difficult to find a location where turbulent heat flux measurements over snow could be easily obtained or measured. Data used in this research were gathered from an energy balance (EB) snow study site, called CUES, located on Mammoth Mountain Ski Area, California (Bair et al., 2015) (Figures 1 and 2). CUES is one of only a handful of locations throughout the western U.S. where the full EB may be studied at a point (Bales et al., 2006). These EB sites were designed with the intent to better understand hydrologic processes in complex mountainous terrain while helping to inform water managers that rely on accurate estimates of water availability for future consumptive purposes.

A detailed history of the site can be found in Bair et al. 2015 with records dating as far back as 1928. The current location of the CUES platform was established in 1987 and is a collaboration between The US Army Corps of Engineers Cold Regions Research and Engineering Laboratory (CRREL) and the University of California, Santa Barbara (UCSB) (CRREL-UCSB Energy Site, CUES). The 7.0 m high platform (Figure 3) is located on a plateau near the gondola station midway up Mammoth Mountain Ski Area at an elevation of 2,940 m just below the tree line. There are a few small clusters of mostly Whitebark and Lodgepole Pine trees that surround the platform with smaller shrubs that remain buried under snow for most of the winter (Bair et al., 2015). Instruments are mounted on or above the platform's railing between 7.0 and 9.0 m above the ground or on movable arms. The movable arms are needed due to the large amounts of snow accumulation that are possible throughout the winter. However, without knowledge of when an instrument was moved, use of these movable arms could affect the consistency of EB calculations when the exact height of a particular measurement is needed. In addition, if the height of the air

temperature and wind speed sensors have changed, this could bias estimates of turbulent heat fluxes. Possible biases were not accounted for in the study.

Prevailing winds at CUES are from the southwest (Figure 4). When looking at Google Earth (Figure 5), a southwesterly wind is from a direction that is in line with the top of Mammoth Mountain. The mountain therefore acts as a natural barrier, leading to lower wind speeds and less turbulent conditions at CUES when compared to the top of the mountain. Using data from this study, mean one-minute wind speeds at CUES are 3.1 m s^{-1} with a maximum one-minute wind speed of 18.9 m s^{-1}. For comparison, the highest recorded wind gust at the top of Mammoth Mountain is greater than 80 m s^{-1} with a mean wind speed at least 50% greater than at CUES (Bair et al., 2018).

The decision to create a ski resort on Mammoth Mountain was not by accident. Even though Mammoth Mountain sits on the east side of the Sierra Crest, local topography shows that the mountain sits in a low spot in the Sierra at the eastern edge of the San Joaquin River Valley. Many times, the valley allows moisture from cool season (November-April) Pacific storms to flow somewhat uninhibited until reaching the windward side of the mountain. Air is then lifted orographically and adiabatically cooled, forcing water vaper to condense. Moisture is then deposited on the lee side of the mountain, usually as snow. However, as this air descends on the lee side, it warms adiabatically and therefore becomes drier. This would be an important factor if the CUES platform were located further east but I think it sits close enough to the crest that it does not significantly alter the results herein.

Consistent with the climate of California, snowfall at Mammoth Mountain exhibits high interannual variability (Cayan 1996). Between water years 2002 and 2017 maximum snow depth at CUES has ranged between 135 cm in 2015 to more than 600 cm in 2006 (Figure 6) when the

depth sensor was buried, and exact measurements were not obtained. Typically, snow is present at CUES continuously from November to May and sometimes as late as July. The continuous nature of the data makes it possible to study turbulent heat fluxes under different meteorological conditions. This will shed light on whether DLHF could cause substantial changes to an existing snowpack during ARs and help answer some of the objectives of this thesis.

2.2 CUES Data

One-minute resolution CUES data were gathered from https://snow.ucsb.edu/ and are listed in Table 1. Five-minute resolution CUES data were also gathered at https://snow.ucsb.edu/ and are listed in Table 2. The choice to use data from CUES stems from the difficulties of finding historical measurements of T_{snow}. The T_{snow} sensor was installed at CUES in November 2016 with data availability beginning 3 November 2016 after the first snowfall of the season. Therefore, data for this study were gathered for 1 October 2016 through 31 May 2021. CUES data are available in three levels (Bair at al., 2015), with level 0 being raw data, level 1 being normalized and checked for errors, and level 2 being model ready quality-controlled data. Some Level 2 data are available through 2017. However, since the T_{snow} sensor was not installed until November 2016, and has mostly continuous measurements to present, I chose to use level 1 data. Because level 1 data are not the highest quality data, gaps exist when instruments may not have been operating properly or were possibly down for maintenance. Data filling or interpolation methods were not performed for any data in this study. Level 1 data was previously checked for errors, but a few data points were still outside of acceptable values. I performed the following additional quality control procedures on the CUES data:

Incoming solar radiation < 0 W m^{-2} was set to 0 W m^{-2},

Incoming solar radiation > 2000 W m^{-2} was removed,

Reflected solar radiation < 0 W m^{-2} was set to 0 W m^{-2}

Reflected solar radiation > 1500 W m^{-2} was removed,

If incoming solar radiation = 0 W m^{-2} then reflected solar radiation = 0 W m^{-2}

Incoming longwave radiation > 450 W m^{-2} was removed,

Air temperature > 26° C or < -30° C was removed,

Snow surface temperature > 0° C was removed,

Relative humidity < 0% was set to 0%,

Relative humidity > 100% was set to 100%,

Barometric pressure < 650 mb was removed,

Wind speed = 0 was removed. This occurred mostly at the beginning of the dataset through 5 April 2017 but also sporadically throughout,

Snow water equivalent < 0 cm was set to 0 cm.

2.3 Data From Other Sources

The CUES platform does not maintain a heated precipitation gauge so hourly tipping bucket precipitation measurements were collected at the Mammoth Pass (MHP) weather station (Figure 2) from the California Data Exchange Center (CDEC; https://cdec.water.ca.gov/dynamicapp/staMeta?station_id=MHP) website. This station is situated approximately 3.4 km south of CUES and is operated by the U.S. Bureau of Reclamation with

fifteen-minute precipitation records beginning in December 1994. Because these data are stored as an accumulation, hourly incremental values were calculated.

Hourly integrated water vapor transport (IVT) [kg m^{-1} s^{-1}] data were gathered from the European Centre for Medium-Range Weather Forecasts (ECMWF) ERA5 re-analysis dataset at https://cds.climate.copernicus.eu/cdsapp#!/dataset/reanalysis-era5-single-levels?tab=form as the vertical integral of both northward and eastward water vapor fluxes (Hersbach et al., 2018) with a spatial resolution of 0.25° x 0.25°. Because CUES is located very close to the Sierra Crest, I chose to download IVT at two grid cells: one on the windward side and one on the lee side (Figure 7). The closest windward side grid cell is at 37.5N x -119.25E, centered 25 km SW of CUES. The closest lee side grid cell is at 37.75N x -118.75E, centered 27 km NE of CUES. There are no missing data for the dates in this study and full IVT at each grid cell were calculated as:

$$Full\ IVT\ = \left|\sqrt{(\int Northward\ IVT)^2 + (\int Eastward\ IVT)^2}\right| \quad (1)$$

and then averaged to get a more representative IVT value at CUES. Rutz et al., 2014 found that AR conditions occurred between 1 and 3% of the time in the Eastern Sierra around the general location of Mammoth Mountain during 23 cool seasons from 1998-2011. Average ERA5 IVT greater than 250 kg m^{-1} s^{-1} occurred 1.1% of the time over the 5 cool seasons used in this analysis. This lies within the findings of Rutz et al., 2014 which also used an AR shape to identify ARs. For this study, I only used IVT greater than 250 kg m^{-1} s^{-1} to identify AR conditions.

Approximately eight months of unpublished hourly turbulent heat flux data during water year 2020, using the EC method, were given to me by Ned Bair, an associate snow researcher at the Earth Research Institute, University of California, Santa Barbara. This was not the method I chose to use but I will show how the two methods compare in later sections.

3 Methods

3.1 Surface Energy Flux Terms Over Snow

The total surface energy flux over snow is the sum of individual energy fluxes into and out of the snowpack. For this study I used the surface EB approach of Heron and Woo, 1978 which expressed the EB as:

$$Q_M = Q^* + Q_H + Q_E + Q_P + Q_G \qquad (2)$$

where Q_M is the total SEF and can be thought of as the energy available for snow melt, Q* is the flux of net radiation (NR), Q_H is sensible heat flux, Q_E is latent heat flux, Q_P is the advective heat flux (AHF) from precipitation, and Q_G is ground heat flux. Units for each term of the EB are W m^{-2} and fluxes directed towards the snow surface are positive.

Q*, is defined as:

$$Q^* = Q_{SW}\downarrow - Q_{SW}\uparrow + Q_{LW}\downarrow - Q_{LW}\uparrow \qquad (3)$$

where $Q_{SW}\downarrow$ is incoming shortwave radiation, $Q_{SW}\uparrow$ is reflected shortwave radiation, $Q_{LW}\downarrow$ is incoming longwave radiation, and $Q_{LW}\uparrow$ is outgoing longwave radiation. Units for each term of Q* are W m^{-2}. The only term that I did not find when downloading CUES data is Q_{LW} which was calculated using the Stefan-Boltzmann law:

$$Q_{LW}\uparrow = T_{snow}^4 \sigma \epsilon_s \qquad (4)$$

where T_{snow} is the temperature of the snow surface [K], σ is the Stefan-Boltzmann constant (5.67×10^{-8} [W m^{-2} K^4]), and ϵ_s is the emissivity of snow with a value of 0.985 (Dozier and Warren, 1982).

To calculate Q_H and Q_E I used the bulk-aerodynamic method (Heron and Woo, 1978):

$$Q_H = \rho_a C_a D_H u(T_z - T_{snow}) \quad (5)$$

$$Q_E = \rho_a \lambda(\frac{\varepsilon}{P}) D_E u(e_z - e_{snow}) \quad (6)$$

where ρ_a is the density of air [kg m^{-3}], C_a is the heat capacity of air at constant pressure [assumed to be 1,004 J kg^{-1} K^{-1}], D_H and D_E are dimensionless turbulent transfer coefficients for heat and water vapor, respectively, u is wind speed [m s^{-1}] at height z [m], T_z and T_{snow} are the temperature [K] at height z [m] and snow surface [K], respectively, λ is the latent heat of vaporization at 0° C [2.5x10^6 J kg^{-1}], ε is the dimensionless ratio of the molecular weights of water and dry air [0.622], P is atmospheric pressure [Pa], and e_z and e_{snow} are the water vapor pressures [Pa] at height z [m], and at the snow surface, respectively.

To solve for e_z, the saturation vapor pressure at height z and RH must be known. Saturation vapor pressure over water (T > 0° C) was calculated using Huang, 2018:

$$P_{s,w} = \frac{exp\,(34.494 - \frac{4924.99}{T+237.1})}{(T+105)^{1.57}} \quad (T > 0^\circ C) \quad (7)$$

where $P_{s,w}$ is the saturation vapor pressure [Pa] over water and T is the temperature [C] at height z [m]. Then, the vapor pressure of the air is simply $P_{s,w}$ multiplied by RH as a decimal.

The vapor pressure at the snow surface is simply the saturation vapor pressure at T_{snow}. I again used Huang, 2018 but calculated the saturation vapor pressure over ice ($T \leq 0°$ C):

$$P_{s,i} = \frac{exp\,(43.494 - \frac{6545.8}{T+278})}{(T+868)^2} \qquad (T \leq 0° \text{ C}) \qquad (8)$$

where $P_{s,i}$ is the saturation vapor pressure [Pa] over ice and T is the temperature [C] at height z [m].

The dewpoint temperature was calculated using the Clausius-Clapeyron equation shown in Curry and Webster, 1999:

$$\frac{e_2}{e_1} = exp\,[\frac{-L_{lv}}{R_v}\left(\frac{1}{T_2} - \frac{1}{T_1}\right)] \qquad (9)$$

Where e_1 and e_2 are the saturation vapor pressures at temperatures T_1 and T_2 in Kelvins, respectively, L_{lv} is the latent heat of vaporization at 0° C (2.5×10^6 [J kg^{-1}]), and R_v is the gas constant for moist air (461.5 [J kg^{-1} K^{-1}]). To solve for e_1, you can assume that T_1 is equal to 0° C. T = 0° C in Equation 7 gives e_1 = 611.24 Pa. Inserting values of T_1 and e_1 into Equation 9 and rearranging gives:

$$\frac{e_2}{611.24\,[Pa]} = exp\,[\frac{L_{lv}}{R_v}\left(\frac{1}{273.15\,[K]} - \frac{1}{T_2}\right)] \qquad (10)$$

Since values for e_2 are given by Equation 7, the dewpoint temperature, T_2, can be calculated.

The calculation for air density is derived using the ideal gas law rearranged as:

$$\rho = \left(\frac{P_d}{R_d * T}\right) + \left(\frac{P_v}{R_v * T}\right) \qquad (11)$$

where ρ is the air density [kg m^{-3}], P_d is the pressure of dry air [Pa], which is calculated as the air pressure [Pa] – e_z [Pa], R_d is the gas constant for dry air (287.05 [J kg^{-1} K^{-1}]), T is the air temperature [K] at height z [m], P_v is e_z [Pa], and R_v is the gas constant for moist air.

The dimensionless turbulent transfer coefficients D_H and D_E were assumed to be equal under neutral atmospheric stability in Heron and Woo, 1978 and equal to D, the aerodynamic eddy diffusivity:

$$D = \frac{K^2}{[ln(\frac{z}{z_0})]^2} \qquad (12)$$

where K is the dimensionless von Kármán's constant [0.4], z is the wind speed measurement height [7m at CUES], and z_0 is the aerodynamic roughness length [m] which is the height above the ground surface at which the wind velocity drops to zero (Smith, 2014). A detailed review of the turbulent transfer coefficients can be found in Male and Grainger, 1981. The equality of these coefficients has been used in other studies and more recent snow models (Garvelmann et al., 2014; Price et al., 1976; Tarboton and Luce, 1996) and was therefore assumed to be correct.

If a logarithmic wind profile is assumed, Heron and Woo, 1978 estimated z_0 as:

$$z_0 = exp\left(\frac{u_2 \, ln \, z_1 - u_1 \, ln \, z_2}{u_2 - u_1}\right) \qquad (13)$$

where u_1 and u_2 are wind speed [m s^{-1}] measurements at levels z_1 and z_2 [m]. Unfortunately, CUES only has wind speed measurements at one level. Therefore, I used a best fit process that is explained after the corrections for stability are described.

Because D_H and D_E are used under neutral atmospheric conditions, and considering the atmosphere above a snowpack is typically stable with air temperature (T_a) warmer than T_{snow}, the following stability corrections to the turbulent transfer coefficients were made using the Richardson (Ri) number to determine stability type (Price and Dunne, 1976):

$$Ri = gz\frac{T_z - T_s}{T_z(u_z - u_s)^2} \quad (14)$$

where Ri is the dimensionless Ri number and is the ratio of buoyancy to vertical shear, g is the acceleration due to gravity [m s^{-2}], z is the wind speed measurement height [7 m at CUES], T_z and T_s are T_a [K] at height z [m] and T_{snow} [K], respectively, u_z is the wind speed [m s^{-1}] at height z [m], and u_s is the wind speed at the surface which is assumed to be 0 m s^{-1}. The only way that Ri can be negative is when T_{snow} is greater than T_a. This is not common over a snowpack and occurs 4.4% of the time at CUES using one-minute data.

Under stable conditions (Ri > 0), the turbulent transfer coefficients are corrected using:

$$D_s = [\frac{D}{1+\sigma Ri}] \quad (15)$$

Under unstable conditions (Ri < 0), the turbulent transfer coefficients are corrected using:

$$D_u = D(1 - \sigma Ri) \quad (16)$$

where D is the turbulent transfer coefficient under neutral conditions and σ is a dimensionless constant assumed to be 10.

When solving for turbulent heat fluxes using the bulk method, z_0 represents a parameter that is not easily obtained. I used EC LHF and bulk LHF data to perform a best fit analysis using

a range of z_0 values appropriate for snow surfaces (Brock et al., 2006). Table 3 lists the range of z_0 values tested along with the root mean square error (RMSE) between the two methods. I chose to use LHF for this analysis due to the possibility that the EC method is resolving strong countergradient SHF (Lapo et al., 2019) which would have made it difficult to find a best fit. The highlighted row in Table 3 represents the z_0 value with the smallest RMSE and is used in all further analysis. I will note here that without a more robust calculation, the estimated z_0 of 0.02 m is near the higher end of published values for snow. For comparison, Heron and Woo, 1978 found an average value of 0.003 m in their study using Equation 13.

Figure 8A is an hourly time series, during February 2020, of bulk LHF, black line, and EC LHF, blue line. The magnitude of some of the negative values line up very well. The EC data shows a much stronger diurnal cycle but are mostly the same sign as bulk LHF. Figure 8B is a scatterplot of EC LHF data vs. bulk LHF for the same time. What is notable here is that many positive bulk LHF values correspond to negative EC LHF values. This may signify that the bulk method is overestimating DLHF at these times. When EC LHF is positive, the bulk method is very close to zero. This may be due to countergradient fluxes that I am unable to represent using the bulk method since it is strictly a down gradient calculation. These countergradient fluxes may be due to local topography, vegetation, or even the nearby mid mountain gondola station. In addition, vertical wind velocities and specific humidity measurements from the EC data were sampled at 10 Hz, which allows for much more variance in measurements.

After calculating the SEF terms at one-minute resolution, I forward averaged the entire dataset to obtain an hourly resolution dataset. Prior to averaging and because each variable from CUES contained different amounts of missing data, I set a threshold that one-minute data must have at least 45 values during the hour to compute the hourly mean. For five-minute data, this threshold was set at 15 values during the hour to compute the hourly mean.

To calculate the AHF from precipitation, Q_P, I used the methods of Born et al., 2019:

$$Q_{P,rain} = P\rho_w C_w(T_{air} - T_0) \quad (17)$$

$$Q_{P,snow} = P\rho_w C_i(T_{air} - T_{snow}) \quad (18)$$

where P is the rainfall intensity [m s^{-1}], ρ_w is the density of water (1,000 [kg m^{-3}]), C_w is the heat capacity of water at 25° C (4,181 [J kg^{-1} K^{-1}]), C_i is the heat capacity of ice at -10° C (2,110 [J kg^{-1} K^{-1}]), T_{air} is T_a [K], and T_0 is the freezing temperature of water at sea level (273.15 [K]).

To calculate the ground heat flux, soil moisture and soil temperature data are needed. This flux is likely very small and negligible during mid winter when a large snowpack exists. Therefore, this flux was neglected in this analysis.

To eliminate large diurnal cycles in variables such as solar radiation that would have greatly biased the results, I forward averaged the hourly data to obtain a daily resolution dataset. To compute daily means, I set a threshold that hourly data must have at least 18 values during the hour. For incremental hourly precipitation data, the same threshold was used but the sum was taken over each hour. Q_P was then recalculated using this hourly sum. Daily Q_M using the new Q_P and daily means of Q*, Q_H, and Q_E was also recalculated.

Because I am interested in identifying the importance of LHF over snow, I eliminated all data for times when there was not at least 15.24 cm (6 inches) of snow present at CUES. Table 4 shows the dates when there was continuous snow depth. For consistency in the data analysis, and because I did not fill or interpolate missing data, if a variable contained missing data, all data for that time was eliminated. Table 5 shows daily mean values of select variables collected/calculated at CUES pre and post application of the snow threshold and after elimination of times with missing data.

3.2 Typical Air and Dewpoint Temperatures during Atmospheric Rivers in the Northern Sierra Nevada Mountains

To identify typical T_a and T_d during ARs in the northern Sierra Nevada Mountains and assess how representative CUES is to locations in the Feather and Yuba River watersheds, I downloaded hourly T_a and RH data from CDEC (https://cdec.water.ca.gov/dynamicapp/staSearch) at select locations within each watershed. There are a total of 18 stations within the Yuba River watershed and 26 stations within the Feather River watershed with co-located data available on the website. However, station data were not downloaded if it was either installed after 1 October 2016 or ended data collection before 2021. AR conditions were identified using IVT data from the ECMWF ERA5 reanalysis dataset. One grid cell was chosen to represent each watershed and full IVT was calculated using Equation 1. Figure 9 shows the stations used and the location of the ERA5 grid cell for each watershed. Values of T_d were calculated using Equation 9.

4 Results

4.1 Typical Air and Dewpoint Temperatures during Atmospheric Rivers in the Northern Sierra Nevada Mountains

CUES is cooler than many locations within the Feather and Yuba River watersheds during ARs, regardless of elevation (Table 6). If a station does not have a mean T_d shown, it means that the station does not measure RH and therefore, T_d cannot be calculated. In this table, hourly T_d during ARs is often above 0° C. This is important for a couple reasons. First, T_{snow} can never be above 0° C. This means there is a maximum possible saturation vapor pressure of 611.24 Pa at the snow surface. Second, if T_d is above 0° C, and the dewpoint depression is small, there is a greater chance that the vapor pressure in the air is greater than 611.24 Pa. Per Equation 6, and depending on atmospheric stability and wind speed, large amounts of latent heat could be directed downward with condensation occurring on the snowpack. This latent heat flux will help reduce the snowpack's cold content and may contributing to snowmelt.

4.2 Bulk-Aerodynamic Method

A schematic of how the bulk-aerodynamic method works is shown in Figure 10. This method estimates turbulent heat fluxes by recognizing the difference between either the air and snow surface temperature or the difference between the water vapor pressure in the air and at the snow surface. Therefore, it is strictly a down gradient calculation. What this means is that if the air is warmer than the snow surface, sensible heat will be transferred to the snow surface. If the air is cooler than the snow surface, sensible heat will be transferred to the air. If the air is moister than the snow surface, deposition will occur, and latent heat will be transferred to the snow surface. Finally, if the air is less moist than the snow surface, sublimation will occur, and latent

heat will be transferred to the air. One shortcoming of this method is that it cannot resolve countergradient fluxes that were mentioned earlier and are described in more detail in section 4.3.

4.2.1 Turbulent Heat Fluxes

The flux of sensible heat depends mostly on near surface atmospheric stability, the temperature difference between the air and snow surface (ΔT) and is highly dependent upon wind speed. It is downward most times of the year except when Ta is less than Tsnow. The flux of latent heat depends mostly on near surface atmospheric stability, Δe, and is also highly dependent upon wind speed. It is upward most times of the year at CUES because Td is usually less than Tsnow.

Daily mean values of SHF and LHF at CUES range between -68 W m^{-2} to 164 W m^{-2} and -113 W m^{-2} to 29 W m^{-2}, respectively (Figure 11), and are consistent with Marks and Dozier, 1992 who used a more robust model to calculate turbulent heat fluxes at two sites in the southern Sierra Nevada Mountains. Figure 12 is an hourly time series plot of data from CUES with calculated turbulent heat fluxes during February 2019. The plot is representative of the cool season at CUES and shows the emergence of several patterns. In the upper panel, temperatures are seen to converge when RH increases. During some of these times, temperatures also tend to decrease over time even though total SEF is close to zero. Larger scale weather patterns may be responsible for this trend but were not identified as part of this study. In the middle panel, increased values of IVT are seen at the beginning, middle, and end of the month with values above the 250 kg m^{-1} s^{-1} AR threshold on the 13th and 14th, possibly signifying AR conditions. However, very small turbulent heat fluxes are seen on these dates. In the bottom panel, there are many consecutive days when turbulent heat fluxes and NR are very close to zero. As T_a and T_{Snow}

converge, ΔT is small and SHF will tend towards zero. However, the opposite is not always true. For example, on 7 and 23 February there are large ΔT values but very small turbulent heat fluxes. These large ΔT values at times of weak wind speeds lead to possibly unreasonable Ri numbers and stability corrections that essentially turn off SHF. The same is true for LHF on these days. Even though T_d is much greater than T_{Snow}, large Ri numbers suggest that the atmosphere is too stable to allow for much LHF. There are other days with large ΔT and T_d greater than T_{Snow}, 6 and 8 February for example, leading to DLHF and large values of downward SHF. Additional research may find a 'sweet spot' of atmospheric stability and wind speed when DLHF and downward SHF occur with large ΔT. Given these results, it may be the case that DLHF is not large enough during ARs to cause rapid snowpack changes at CUES.

4.2.2 Importance of Downward Latent Heat Flux

The original focus of this research was to understand the importance of condensational heating of a snowpack during ARs. However, after a quick review of Figure 12, it appears that large values of DLHF do not occur during periods of increased IVT and is therefore not important during AR conditions. Table 7 shows the monthly frequency of daily mean LHF over all water years. Overall, DLHF occurs 25% of the time at CUES with the months of November through March having the greatest frequency. The spring months of May and June are warmer than mid-winter, with T_d possibly greater than T_{Snow}, but with a lot of missing T_{Snow} data during these months LHF is largely unknown.

Figure 13 shows the daily mean distributions of each SEF term to show how important LHF is to the total SEF. Figure 13A shows daily mean distributions of all CUES data on dates with snow. SHF appears to be the largest term in the total SEF with a median and mean value of

17.5 W m^{-2} and 28.0 W m^{-2}, respectively. Median and mean values of LHF are -3.6 W m^{-2} and -9.8 W m^{-2}, respectively. The 75th percentile of LHF is -0.03 W m^{-2} showing, again, that LHF is downward roughly 25% of the time. AHF is very close to zero and has been omitted from further results. Median and mean values of NR are -6.4 W m^{-2} and -5.7 W m^{-2}, respectively. After adding the EB terms, the median and mean total SEF are 10.1 W m^{-2} and 12.8 W m^{-2}, respectively. Overall, the total SEF is downward most of the time with LHF bringing total SEF closer to zero. Figure 13B shows daily mean distributions of CUES data on days with DLHF. SHF has less influence on total SEF and is mostly downward with a minimum value of -0.7 W m^{-2}. The magnitude of SHF decreases with median and mean SHF values of 10.5 W m^{-2} and 16.1 W m^{-2}, respectively. LHF is of course all downward with a 75th percentile of 3.9 W m^{-2}. The distribution of NR does not change much with both the median and mean equal to -6 W m^{-2}. The distribution of total SEF on days with DLHF changes slightly with the median lowering to 9.9 W m^{-2} and the mean rising to 13.5 W m^{-2}. Again, total SEF is downward, but there is not a significant difference in total SEF on days with DLHF.

After identifying the distributions of each SEF term on days with DLHF the percent contribution of DLHF to the total SEF was identified to see if DLHF was ever the most important term in the total SEF. Figure 14 shows the percent contribution of each SEF term on each day with daily mean DLHF. The black line with dots indicates the percent contribution of DLHF. The horizontal dashed black line represents the mean DLHF percent contribution of 9.6%. The other grey horizontal dashed lines represent the mean percent contribution of the other SEF terms, as shown. DLHF contributes much less to the total SEF than NR and SHF and out of the 149 days when LHF was downward, it is never the most important term in the total SEF.

4.2.3 Meteorological Thresholds

Meteorological thresholds were created to help identify conditions favorable for DLHF. The first threshold is simply the presence of snow. Other thresholds limit the data to the following: times when daily mean LHF is upward or downward, when daily mean $T_d > 95^{th}$ percentile, when daily mean IVT > 95^{th} percentile, when daily mean RH > 95^{th} percentile, when daily mean SEF > 95^{th} percentile, when daily mean $T_{Snow} > 95^{th}$ percentile, and when daily mean LHF > 95^{th} percentile. These percentile thresholds were also limited to times when snow is present. When snow is present, and after the removal of times with missing data, 595 daily mean values of each variable remain. Therefore, the 95^{th} percentile of a given variable will include the 30 most extreme values. The T_d threshold was chosen with the idea that T_d may be sufficiently larger than T_{Snow} to allow for DLHF. The T_{Snow} threshold was chosen in hopes that when T_{Snow} was closest to 0° C, T_d would be greater than T_{snow} and DLHF would occur. The IVT threshold was chosen to identify LHF values under AR conditions. However, the 99^{th} percentile of daily mean IVT at CUES is 227 kg m^{-1} s^{-1}. This indicates that either hourly IVT is not above the traditional AR threshold at CUES long enough for the daily mean to indicate AR conditions or that storm systems tend to be much drier close to the Sierra crest. The RH threshold was chosen because these are times when the air is close to saturation and abundant moisture is flowing over the snowpack leading to an elevated chance of condensing water vapor onto the snowpack. The SEF threshold was chosen to understand the role of LHF when the greatest amount of energy was entering the snowpack. Finally, the LHF threshold was chosen to understand meteorological conditions when DLHF occurs most often and in case DLHF was small under other thresholds.

Daily mean distributions of the SEF terms were described in the previous section. When looking at daily mean probability density functions (PDF) of other meteorological variables when snow is present (Figure 15), some interesting conditions on days with DLHF begin to emerge.

The two most drastic differences are that T_a is approximately 4° C cooler than average and RH increases significantly. T_d is approximately 2° C warmer than average, and T_{Snow} is 1.6° C cooler than average. Since T_d is always less than T_a and T_{Snow} is likely to be less than T_a, temperatures seem to be converging, as evidenced in Figure 12. This means that ΔT becomes smaller leading to smaller Ri numbers with stability tending towards neutral. Because the dewpoint depression decreases, the increase in RH is quite drastic. T_d must now be warmer than T_{Snow} leading to positive values of Δe and DLHF. Negative values of Δe appear in the PDF but are likely an artifact of forward averaging to daily means. Finally, DLHF occurs slightly more often on days with IVT greater than 250 kg m^{-1} s^{-1}. However, the relatively small increase in IVT does not indicate that DLHF occurs significantly more often with increased IVT.

Table 8 lists daily mean values for meteorological variables shown in Figure 15 for all thresholds. LHF is downward only under the DLHF threshold and LHF > 95th percentile threshold. An IVT value of 66 kg m^{-1} s^{-1} when DLHF is largest, with very few values of IVT greater than 200 kg m^{-1} s^{-1} in Figure 15, further indicates that DLHF is not common during AR conditions. DLHF may be possible under other thresholds but will not be large. The flux of sensible heat is downward under all thresholds and larger in magnitude than NR and LHF, again indicating that it is the primary driver of SEF under each threshold. Total SEF is downward under all thresholds, smallest under the RH threshold, and relatively large during the LHF threshold. Figure 12 clearly shows SEF terms near zero when RH is high. With SHF downward under all thresholds, even though NR is most negative under the LHF threshold, likely from a greater amount of outgoing longwave radiation than incoming solar radiation due to clouds, the largest LHF values added to large SHF values lead to relatively large downward SEF. T_d is greater than T_{Snow} only when looking at thresholds with DLHF. This indicates that T_d at CUES is too cool to get DLHF under most thresholds even with high RH values. The most promising threshold for

snow melt is $T_{Snow} > 95^{th}$ percentile since substantial snowmelt can only occur when a snowpack is isothermal at 0° C. However, under this threshold, T_d remains cooler than T_{Snow} and LHF is upward. These results indicate that even under certain limiting thresholds, LHF at CUES is mostly upward. Even though SEF is downward under all thresholds, T_{Snow} is too cold to have significant melt, and with LHF mostly upward, the snowpack is mostly sublimating and cooling.

4.2.4 Composite Plots

Turbulent heat fluxes depend greatly on the current state of the atmosphere and are in a constant state of change. For instance, at a high elevation location such as CUES, where T_a tends to be below freezing much of the time, if T_d happens to be warmer than T_{Snow}, DLHF and condensational heating of the snowpack will be shown to occur. However, large amounts of LHF directed towards the snow, among other variables such as NR and SHF, may increase T_{Snow}. This increase could cause T_{Snow} to become warmer than T_d, or cause Δe to be negative, thereby switching to upward LHF and sublimation of the snow.

In this section I identify any obvious patterns on days surrounding specific thresholds and identify reasons why DLHF was or was not occurring. The thresholds I chose to look at are daily mean IVT > 95^{th} percentile, daily mean RH > 95^{th} percentile, and daily mean LHF > 95^{th} percentile. Figure 16 is an hourly time series plot of data from CUES with calculated turbulent heat fluxes for 11 February 2019 to 16 February 2019. It is obvious by this plot that there are interesting meteorological processes occurring when IVT and RH are large.

Each composite plot has 3 panels of hourly data; from left to right, the day prior to the threshold being met, the first day the threshold was met, and the day after the threshold was met. Under each specific threshold there were times when the threshold was met for multiple

consecutive days. Therefore, the middle panel only shows the composite of the first day the threshold was met. The panel for the day prior to the threshold being met is the composite of days before the first day the threshold was met. Since the day after the first day the threshold was met may still be above the threshold, this panel may not be fully representative of when conditions drop below the specific threshold. Figure 16 shows that both the IVT and RH thresholds may have been met on two consecutive days. If the day after is still within the threshold it is not included in the first day the threshold was met composite. Figures 17-19 are the hourly composite plots, of the same variables in figure 15, when daily mean IVT, daily mean RH, and daily mean LHF exceeded the 95th percentile, respectively. When referring to each day, the day before the threshold is met will be considered day -1, the first day the threshold was met will be considered day 0, and the day after the threshold was met will be considered day 1. In each panel, the black line is the hourly composite mean, the red line is the hourly CUES mean using all data when snow is present, and the grey shading represents the 20^{th} to 80^{th} percentiles of the hourly composite. A distinct hourly mean diurnal cycle is obvious in all variables except IVT.

4.2.4.1 IVT > 95^{th} Percentile

Figure 17 is the hourly composite plot of how each meteorological variable changes in time when daily mean IVT is greater than the 95^{th} percentile. Hourly composite IVT increases on days -1 and 0 peaking at approximately 200 kg m^{-1} s^{-1} just before mid-day on day 0 with the 80^{th} percentile above the traditional AR threshold of 250 kg m^{-1} s^{-1}. At an hourly temporal scale, AR conditions may be present at this time. LHF is usually upward and close to the normal diurnal cycle on days -1 and 1. On day 0 it begins slightly more negative than normal but deviates from the diurnal cycle at mid-day, eventually becoming downward. However, the magnitude of DLHF is small with a maximum hourly composite mean value of 5.6 W m^{-2}.

T_a on day -1 is about average with a suppressed diurnal cycle. On days 0 and 1 it continues to drop with almost no warming on day 0. T_d is much warmer than normal on day -1 and increases until just after mid-day of day 0, after which it drops sharply back to normal. T_{Snow} is very similar to T_d and again begins to decrease sharply mid-day of day 0. From this, there are likely two controlling factors for the occurrence of DLHF. First, increasing IVT signifies that a combination of moisture and winds are increasing at CUES. Wind is a very important factor in the bulk formula and are, at times, shown to double in velocity. The hourly composite mean is greater than the data mean by approximately 1 m s^{-1} with no major changes in wind speed over all three days. Therefore, wind does not appear to significantly change the magnitude of the composite mean turbulent heat fluxes. With increasing moisture and decreasing T_a, T_d, and therefore RH, must also increase. As IVT diminishes towards the end of day 0, T_a is relatively stable which means that T_d and RH fall sharply at the end of day 0 into day 1. Another factor is how T_{Snow} behaves, and the timing of the drop in temperature between days 0 and 1. We see that T_{Snow} is much warmer than normal until day 1. SEF on day -1 is at normal values leading to an increase in T_{Snow}. However, in the overnight hours between days -1 and 0, SEF is above normal and around 0 W m^{-2}. Since no energy is entering or leaving the snow, T_{Snow} does not change much. T_{Snow} rises slightly on day 0 but does not change much through day 0 because NR is suppressed. Since NR is suppressed, there is more time for radiational cooling of the snow, which may be why we see such a large decrease in T_{Snow}. Another possibility for why T_{Snow} behaves as it does may be due to precipitation. The temperature of the precipitation should be close to the wet bulb temperature. This temperature lies between T_a and T_d and with these temperatures converging the temperature of the freshly fallen precipitation will be constrained. This may be true at some times when the temperatures converge but it isn't precipitating at all times of temperature convergence. Another important reason for this is that the bulk formula is more of a

diagnostic tool and only knows the current state of the atmosphere. We see that T_{snow} cools rapidly after mid-day on day 0. However, because the bulk formula is strictly a down gradient calculation it has no way of representing a process such as countergradient fluxes.

Net radiation plays a large role in changes to the total SEF and differences from the mean are likely from cloud cover. On days -1 and 1, NR is very close to normal. Greater than normal negative values, with an increasing trend, occur during the overnight hours between days -1 and 0. Greater than normal negative values also occur during the overnight hours between days 0 and 1 but with a decreasing trend. Suppressed NR values are seen throughout day 0 due to less solar radiation reaching the sensor. This indicates that cloud cover was likely increasing before day 0, present throughout day 0, and decreasing into day 1. The increasing overnight trend would be due to an increase in downward longwave radiation from clouds. The opposite would be true of a decreasing overnight trend.

The timing of when T_{Snow} begins to decrease, and the rate at which it decreases, determines if DLHF will occur. Figure 20 shows the combined hourly composites of T_a, T_d, and T_{Snow} when IVT is greater than the 95th percentile. When DLHF occurs at the end of day 0 into day 1, the hourly composite mean of T_d is almost identical to T_{Snow}. This means that there are enough times when Δe values become positive and DLHF occurs. We also see some temperature convergence on day 0. The decrease in ΔT will lead to a less stable environment that is more favorable for turbulent heat fluxes but because T_d is not much larger than T_{Snow}, positive Δe values remain small and limit the magnitude of DLHF.

4.2.4.2 RH > 95th Percentile

Figure 18 is the hourly composite plot of how each meteorological variables change in time when daily mean RH is greater than the 95th percentile. Hourly composite RH is above normal over all three days and is very close to 100% throughout day 0, rising sharply on day -1, and decreasing on day 1. Composite patterns for all variables are very similar to the IVT threshold with some subtle differences for each. DLHF values are slightly larger and at similar times as the IVT threshold during the overnight hours at the end of day 0. The 80th percentile of LHF has slightly larger downward values than under the IVT threshold with some DLHF at the end of day -1.

At the beginning of day -1 T_a is about normal and does not warm as much as the diurnal cycle, with a decreasing trend continuing over all days. The first difference is in the behavior of T_d. We see that T_d remains much above normal over all days. The pattern of IVT is identical to the IVT threshold but less magnitude. Again, increasing IVT signifies that a combination of moisture and winds are increasing over CUES. The hourly composite mean of wind speed is greater than the data mean with two local maximums reaching approximately 5 m s^{-1} and 80th percentile speeds reaching more than 7 m s^{-1}. Winds are stronger under this threshold and coincide with times of largest DLHF between days 0 and 1. With increasing moisture, and because T_a is continuing to drop, T_d is again forced to rise. However, when IVT begins to drop, T_a continues to drop so that RH and T_d remain elevated, and T_d does not drop as drastically on day 1. Similar arguments as before can be made for T_{Snow}, NR, and SEF. However, one major difference in SEF is that on day 0, SHF drops to zero due to a much smaller ΔT leading to much less than normal SEF. What is interesting here is that T_{Snow} does not decrease as much as in the IVT threshold even though SEF is much more suppressed on day 0. NR between days 0 and 1 is less negative so it could be the case that downward longwave radiation from cloud cover is offsetting

radiational cooling of the snow. Overall trends in NR are very similar to the IVT threshold with cloud cover likely during day 0, limiting the amount of solar radiation reaching CUES, and limiting the typical diurnal cycle in NR.

Under this threshold, the occurrence of DLHF is again dependent upon the timing of when T_{Snow} begins to decrease, and the rate at which it decreases. Figure 21 shows the hourly composite mean of T_a, T_d, and T_{Snow} when RH is greater than the 95th percentile. As with the IVT threshold, when DLHF occurs at the end day 0 into day 1, the hourly composite mean of T_d is almost identical to T_{Snow} such that there are enough times when Δe values become positive. Under the RH threshold it is much more obvious that temperatures converge on day 0. Because ΔT is so small, SHF is essentially shut off and since T_d is very close to T_{Snow}, positive Δe values again remain small and limit the magnitude of DLHF even though wind speeds are stronger than under the IVT threshold.

4.2.4.3 LHF > 95th Percentile

Because the IVT and RH threshold did not show an increased likelihood for DLHF, I then limited the data to when LHF was greatest. Figure 19 is the hourly composite plot of how each meteorological variable changes in time when daily mean LHF is greater than the 95th percentile. Hourly composite LHF is downward at the end of day -1, for most of day 0, at the beginning and end of day 1, and is much greater than the data mean. My hypothesis stated that ARs increase the likelihood of condensational heating of a snowpack that may lead to significant snowmelt. However, the largest values of DLHF occur when IVT is between 50 and 80 kg m^{-1} s^{-1}, much less than the traditional definition of AR conditions.

Some dramatic differences stand out when the largest values of LHF occur. IVT is much less than the previous thresholds and closer to normal. T_a is much colder than normal without a

decreasing trend over each day. With colder T_a, less moisture is needed to maintain relatively high T_d and RH values. So, even though IVT values are less than the previous thresholds, the much lower than average T_a can lead to a saturated atmosphere with ample amounts of moisture available to condense onto the snow.

On days -1 and 0, T_d is a little greater than normal but drops below normal after mid-day of day 0. On day -1, when IVT is largest, T_d is about average. With cooler than normal T_a, RH will be much greater than normal. But, because the trend in T_a is somewhat flat, as IVT drops, T_d and RH must also drop. T_{Snow} is close to normal until mid-day on day 0, follows the diurnal cycle better than the previous thresholds, but drops well below normal values at the end of day 0 into day 1. Again, the reason for the drop in T_{Snow} on day 0 is tough to describe. NR in the overnight hours between days 0 and 1 is normal and upward. However, this is offset by downward SHF and DLHF leading to close to zero SEF which does not explain why T_{snow} decreases so rapidly.

Figure 22 shows the hourly composite mean of T_a, T_d, and T_{Snow} when LHF is greater than the 95th percentile. There are two distinct times and meteorological conditions when DLHF occurs. The first is between days -1 and 0. With T_a much less than normal, and T_d slightly above normal, this leads to higher than normal RH. With T_{Snow} slightly below normal, T_d ends up being greater than T_{Snow}. Therefore, Δe is positive and DLHF occurs. The second is like the previous thresholds where IVT, RH, T_d, and T_{Snow} all begin to decrease. T_{Snow} begins to decrease before T_d, and quicker, causing T_d to be greater than T_{Snow}. At this point Δe is positive and DLHF occurs.

At a cold, high elevation location such as CUES it is not common for T_d to be greater than T_{Snow}. Because this condition does not occur often at CUES DLHF is not common and when it does occur its magnitude is not large. Under the three thresholds I studied, DLHF occurs most often when IVT, RH, T_d, and T_{Snow} decrease at the end of day 0, which correspond to times after

AR conditions have passed. When DLHF does occur, it is not during times of maximum IVT. It seems that CUES is at too high an elevation with T_d too cool for significant snowmelt to occur. However, DLHF may be more common at a warmer, lower elevation location. Therefore, Section 5 identifies a simple sensitivity process to test this secondary hypothesis.

4.3 Eddy Covariance Method

Eight months worth of hourly EC data were given to me by Ned Bair. Because I did not do these calculations myself, and because these data are unpublished and have not been peer-reviewed, the correctness of these data are not fully known. However, the sign and magnitude of the flux data are consistent with other published findings (Stigter et al. 2018). This method works by measuring horizontal and vertical wind eddies that pass a sonic anemometer attached to a tower. Example equations for measuring turbulent heat fluxes are as follows:

$$\text{SHF} = -\rho C_p(\overline{w'\theta'}) \quad (19)$$

$$\text{LHF} = -\rho L_v(\overline{w'q'}) \quad (20)$$

where ρ is the air density, Cp is the specific heat of air, Lv is the latent heat of vaporization/sublimation of water, $\overline{w'\theta'}$ is the time average of the instantaneous covariance of the vertical wind velocity, w, and the potential temperature, θ, and $\overline{w'q'}$ is the time average of the instantaneous covariance of the vertical wind velocity, w, and the specific humidity, q.

It is easy to see how the time average of the instantaneous covariances might lead to countergradient fluxes, but it is difficult to explain why they occur at CUES. Figure 23 explains one possibility. In this figure we see possible moisture profiles at the top of Mammoth Mountain and at CUES. At CUES, air at the snow surface is drier than in the air. At the top of Mammoth

Mountain, we see a similar moisture profile with drier air at the snow surface. We also see that due to the elevation difference it is likely to be drier overall at the top of Mammoth Mountain. If, at times, there is a down sloping wind transporting dry air from the top of Mammoth Mountain towards CUES, the air above CUES will become drier. This means that w and q are now negative at CUES. This will lead to a negative, or upward, LHF and sublimation. However, when using the bulk formula, the moisture profile at CUES would suggest DLHF. Again though, I am unsure if this is how countergradient fluxes work at CUES, but it seems to be one example of many.

4.3.1 Importance of Downward Latent Heat Flux

Daily mean values of SHF and LHF at CUES range between -172 W m^{-2} to 64 W m^{-2} and -85 W m^{-2} to 0 W m^{-2}, respectively. Table 9 shows the monthly frequency of daily mean LHF for the one water year of EC data. Daily mean DLHF does not occur. However, there is too much missing data for this table to be conclusive.

Figure 24 shows the daily mean distributions of each SEF term to show how important LHF is to the total SEF. Figure 24A show daily mean distributions of all EC data on dates with snow. We see that SHF and NR have less influence on the total SEF. The median and mean values of SHF are 6.7 W m^{-2} and 9.5 W m^{-2}, respectively. Median and mean values of LHF are -31.6 W m^{-2} and -32.8 W m^{-2}, respectively. The maximum value of LHF is -0.5 W m^{-2}, again signifying that DLHF does not occur. AHF is very close to zero and has been omitted from further results. Median and mean values of NR are -11.3 W m^{-2} and -10.7 W m^{-2}, respectively. After adding the EB terms, the median and mean total SEF are -30.0 W m^{-2} and -34.0 W m^{-2}, respectively. SEF is upward when using the EC turbulent heat fluxes. SHF and NR seem to cancel each other out, leaving LHF with much more influence on the SEF. Figure 24B is the same

as Figure 13A to compare the two methods. We see that both SHF and LHF have decreased and are both upward more often. This may be due to countergradient effects.

4.3.2 IVT > 95th Percentile

Figure 25 is the hourly composite plot of how each meteorological variable changes in time when daily mean IVT is greater than the 80th percentile. I lowered the percentile threshold due to having less EC data. Hourly composite IVT increases on days -1 and 0 peaking at approximately 100 kg m^{-1} s^{-1} just before mid-day on day 0. The much lower IVT values may indicate that AR conditions did not occur often at CUES during WY2020. In the LHF composite we see that the diurnal cycle is much more negative than with the bulk method, likely due to countergradient effects. The hourly composite of LHF follows this diurnal cycle until the end of day 0 into day 1 when we see very small values of DLHF. This corresponds well with times of DLHF using the bulk method.

With the EC method, the three temperatures and Δe are less important for turbulent heat fluxes. However, Δe is again positive at the end of day 0 into day 1 which would correspond to times of DLHF using the bulk method. The positive Δe values are again due to the T_{snow} dropping substantially at the end of day 0. The most striking difference with the bulk method is seen in the SHF. We see that ΔT is always positive and close to average. However, SHF is strongly upward during daylight hours. This is counter to what would be expected when using the bulk method and is when we begin to see strong countergradient effects with the EC method.

The hourly composite mean of NR does not deviate much from the hourly diurnal cycle. What is noticeable though is that large values of upward SHF and LHF are slightly offset from large values of downward NR. This is evident in the total SEF where we see a strong diurnal

pattern of oscillating upward and downward flux values. This pattern appears to correspond better with increasing T_{snow} during the day and decreasing T_{snow} at night. Comparisons of total SEF and T_{snow} between the two methods are explored in the next section.

4.4 Bulk-Aerodynamic and Eddy Covariance Comparison

Turbulent heat flux values calculated herein using both the bulk and EC methods are consistent with past research at similar locations. However, when looking at hourly composite plots under specific thresholds it is evident that T_{snow} changes in such a way that is inconsistent with turbulent heat fluxes and total SEF. For instance, in Figures 17-19 we see that T_{snow} decreases rapidly between days 0 and 1 while net SEF is downward or near 0 W m^{-2}. We also see that SHF is downward over all three days with DLHF occuring between days 0 and 1. With this energy directed towards the snow one would expect to see a rise in T_{snow}, not a sharp decrease. The question then is why is T_{snow} decreasing so rapidly? As mentioned in Section 4.2.4.1, the bulk method is more of a diagnostic tool with current weather variables as input. This means that turbulent heat fluxes are calculated for a snapshot in time without knowing how these variables are changing in time. In addition, the bulk method has no way of representing processes such as countergradient fluxes.

Figure 26 compares hourly mean turbulent heat fluxes calculated from the bulk and EC methods. Keep in mind, the EC data are unpublished, have not been peer reviewed, and the accuracy of these data is not fully known. In Figure 26B we see that bulk SHF is always downward with a minimum value at 11am. This makes sense since T_a is usually warmer than T_{snow}. The EC method shows large upward SHF values from 8am to 5pm which is opposite of the bulk method. This has not yet been validated but this may be a countergradient flux and

represents a major discrepancy between the two methods. Lapo, 2019 suggest though, that depending on the height at which EC measurements are taken, countergradient fluxes may not be transferring heat away from the surface. LHF in both methods is upward but is much greater in magnitude in the EC method. This suggests that sublimation is much stronger than what is represented by the bulk method. Figure 26C shows the total turbulent heat flux for both methods as solid lines and with the addition of NR as the dashed lines. Again, we see large upward combined turbulent heat flux during most of the daylight hours in the EC method and slight upward turbulent heat flux midday in the bulk method. With NR, magenta line, added to bulk turbulent heat fluxes we see large downward heat flux during the day that should warm the snow surface and upward heat flux overnight that should cool the snow surface. The timing of the bulk downward flux is not fully consistent with the mean diurnal cycle of T_{snow}. With the EC turbulent heat fluxes, we see mostly upward heat flux throughout the day when NR is added, with a small downward heat flux in the morning. This is also inconsistent with the diurnal cycle of T_{snow} during some times of the day.

One way to estimate the residual turbulent heat flux needed to change T_{snow} is to solve for total SEF, given the change in T_{snow}, and then subtract NR. One can imagine an equation such as:

$$SEF = \frac{dT_{snow}}{dt} * C_i * \rho_s * h \qquad (21)$$

where $\frac{dT_{snow}}{dt}$ is the time rate of change [s] of T_{snow} [K], C_i is the specific heat of ice [J kg^{-1} K^{-1}], ρ_s is the snow density [kg m^{-3}], and h is the depth of snow [m] that is subject to the temperature change. Because C_i, ρ_s, and h are difficult to calculate, they can be estimated as a proportionality constant, α. Because α is unknown I performed a least-squares fit between $\frac{dT_{snow}}{dt}$ and SEF (Figure 26A) and found the α to be 164,900. If we estimate C_i to be 2,108 J kg^{-1} K^{-1}, ρ_s to be 50

kg m^{-3}, and h to be 0.2 m, estimated α would be approximately 21,000 J K^{-1} m^{-2}. Therefore, α is eight times larger than estimated α, but is estimated from the hourly mean over all CUES data with snow. Each hourly value of $\frac{dT_{snow}}{dt}$ was then multiplied by α to find the estimated hourly SEF needed to return the hourly mean T_{snow} shown in Figure 26E. NR was then subtracted from the estimated hourly value of total SEF returning the estimated residual turbulent heat fluxes (Figure 26D). With NR added we see much better alignment with how T_{snow} changes. Comparing bulk residual turbulent heat flux plus NR in Figure 26D to bulk turbulent heat flux plus NR in Figure 26C we see that the residual turbulent heat flux calculation describes the evolution of T_{snow} much better. The probable conclusion is that the bulk method is not able to resolve local turbulence or instability during the early afternoon hours between the ground and the sensors like the EC method.

To see how well this process performed at an hourly level, I performed the same analysis for a single day. The dates of the EC data I was given were limited to one water year. However, I found that 06 April 2020 was in both the EC data and above the 95th percentile LHF threshold. Figure 27 is the same as Figure 26 but for 06 April 2020. Figure 27A is the least-squares fit between $\frac{dT_{snow}}{dt}$ and SEF. This time, α was found to be 30,800 which is much more consistent with the estimated α. In Figure 27B we see that EC LHF is the dominant flux during the morning and evening hours and may represent large time periods of sublimation. EC SHF is again shown to be upward during daylight hours. The scale of the plot is deceiving for the bulk turbulent fluxes, but SHF reaches a maximum of 50 W m^{-2} downward at 4pm, with LHF reaching a maximum of 27 W m^{-2} downward, also at 4pm. In fact, there is only one hour when bulk SHF is upward and two hours when bulk LHF is upward. Figure 27C shows the total turbulent heat flux for both methods as solid lines and with the addition of NR as dashed lines. We again see large

upward turbulent heat flux for most of the day from the EC method and close to zero or downward turbulent heat flux from the bulk method. After calculating α using equation 21 and estimating SEF the dashed blue line in Figure 27D is more consistent with T_{snow} in Figure 27E. Comparing bulk residual turbulent heat flux plus NR in Figure 27D to bulk turbulent heat flux plus NR in Figure 27C, we see that the residual turbulent heat flux calculation describes the evolution of T_{snow} much better. The only times bulk turbulent heat flux plus NR should be downward is 6am to 9am and 10pm. Bulk turbulent heat flux plus NR in Figure 27C suggests that T_{snow} should be warming during most of the daylight hours. Because T_{snow} drops so dramatically in the afternoon and evening, I expected upward bulk residual turbulent heat flux plus NR in Figure 27D to be more negative. I again believe the probable conclusion is the that bulk method is not able to resolve local turbulence or instability during the early afternoon hours between the ground and the sensors like the EC method.

More research is needed to understand which method, or even a combination of methods, would work best at CUES. The bulk method is strictly a down gradient calculation without a way to resolve countergradient fluxes. The EC method has difficulties in complex terrain with complex wind patterns. Therefore, it may be that actual turbulent heat fluxes lie somewhere between the two methods. If the EC method is resolving countergradient fluxes, it may be worth investigating the appropriate height at which the method measures a SEF that more closely follows the evolution of T_{snow}. Because the EC measurement height above the snow is also an important factor when calculating turbulent heat fluxes, one suggestion would be to install multiple sensors at different heights, maintain those heights above the snow throughout the season, and then compare to each other and the bulk method.

5 Sensitivity Study

Because the CUES platform is located at such a high elevation on the lee side of the Sierra it may not be representative of lower elevation and warmer locations within the Feather and Yuba River watersheds. I created a simple sensitivity study, using data from CUES, to look at how sensitive LHF is to temperatures typical of the Feather and Yuba River watersheds. When increases or decreases are shown for all data, it is in comparison to the CUES results. When increases or decreases are shown for data with only DLHF, it is in comparison to all data, with snow, when T_a and T_{Snow} were increased by the specified amount.

5.1 Methods

The first step was to identify typical T_a within the Feather and Yuba River watersheds during ARs (Table 6). I downloaded hourly T_a data at 9 stations within the Feather River watershed and 6 stations within the Yuba River watershed (Figure 9) from 1 October 2016 to 31 May 2021 from the CDEC website (https://cdec.water.ca.gov/dynamicapp/staSearch). I chose these locations based on elevation and the likelihood of that station receiving snow on at least a semi regular basis throughout the cool season. The mean hourly T_a at CUES during ARs during the cool season is -0.6° C. All but one station is shown to be warmer than CUES with the largest difference being greater than +5° C. Therefore, I chose to run the following analysis twice, first with a T_a increase of 2.5° C and then with a T_a increase of 5° C. Two datasets based on the one-minute CUES data were then created. For each dataset, both T_a and T_{snow} were raised by 2.5° C or 5° C with T_{snow} capped at 0° C. To keep the sensitivity study simple, and since I was not looking at any specific location, I did not change the other measured meteorological variables collected

from CUES. I recalculated the EB terms per Section 3.1 and ran the same analysis techniques, with the same thresholds, as for the non adjusted CUES data.

Because the Sierra are lacking T_{Snow} and full radiation measurements, I was unable to study any specific location within the Feather and Yuba River watersheds. Therefore, for the sensitivity study I was forced to use data from CUES that is not fully representative of either watershed. Lower elevation locations should not only be warmer, but all radiation terms, RH, IVT, and wind speed will be different in space and time. This sensitivity study is therefore lacking and is only meant to be a gage on whether placing new equipment on existing weather stations is warranted so that condensational heating of snow at a more appropriate location may be understood.

5.2 Increase of 2.5° C Results

Table 10 shows the monthly frequency of daily mean DLHF over all water years after raising the air and snow surface temperature by 2.5° C. DLHF occurred 20% of the time with the months of November through March having the greatest frequency. This represents a 5% decrease in the number of days with DLHF. The spring months of May and June are warmer than mid-winter, with T_d possibly greater than T_{Snow}, but with a lot of missing T_{Snow} data during these months LHF is largely unknown.

Figure 28 shows the daily mean distributions of each SEF term to show how important LHF is to the total SEF after a 2.5° C increase in T_a and T_{Snow}. Figure 28A is the daily mean distributions of all data with snow. SHF still appears to be the largest term in the total SEF with both median and mean values increasing to 19.6 W m^{-2} and 29.4 W m^{-2}, respectively. Median and mean values of LHF both decrease to -4.8 W m^{-2} and -11.6 W m^{-2}, respectively, thereby decreasing the possibility of DLHF. The 75th percentile of LHF decreases to –0.6 W m^{-2} showing,

again, that less than 25% of LHF is downward. AHF rises slightly to 0.25 W m^{-2} due to the temperature of the precipitation warming and has again been omitted from further results. Radiation terms were unchanged and so values of NR did not change. After adding the EB terms, the median and mean total SEF both decrease to 9.3 W m^{-2} and 12.5 W m^{-2}, respectively. Overall, the total SEF is still downward most of the time with very small changes to total SEF. Figure 28B is the daily mean distributions of all data with snow, but only for days with DLHF. SHF has less influence on total SEF and is always downward with a minimum value of 1.1 W m^{-2}. The magnitude of SHF decreases with median and mean values of SHF 14.8 W m^{-2} and 19.8 W m^{-2}, respectively. LHF is of course all downward with a 75th percentile value of 5.9 W m^{-2}. Because days with DLHF may have changed, the distribution of NR also changes. The median and mean NR change to -6.8 W m^{-2} and -6.2 W m^{-2}, respectively. Finally, the median and mean values of total SEF on days with DLHF change to 15.1 W m^{-2} and 18.7 W m^{-2}, respectively. Total SEF is mostly downward and, when compared to the CUES data, increases on days when daily mean LHF is downward. What is noticeable in both plots is that the purple star, representing the mean of each EB term in the sensitivity study, is not much different from the mean of the CUES data. Overall, raising T_a and T_{Snow} by 2.5° C does not cause a significant increase of latent heat into the snowpack.

After identifying the distributions of each SEF term on days with DLHF the percent contribution of DLHF to the total SEF was identified to see if DLHF was ever the most important term in the total SEF. Figure 29 shows the percent contribution of each SEF term on each day when daily mean LHF was downward. The black line with dots indicates the percent contribution of DLHF. The horizontal dashed black line represents the mean DLHF percent contribution of 10.3%. The grey horizontal dashed lines represent the mean percent contribution of the other SEF terms, as shown. DLHF contributes more to total SEF but is still much less than the contributions

of NR and SHF. Of the 119 days when LHF was downward, it is never the most important term in the total SEF.

Figure 30 shows the daily mean PDFs of other meteorological variables after raising T_a and T_{Snow} by 2.5° C. As expected, the distributions of T_a, T_d, and T_{Snow} have increased in the positive direction. On days with DLHF, T_a is still cooler than average, but not as cool as the unadjusted CUES data. T_{Snow} reaches 0° C more often which means that ΔT should be larger. ΔT does increase when compared to CUES which will make the atmosphere slightly more stable. However, there are also less values close to zero, which still allows SHF. The dewpoint depression decreases which increases RH. T_d is warmer than 0° C more often and with sufficiently large enough RH such that Δe is positive, DLHF occurs more often. As seen in Figure 30, this is occurring with DLHF increasing slightly. Finally, DLHF does occur slightly more often on days with IVT greater than 250 kg m^{-1} s^{-1} but mean IVT decreases. So again, this does not indicate that DLHF occurs more often with increased IVT. However, IVT values will be larger when a more suitable location is chosen to study further.

Table 11 lists daily mean values for meteorological variables shown in Figure 30 for all thresholds. Daily mean LHF is downward in more than only the DLHF threshold and LHF > 95th percentile threshold. All thresholds except for the IVT threshold still have IVT values well under the 250 kg m^{-1} s^{-1} AR threshold. SHF is downward under all thresholds and much larger in magnitude than NR and LHF, again indicating that it is the primary driver of SEF. SEF is still positive under all thresholds, smallest under the RH threshold, and relatively large during the LHF threshold. T_d is greater than T_{Snow} when looking at the DLHF, T_d, and RH thresholds. LHF is downward under the T_{Snow} threshold but is very small. The T_{snow} threshold is important since T_{Snow} close to 0° is needed for substantial melt. However, with LHF only 1.2 W m^{-2} significant condensational heating of the snowpack is not expected. These results indicate that under some

thresholds, LHF is downward more often but likely not large enough to cause substantial snowmelt.

5.2.1 Threshold Composites

When looking at the composite plots, NR, wind speed, RH, and IVT were not adjusted for the sensitivity study. However, the composites of those variables may change under each threshold since the actual days when the threshold is met may change when compared to the unadjusted CUES data. Figures 31-33 are the hourly composite plots of how each meteorological variable changes in time when daily mean IVT > the 95th percentile, when daily mean RH > the 95th percentile, and when daily mean LHF > the 95th percentile, respectively, after raising T_a and T_{Snow} by 2.5° C. In all plots, the results are very similar to the unadjusted CUES data. Because IVT and RH were not changed, the same days are shown as for the unadjusted CUES data. Under the LHF threshold though, the days when the threshold is met are different.

Figures 34-36 show the combined hourly composite plots of T_a, T_d, and T_{Snow} when daily mean IVT > the 95th percentile, when daily mean RH > the 95th percentile, and when daily mean LHF > the 95th percentile, respectively, after raising T_a and T_{Snow} by 2.5° C. The main takeaway here is that T_d is greater than T_{Snow} more often, allowing for more times of DLHF at greater magnitudes than the unadjusted CUES data.

5.3 Increase of 5° C Results

Table 12 shows the monthly frequency of daily mean DLHF over all water years after raising the air and snow surface temperature by 5° C. In the sensitivity study, DLHF occurs 27.2% of the time with the months of November through March having the greatest frequency.

This represents a modest 2.2% increase in the number of days with DLHF. The spring months of May and June are warmer than mid-winter, with T_d possibly greater than T_{Snow}, but with a lot of missing T_{Snow} data during these months LHF is largely unknown.

Figure 37 shows the daily mean distributions of each SEF term to show how important LHF is to the total SEF after a 5° C increase in T_a and T_{Snow}. Figure 37A is the daily mean distributions of all data with snow. SHF again appears to be the largest term in the total SEF with both the median and mean values increasing to 23.9 W m^{-2} and 33.6 W m^{-2}, respectively. This is mostly due to larger values getting larger. The 25th percentile does not change much but the 75th percentile increases by 6.7 W m^{-2}. For LHF, the median decreases to -3.9 W m^{-2} and the mean increases to -9.5 W m^{-2}. Again, larger values are getting larger, but the median and mean do not change very much. The 75th percentile of LHF increases to 0.3 W m^{-2} again showing that LHF is downward more than 25% of the time. AHF increases to 0.5 W m^{-2} due to further warming of the precipitation temperature but is still small and has again been omitted from further results. Radiation terms were unchanged and so values of NR did not change. After adding the EB terms, the median and mean total SEF both increase to 10.5 W m^{-2} and 18.9 W m^{-2}, respectively. Overall, total SEF is downward most of the time. The larger positive SHF values cause the larger positive values of the total SEF to increase thereby lengthening the positive side of the distribution. This is also shown by the purple star representing the mean of each EB term in the sensitivity study. Figure 37B is the daily mean distributions of all data with snow, but only for days with DLHF. SHF now has a much larger influence on total SEF and is always downward with a minimum value of 1.1 W m^{-2}. The median SHF increases slightly to 24.6 W m^{-2} while the mean SHF decreases to 31.5 W m^{-2}. LHF is of course all downward with the 75th percentile increasing quite a bit to 13.2 W m^{-2}. Because days with DLHF may have changed, the distribution of NR also changes. The median and mean NR change to -5.3 W m^{-2} and -3.6 W m^{-2},

respectively. Finally, the median and mean values of total SEF on days with DLHF change to 29.8 W m^{-2} and 39.4 W m^{-2}, respectively. It is tough to see in the plot, but mean values of SHF and LHF have doubled when compared to the unadjusted CUES data. Total SEF and LHF are now clearly much more positive with respect to the unadjusted CUES data. The purple star representing the mean of each EB term in the sensitivity study has increased significantly on the total SEF distribution when compared to the unadjusted CUES data. With the much larger positive distribution of total SEF, warming/melting of the snowpack may be much more likely.

After identifying the distributions of each SEF term on days with DLHF the percent contribution of DLHF to the total SEF was identified to see if DLHF was ever the most important term in the total SEF. Figure 38 shows the percent contribution of each SEF term on each day daily mean LHF was downward. The black line with dots indicates the percent contribution of DLHF. The horizontal dashed black line represents the mean DLHF percent contribution of 14.7%. The grey horizontal dashed lines represent the mean percent contribution of the other SEF terms, as shown. DLHF contributes more to total SEF but is still much less than the contributions of NR and SHF. Of the 162 days when LHF was downward, it is the most important term in the total SEF one time.

Figure 39 shows the daily mean PDFs of other meteorological variables after raising T_a and T_{Snow} by 5° C. Distributions of T_a, T_d, and T_{Snow} have further increased in the positive direction. On days with DLHF, T_a is not much cooler than the average of all the data with snow. T_{Snow} reaches 0° C quite a bit more often which means that ΔT should again be larger. ΔT does increase when compared to unadjusted CUES data which will make the atmosphere more stable. SHF values increase when compared to the unadjusted CUES data. This makes sense since T_{Snow} is capped at 0° C and T_a is now larger than 0° C. The mean dewpoint depression decreases, increasing RH. We see that T_d is now warmer than 0° C much more often. Therefore, Δe is easily

more positive than the unadjusted CUES data and DLHF is more likely. As seen in Figure 39, this is occurring with a large increase in DLHF. Finally, DLHF does occur slightly more often on days with IVT greater than 250 kg m^{-1} s^{-1}, but mean IVT is still below 100 kg m^{-1} s^{-1}. So again, this does not indicate that DLHF occurs more often with increased IVT. Again, IVT values may be larger when a suitable windward location is chosen to study further.

Table 13 lists daily mean values for meteorological variables shown in Figure 39 for all thresholds. Interestingly, LHF is now downward in all limiting thresholds. However, the largest IVT, outside of the IVT threshold, is no larger than 132 kg m^{-1} s^{-1}. This will change once a more suitable location is chosen to study. SHF is downward under all thresholds and much larger in magnitude than NR and LHF, again indicating that it is the primary driver of SEF under each threshold. SEF is still downward under all thresholds, smallest when LHF is upward, and largest under the LHF threshold. T_d is now greater than T_{Snow} under all limiting thresholds leading to DLHF under each threshold except, of course, upward LHF. Under the T_{Snow} threshold, T_{Snow} is almost always 0° C with T_a of 5.5° C. In fact, under all thresholds, except for the DLHF threshold, T_{Snow} is between -1° C and 0° C which is a more ideal condition for substantial snowmelt. At this point, even though DLHF is not the most important term in the total SEF, meteorological conditions may be sufficient for significant snowmelt.

5.3.1 Threshold Composites

When looking at the composite plots, NR, wind speed, RH, and IVT were not adjusted for the sensitivity study. However, the composites of those variables may change under each threshold since the actual days when the threshold is met may change when compared to the CUES data. Figures 40-42 are the hourly composite plots of how each meteorological variable

changes in time when daily mean IVT > the 95th percentile, when RH > the 95th percentile, and when LHF > the 95th percentile, respectively, after raising T_a and T_{Snow} by 5° C. In all plots, the results are again very similar to the unadjusted CUES data. Because IVT and RH were not changed, the same days are shown as for the unadjusted CUES data. Under the LHF threshold though, the days when the threshold is met are slightly different.

Figures 43-45 show the combined hourly composite plots of T_a, T_d, and T_{Snow} when IVT > the 95th percentile, when RH > the 95th percentile, and when LHF > the 95th percentile, respectively, after raising T_a and T_{Snow} by 5° C. Again, the main takeaway here is that T_d is greater than T_{Snow} more often, allowing for more times of DLHF at greater magnitudes than the unadjusted CUES data.

6 Conclusions

Meteorological measurements are extensive throughout the Sierra Nevada Mountains of California. However, it was difficult to find a location where turbulent heat flux measurements over snow could be easily obtained or measured. One of the few locations in the western U.S. with a suite of readily available measurements is the CUES platform on Mammoth Mountain, California. The platform sits at a high elevation close to the Sierra crest on the lee side of the mountain range. However, the location of interest is the Feather and Yuba River watersheds located on the windward side of the Sierra crest at much lower elevations. CUES was shown to have cooler hourly mean T_a and T_d during AR conditions. More importantly, the mean T_d during ARs is above 0° C at most stations within the Feather and Yuba River watersheds.

Calculating turbulent heat fluxes using the bulk method is straightforward. However, the z_0 term, the use of the Ri number for stability, and the inability for the bulk method to resolve

countergradient effects are likely the greatest sources of error. Because wind speed is only available at one level, I was unable to easily estimate z_0. Using an empirical best fit to data from the EC method likely introduced even more error, with the value of z_0 obtained being at the higher end of values found in the literature. However, without more sophisticated methods to estimate z_0 the value I found is valid and led to turbulent heat fluxes consistent with other studies. With a mean ΔT at CUES of approximately 7° C during the cool season, it is not uncommon to have unreasonably large Ri numbers and stability corrections that essentially turn off turbulent heat fluxes. Some EB models set this parameter to zero if it is over some critical value, however, this was not performed here. Further research may identify a set of critical meteorological values and Ri numbers that lead to times of greatest DLHF. If this exists it could greatly enhance our knowledge of whether large DLHF is expected over specific snow-covered areas and help improve hydrologic models and flood forecasts.

Daily mean bulk method LHF at CUES was shown to be -9.8 W m^{-2}. This implies that the majority of LHF is upward, with sublimation being more likely. Daily mean DLHF was shown to occur 25% of the time. On these days, daily mean LHF was 3.0 W m^{-2} with an average daily contribution to the total SEF of approximately 10%. Daily mean DLHF was also shown to never be the most important term in the total SEF. With a daily mean T_{Snow} of -10.6° C the energy supplied by all downward fluxes would first need to warm T_{Snow} to 0° C before significant melt could take place. This may occur during the fall or late spring with a warmer T_{snow} but because the snowpack at CUES can be very deep and cold, mid-winter periods of condensational heating would likely be limited to small amounts of surface melting. As this meltwater percolates through the cold snowpack, it is likely to refreeze before running off.

The three hourly composite plots I studied show a similar pattern for when DLHF occurs when the bulk method was used. Because mid-winter temperatures at CUES are typically below freezing, T_d is often not greater than T_{Snow}. However, late on day 0 into day 1 T_{Snow} begins to rapidly decrease. At the same time IVT, RH, and T_d also begin to decrease. This causes T_d to be very close to, or even greater than, T_{Snow} such that Δe is positive leading to DLHF. This suggests that the largest values of DLHF occur shortly after AR conditions have passed.

IVT values greater than 250 kg m^{-1} s^{-1} do not occur often at CUES due to its location on the lee side of the Sierra. Depending on a given ARs orientation, orographic lift on the windward side of the Sierra crest has likely wrung out most of the moisture it brought. After estimating turbulent heat fluxes using the bulk method, and when daily mean IVT > 95th percentile, daily mean LHF was -3.9 W m^{-2}. This signifies that even during possible AR conditions, sublimation is more likely to occur. After estimating turbulent heat fluxes using the bulk method, and after looking at hourly composites when daily mean IVT > 95th percentile, the magnitude of DLHF is very small and is shown to occur after peak IVT. This small flux is likely not a large contributor to snowmelt at CUES when IVT values are large. In addition, when LHF > 95th percentile, daily mean LHF is only 3.0 W m^{-2}. Again, this may be too small to contribute to significant amounts of snowmelt. Small DLHF values at CUES are mostly attributed to the platform's location at an elevation such that T_a and T_d are below freezing during much of the cool season with T_d often cooler than T_{Snow}.

With the limited amount of EC data I was given, I found that daily mean DLHF never occurred during WY2020, which may be due to countergradient effects. LHF seems to contribute much more to the total SEF, but I feel that this is inconclusive due to the lack of data. Once additional EC data are available a more robust comparison of the two methods would be possible.

In addition, I feel that the EC method may be overestimating upward turbulent heat fluxes because of the countergradient effects.

When comparing bulk turbulent heat fluxes to EC turbulent heat fluxes, it was found that the EC method may be resolving countergradient turbulent heat fluxes. The hourly composite plot of bulk SHF was shown to be downward for the entire day while the hourly composite plot of EC SHF was downward at night and large and upward during the day. SHF from the EC method seems to be counter-intuitive since T_a is usually warmer than T_{snow}. Local wind turbulence, the height of the EC sensor, and unknown unstable layers between the EC sensor and the snow surface may be creating countergradient fluxes that make for difficulties in accurately measuring turbulent heat fluxes. It may also be the case that the bulk method is overestimating downward turbulent heat fluxes while the EC sensor at CUES may not be at the correct height above the snow surface throughout the cool season for completely accurate measurements. I am unaware of whether the EC sensor is moved vertically throughout the cool season to maintain a constant height above the snow surface as this could bias EC measurements.

Turbulent heat fluxes shown for CUES may be less than expected for locations in the Feather and Yuba River watersheds. Therefore, two simple sensitivity studies were performed using data from CUES. T_a and T_{Snow} were raised by 2.5° C and 5° C, while capping T_{Snow} at 0° C, and turbulent heat fluxes were recalculated. The results after a 5° C increase show that DLHF may occur under all limiting thresholds. However, the study has many limitations. I held all radiation terms, RH, wind speeds, and IVT the same as at CUES. In general, the radiation terms will influence all temperatures, locations within the Feather and Yuba River watersheds will have much larger IVT values and depending on the location of an AR feature or local topography, wind speeds may be quite different. If additional research is warranted, at a minimum, incoming and outgoing shortwave radiation, incoming and outgoing longwave radiation, and T_{Snow} sensors

could be installed onto existing weather stations in more appropriate locations. It may also be helpful to use a more sophisticated EB model with a snow component, to fully understand how LHF and T_{snow} behave. This will help to not only better understand their effects on an existing snowpack during an AR and but will also help estimate the amount of possible snowmelt runoff.

Tables

Table 1: List of variables gathered from the CUES station at one-minute resolution with percent missing. When snow is not present, snow surface temperature data show as missing, thereby increasing the percent missing.

Variable	Instrument	Missing
Incoming Solar Radiation [W m^{-2}]	Eppley Lab Precision Spectral Pyranometer	0.3%
Reflected Solar Radiation [W m^{-2}]	Eppley Lab Precision Spectral Pyranometer	0.3%
Incoming Longwave Radiation [W m^{-2}]	Eppley Lab Precision Infrared Longwave Radiometer	0.3%
Air Temperature [C]	Campbell HMP 45C (Radiation Shielded)	1.3%
Snow Surface Temperature [C]	Apogee SI-111 Thermal Radiometer	35.5%
Relative Humidity [%]	Campbell HMP 45C (Radiation Shielded)	1.1%
Barometric Pressure [mb]	Unknown	0.9%
Wind Speed [m s^{-1}]	RM Young bird Anemometer	12.3%
Wind Direction [°]	RM Young bird Anemometer	5.4%

Table 2: List of variables gathered from the CUES station, at five-minute resolution with percent missing. When snow is not present, snow depth data show as missing, thereby increasing the percent missing.

Variable	Instrument	Missing
Snow Water Equivalent [cm]	Department of Water Resources Snow Pillow	3.0%
Snow Depth [cm]	Ultrasonic Depth Pinger on Remote Boom	19.8%

Table 3: RMSE values for different roughness lengths using hourly latent heat flux estimated from the bulk-aerodynamic method and hourly latent heat flux using the eddy covariance method. Roughness length value that minimizes RMSE is shaded.

Roughness Length [m]	RMSE
0.001	49.74
0.002	48.98
0.003	48.49
0.004	48.13
0.005	47.85
0.006	47.61
0.007	47.42
0.008	47.25
0.009	47.11
0.01	46.98
0.02	46.38
0.03	46.39
0.04	46.72
0.05	47.28
0.06	48.00
0.07	48.85
0.08	49.80
0.09	50.84
0.1	51.96

Table 4: Dates with at least 15.24 cm of snow present at CUES

Begin	End
29 November 2016	6 July 2017
16 November 2017	4 June 2018
22 November 2018	8 July 2019
27 November 2019	1 June 2020
8 November 2020	18 May 2021

Table 5: Daily mean values of select variables collected/calculated at CUES.

Variable	All Data	With Snow Present	With Snow Present and Missing Data Removed
Downward SWR [W m^{-2}]	215	193	134
Upward SWR [W m^{-2}]	101	128	112
Downward LWR [W m^{-2}]	241	232	227
Upward LWR [W m^{-2}]	274	273	273
Net Radiation [W m^{-2}]	-8	-7	-5.7
Relative Humidity [%]	49	56	59
Air Temperature [C]	4.0	0.1	-2.7
Dewpoint Temperature [C]	-8.3	-9.8	-12.0
Snow Surface Temperature [C]	-8.8	-9.0	-9.0
Wind Speed [m s^{-1}]	3.1	3.3	3.3
IVT [kg m^{-1} s^{-1}]	50	54	55
Sensible Heat Flux [W m^{-2}]	27.7	28.0	28.0
Latent Heat Flux [W m^{-2}]	-10.4	-9.8	-9.8
Advective Heat Flux [W m^{-2}] (On days with precipitation)	1.7	0.7	0.2
Surface Energy Flux [W m^{-2}]	11.7	12.8	12.8
Richardson Number	2.1	2.1	2.1
Number of Days in Dataset	1,703	1,030	595

Table 6: Mean hourly air and dewpoint temperatures during atmospheric rivers at various weather stations within the Feather and Yuba River watersheds and at CUES during the cool season.

Station	Elevation	Mean T_a During ARs	Mean T_d During ARs	ΔT_a with CUES During ARs	Mean Dewpoint Depression During ARs
CUES	2,940 m	-0.6° C	-1.8° C	-	1.2° C
GRZ	2,103 m	-0.1° C	-	+0.5° C	-
CSL	2,103 m	2.0° C	-	+2.6° C	-
JDP	2,076 m	2.2° C	0.05° C	+3.0° C	2.2° C
GOL	2,057 m	0.5° C	-	+1.1° C	-
RCC	1,975 m	1.6° C	-	+2.2° C	-
RTL	1,892 m	-0.8° C	-	-0.2° C	-
HRK	1,890 m	1.1° C	-0.3° C	+1.8° C	1.4° C
BOL	1,642 m	3.4° C	-	+4.0° C	-
LSP	1,571 m	4.0° C	2.9° C	+5.0° C	1.1° C
WWD	1,570 m	2.0° C	1.1° C	+4.3° C	0.9° C
CHS	1,379 m	3.7° C	0.1° C	+3.8° C	3.6° C
CSH	1,378 m	5.9° C	3.5° C	+6.7° C	2.4° C
WTC	1,317 m	5.9° C	4.8° C	+9.4° C	1.1° C
TAY	1,079 m	6.6° C	4.2° C	+5.1° C	2.4° C
QYR	1,066 m	6.5° C	4.7° C	+6.2° C	1.8° C

Table 7: Monthly frequency of daily mean DLHF over all water years using the bulk-aerodynamic method.

Month	Daily Mean LHF Values	Daily Mean DLHF Values	Frequency of DLHF
November	43	13	30.2%
December	118	33	28.0%
January	99	30	30.3%
February	111	30	27.0%
March	114	31	27.2%
April	81	8	9.9%
May	27	4	14.8%
June	2	0	0.0%
Total	595	149	25.0%

Table 8: Daily mean values for select variables at CUES, over snow, under different thresholds. Turbulent heat fluxes were estimated using the bulk-aerodynamic method.

Meteorological Variable	With Snow Present	With snow and Upward LHF	With snow and Downward LHF	T_d > 95th %ile [-3.7 C]	IVT > 95th %ile [139 kg m^{-1} s^{-1}]	LHF > 95th %ile [4.4 W m-2]	RH > 95th %ile [92.9 %]	SEF > 95th %ile [46 W m-2]	T_{Snow} > 95th %ile [-2.4 C]
Net Radiation [W m^{-2}]	-5.7	-5.6	-5.9	3.2	-5.6	-14.9	-0.3	6.3	6.9
Sensible Heat Flux [W m^{-2}]	28.0	32.0	16.1	17.8	21.9	30.7	2.7	75.8	24.0
Latent Heat Flux [W m^{-2}]	-9.8	-14.1	3.0	-1.9	-3.9	8.8	-1.0	-20.8	-12.4
Surface Energy Flux [W m^{-2}]	12.8	12.5	13.5	19.2	12.9	25.0	1.6	61.4	18.5
Wind Speed [m s^{-1}]	3.3	3.3	3.2	4.2	4.2	4.6	4.4	5.2	4.4
Air Temperature [C]	-2.7	-1.4	-6.5	-0.1	-1.5	-6.9	-3.3	-0.7	1.0
Dewpoint Temperature [C]	-12.0	-12.7	-9.9	-2.3	-4.9	-9.8	-4.0	-10.3	-3.2
Snow Surface Temperature [C]	-9.0	-8.4	-10.6	-2.1	-3.9	-10.7	-3.6	-6.3	-1.6
Relative Humidity [%]	58	51	79	87	82	83	95	56	78
ΔT [C]	6.2	6.9	4.2	1.9	2.4	3.8	0.3	5.6	2.5
Δe [hPa]	-0.4	-0.7	0.3	0.01	-0.1	0.4	0.01	-0.7	-0.4
IVT [kg m^{-1} s^{-1}]	55	51	66	122	181	66	132	50	110

Table 9: Same as Table 7 but using the eddy covariance method.

Month	Daily Mean LHF Values	Daily Mean DLHF Values	Frequency of DLHF
November	22	0	0%
December	0	0	0%
January	28	0	0%
February	27	0	0%
March	9	0	0%
April	6	0	0%
May	4	0	0%
June	21	0	0%
Total	97	0	0%

Table 10: Same as Table 7 but after raising the air and snow surface temperatures by 2.5° C.

Month	Daily Mean LHF Values	Daily Mean DLHF Values	Frequency of DLHF
November	43	10	23.3%
December	118	26	22.0%
January	99	24	24.2%
February	111	20	18.0%
March	114	25	21.9%
April	81	8	9.9%
May	27	6	22.2%
June	2	0	0.0%
Total	595	119	20.0%

Table 11: Same as Table 8 but after raising the air and snow surface temperatures by 2.5° C.

Meteorological Variable	With Snow Present	With snow and Upward LHF	With snow and Downward LHF	T_d > 95th %ile [-1.2 C]	IVT > 95th %ile [139 kg m^{-1} s^{-1}]	LHF > 95th %ile [5.8 W m-2]	RH > 95th %ile [92.9 %]	SEF > 95th %ile [49 W m-2]	T_{Snow} > 95th %ile [-0.6 C]
Net Radiation [W m^{-2}]	-5.7	-5.5	-6.2	3.2	-5.6	-4.1	-0.3	10.3	4.8
Sensible Heat Flux [W m^{-2}]	29.4	31.8	19.8	28.7	27.6	35.4	8.0	67.1	33.2
Latent Heat Flux [W m^{-2}]	-11.6	-15.6	4.6	7.4	-1.0	13.1	0.2	-8.6	1.2
Surface Energy Flux [W m^{-2}]	12.5	10.9	18.7	40.0	21.8	45.1	8.6	69.0	40.0
Wind Speed [m s^{-1}]	3.3	3.3	3.1	4.3	4.2	4.3	4.4	5.1	4.4
Air Temperature [C]	-0.2	0.6	-3.2	2.4	1.0	-1.0	-0.8	2.3	3.1
Dewpoint Temperature [C]	-9.7	-10.4	-6.9	0.1	-2.5	-3.5	-1.5	-5.1	-0.5
Snow Surface Temperature [C]	-6.6	-6.3	-8.2	-0.5	-2.0	-4.8	-1.5	-3.0	-0.3
Relative Humidity [%]	59	54	79	87	82	85	95	65	81
ΔT [C]	6.4	6.8	5.0	2.9	3.0	3.7	0.7	5.2	3.3
Δe [hPa]	-0.5	-0.8	0.4	0.3	-0.0	0.5	0.1	-0.4	0.0
IVT [kg m^{-1} s^{-1}]	55	53.0	63.6	122	181	96	132	64	121

Table 12: Same as Table 7 but after raising the air and snow surface temperatures by 5° C.

Month	Daily Mean LHF Values	Daily Mean DLHF Values	Frequency of DLHF
November	43	13	30.2%
December	118	27	22.9%
January	99	27	27.3%
February	111	23	20.7%
March	114	28	24.6%
April	81	27	33.3%
May	27	16	59.3%
June	2	1	50.0%
Total	595	162	27.2%

Table 13: Same as Table 8 but after raising the air and snow surface temperatures by 5° C.

Meteorological Variable	**With Snow Present**	**With snow and Upward LHF**	**With snow and Downward LHF**	**T_d > 95th %ile [1.2 C]**	**IVT > 95th %ile [139 kg m^{-1} s^{-1}]**	**LHF > 95th %ile [17.6 W m-2]**	**RH > 95th %ile [92.9 %]**	**SEF > 95th %ile [77 W m-2]**	**T_{Snow} > 95th %ile [-0.0 C]**
Net Radiation [W m^{-2}]	-5.7	-6.4	-3.6	3.2	-5.6	-6.0	-0.3	11.6	2.9
Sensible Heat Flux [W m^{-2}]	33.6	34.5	31.5	50.2	41.5	61.5	23.7	77.3	55.0
Latent Heat Flux [W m^{-2}]	-9.5	-17.1	10.6	32.6	13.7	37.0	14.9	25.8	21.2
Surface Energy Flux [W m^{-2}]	18.9	11.3	39.4	88.3	51.8	94.8	40.6	116	81.4
Wind Speed [m s^{-1}]	3.3	3.2	3.4	4.3	4.2	5.0	4.4	5.4	4.3
Air Temperature [C]	2.3	2.8	1.1	4.9	3.5	4.1	1.7	5.1	5.5
Dewpoint Temperature [C]	-7.3	-9.1	-2.7	2.6	-0.1	2.0	0.9	0.6	1.4
Snow Surface Temperature [C]	-4.7	-4.8	-4.2	-0.1	-0.9	-0.5	-0.4	-0.6	-0.0
Relative Humidity [%]	59	51	79	87	82	88	95	76	80
ΔT [C]	6.9	7.5	5.3	5.0	4.4	4.5	2.1	5.6	5.4
Δe [hPa]	-0.5	-0.9	0.6	1.4	0.6	1.2	0.7	0.7	0.8
IVT [kg m^{-1} s^{-1}]	55	47	77	122	181	128	132	89	120

Figures

Figure 1: Location Map of Mammoth Mountain Ski area and CUES

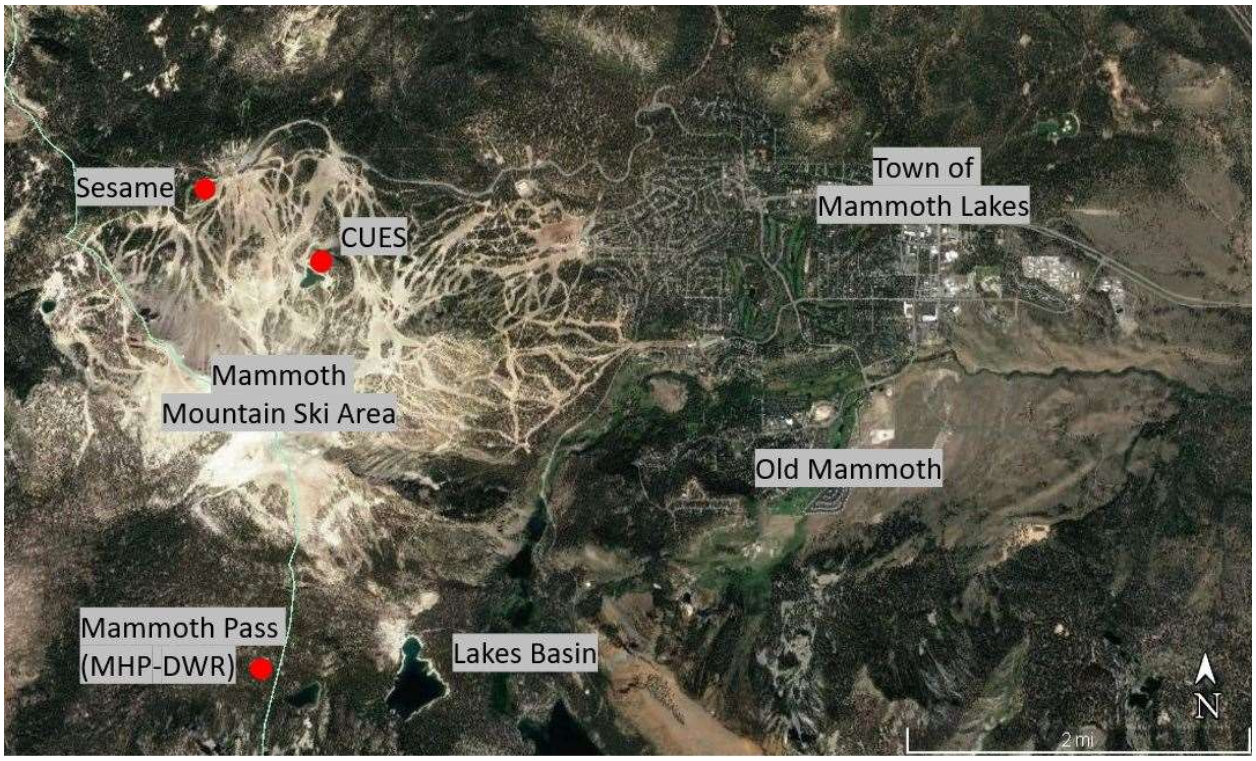

Figure 2: Vicinity Map of Mammoth Mountain Ski area and the location of the CUES snow study site.

Figure 3: The CUES platform in 2020 with its wide array of instruments. The movable arm is seen in the foreground. https://snow.ucsb.edu/index.php/2020/09/23/2020-cues-tlc/

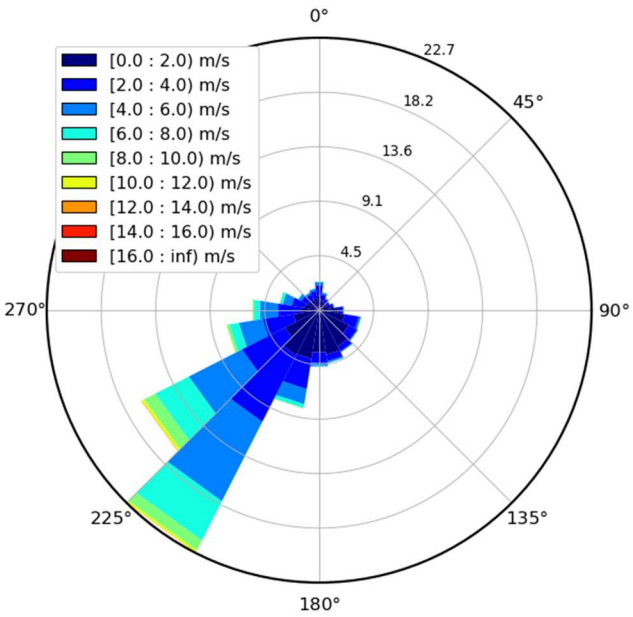

Figure 4: Wind rose using one-minute data from CUES from water year 2017 to 31 May 2021. The prevailing wind is from the southwest.

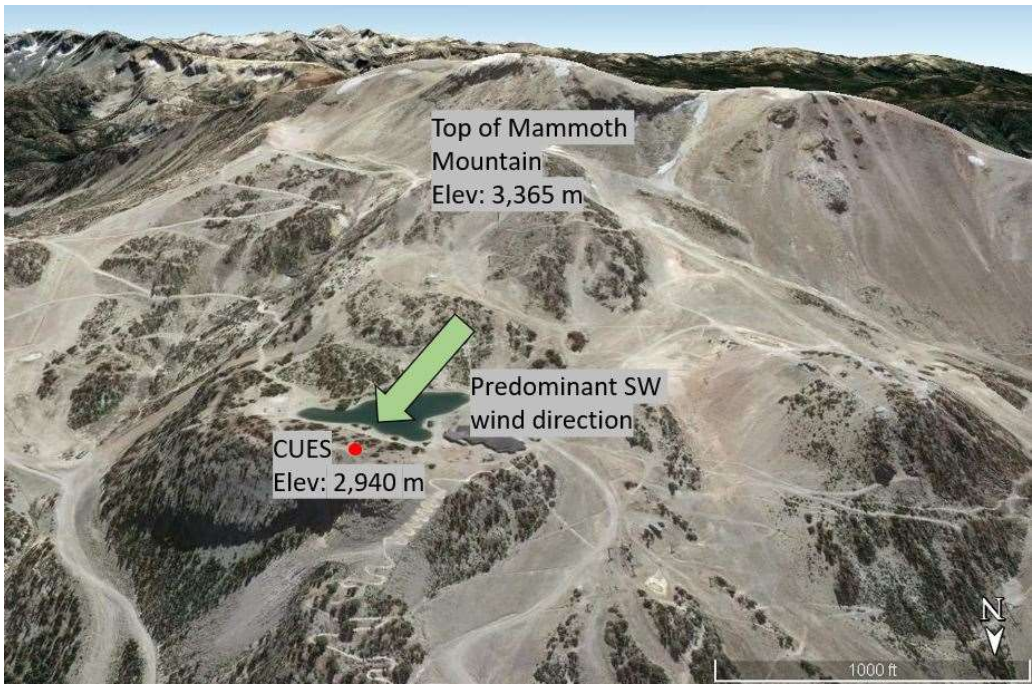

Figure 5: Google Earth image of Mammoth Mountain looking to the south. North is pointed down. The light green arrow shows the predominant wind direction.

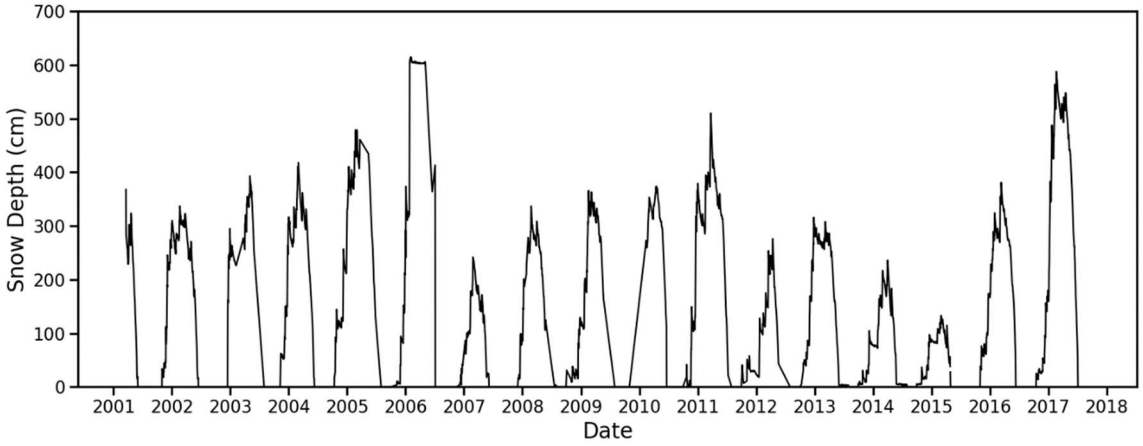

Figure 6: Daily snow depth at CUES. (Adapted from Bair, 2015)

Figure 7: Map of a portion of Central California showing grid points of the ERA5 reanalysis dataset as yellow circles. The red triangles represent the grid cells where data from the ERA5 reanalysis dataset were downloaded.

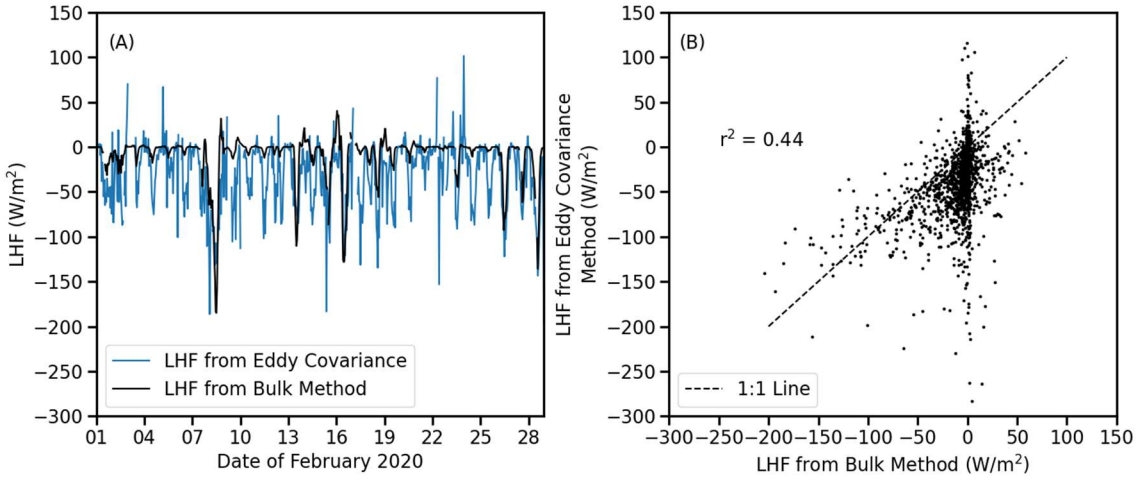

Figure 8: Best RMSE fit for roughness length z_0. (A) Hourly time series during February 2020 of latent heat flux, black line, calculated from the bulk-aerodynamic method with a z_0 value of 0.02 m overlaid onto a portion of latent heat flux, blue line, calculated from the eddy covariance method. (B) Scatterplot of eight months worth of latent heat flux data from the eddy covariance method vs. latent heat flux estimated using the bulk-aerodynamic method.

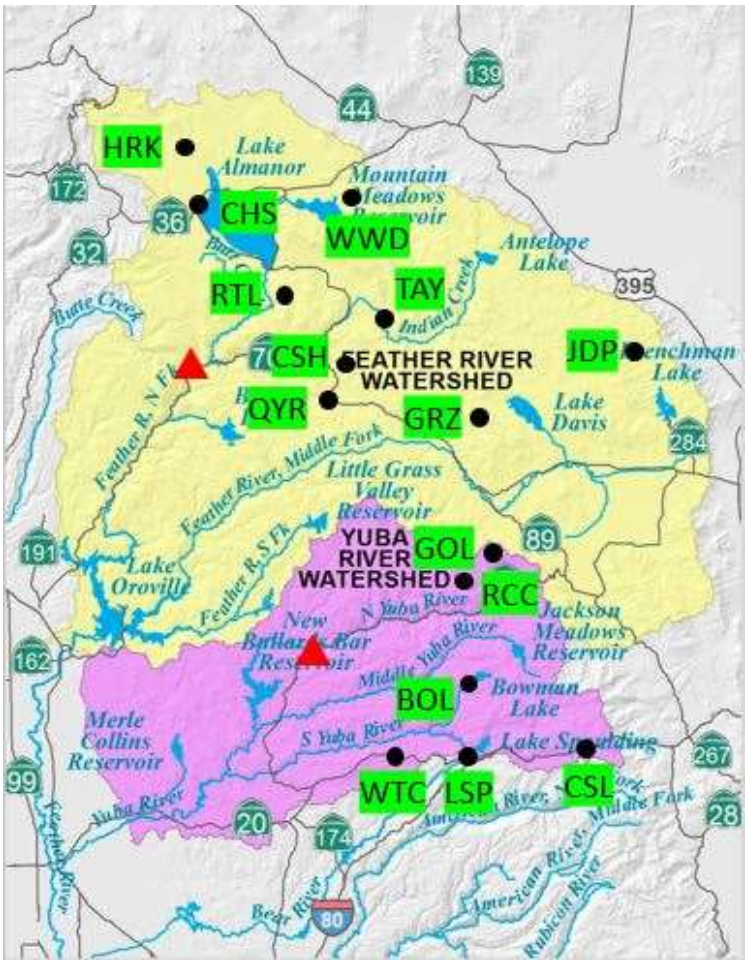

Figure 9: Map of the Feather River watershed in yellow and the Yuba River watershed in purple showing the location of weather stations from the CDEC website. The red triangles represent the location of the ERA5 IVT grid cell used in each watershed.

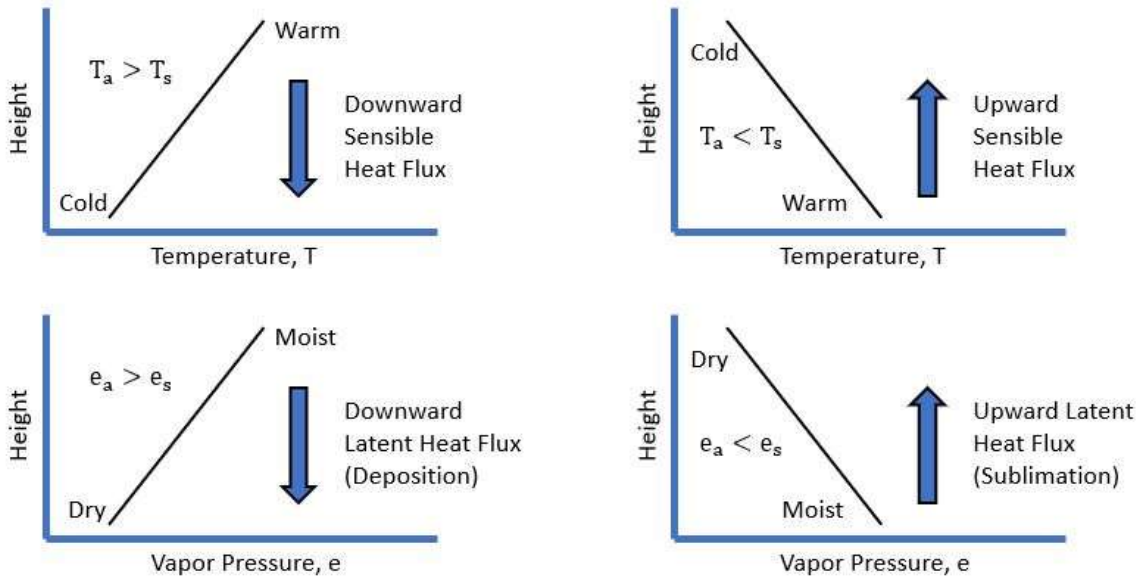

Figure 10: Schematics of how the bulk-aerodynamic method works.

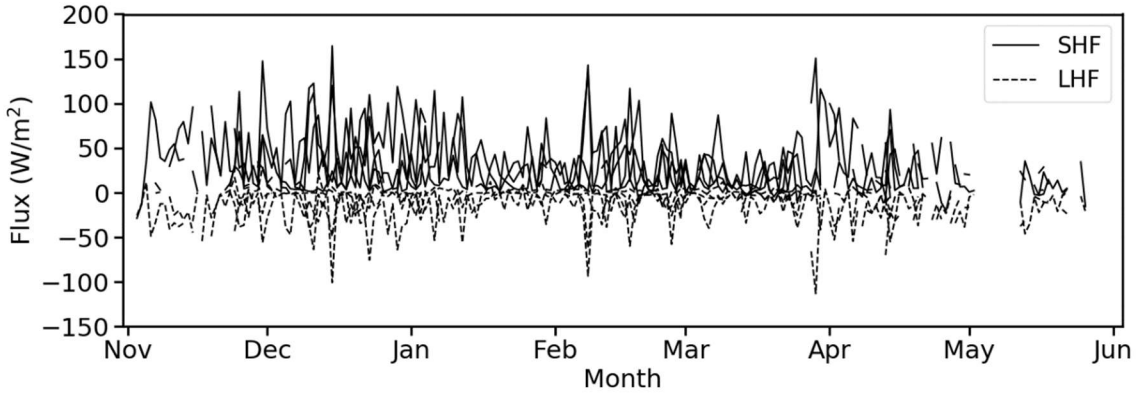

Figure 11: Composite plot of daily mean SHF and LHF over snow, at CUES, using the bulk-aerodynamic method for water year 2017 – May 2021.

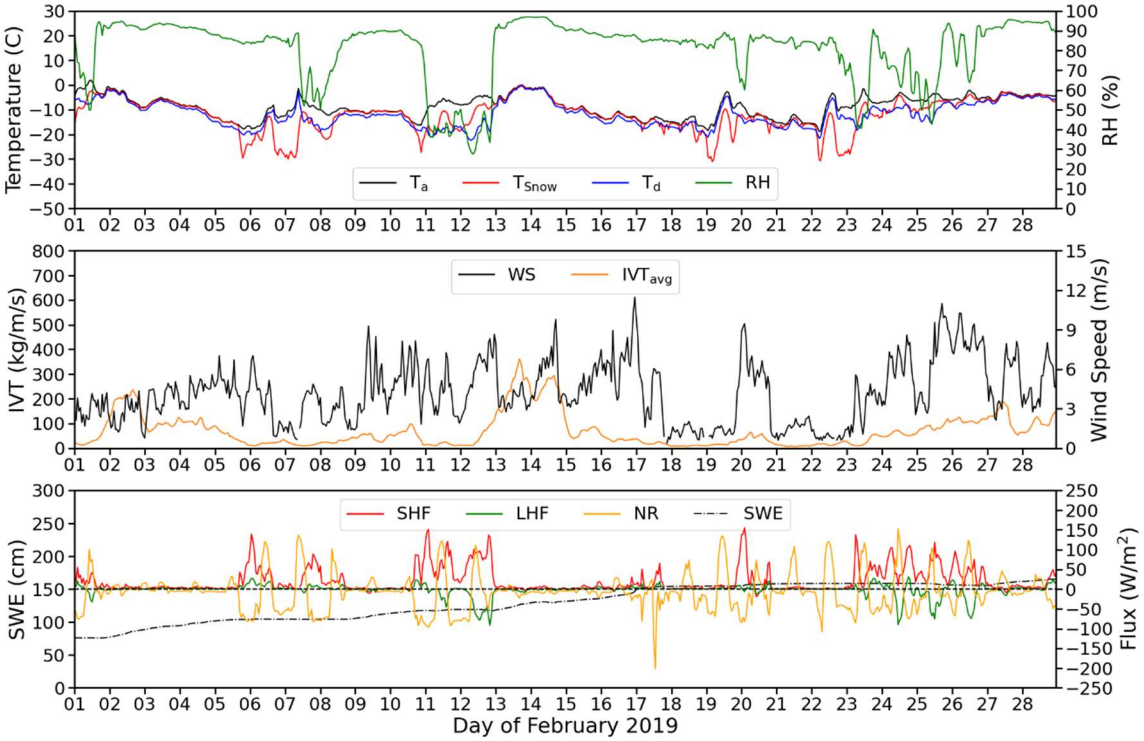

Figure 12: Hourly time series plot of data from CUES and turbulent heat fluxes estimated from the bulk-aerodynamic method during February 2019.

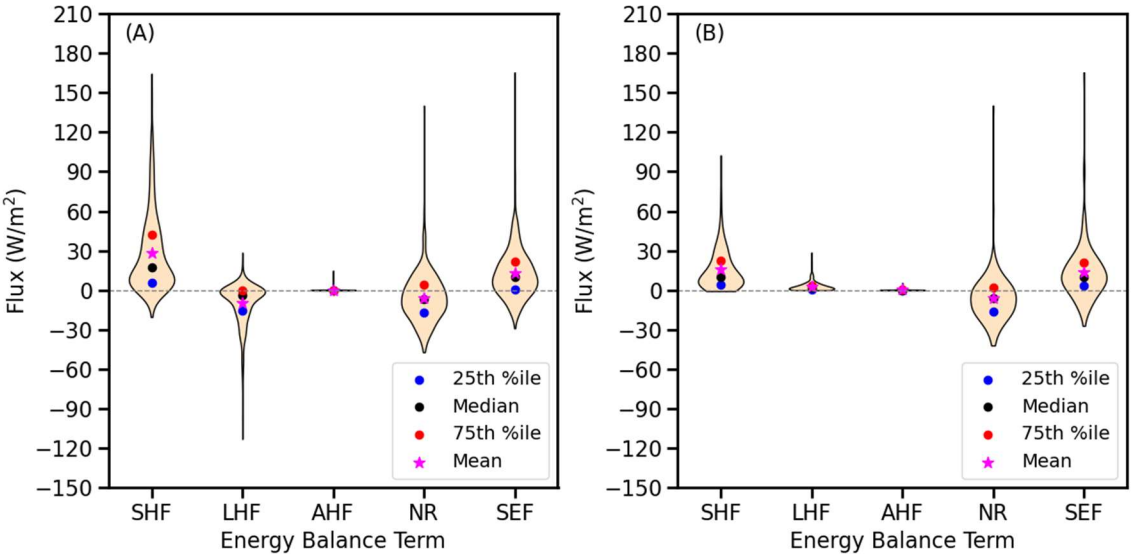

Figure 13: Violin distribution plots of each surface energy balance term with (A) Daily mean CUES data over snow and (B) Daily mean CUES data over snow when LHF is downward. Turbulent heat fluxes were estimated using the bulk-aerodynamic method.

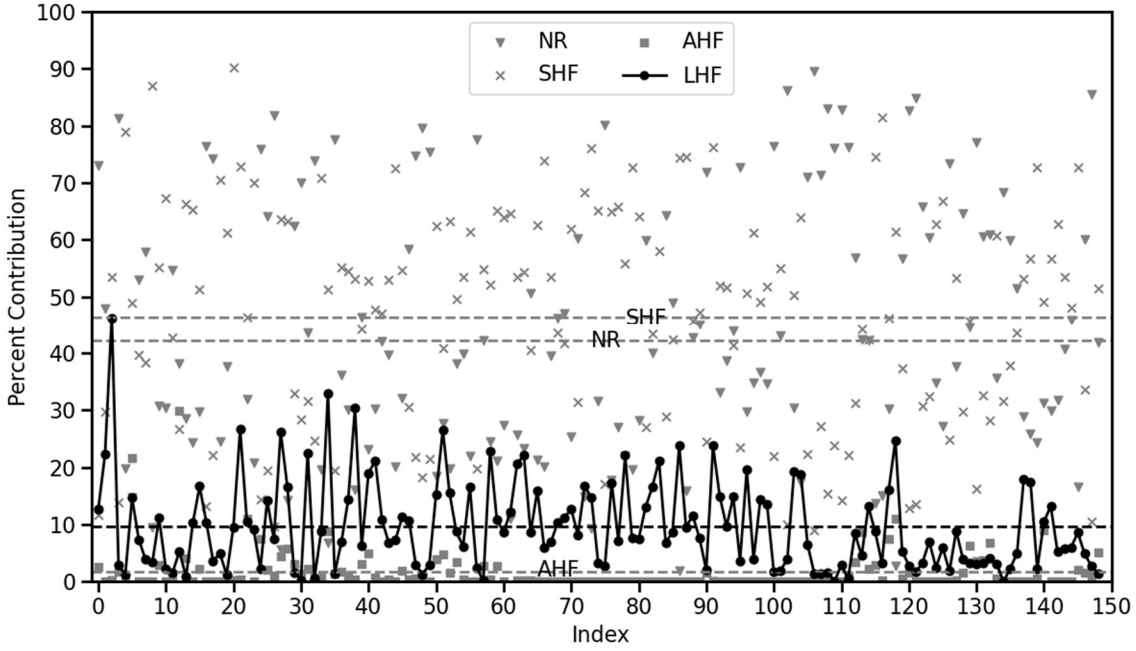

Figure 14: Percent contribution of each SEF term on each day with daily mean DLHF, with snow. Turbulent heat fluxes were estimated using the bulk-aerodynamic method

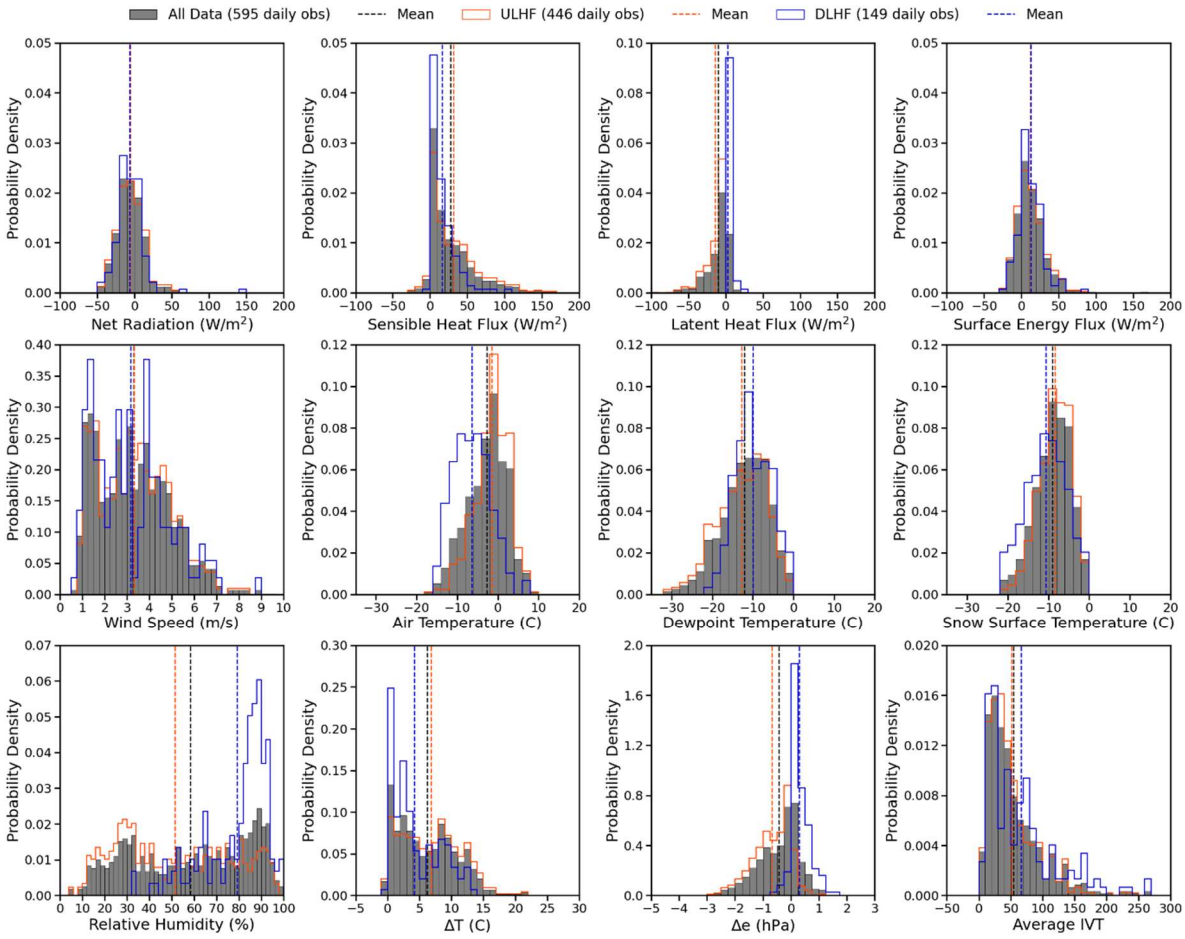

Figure 15: Daily mean probability density functions of various meteorological variables gathered from or calculated at CUES, when snow is present. Turbulent heat fluxes were estimated using the bulk-aerodynamic method. Grey bars represent the probability density function using all data. The orange and blue outlines represent the probability density function when LHF is upward and downward, respectively. The mean is shown as the vertical dashed line of the same color.

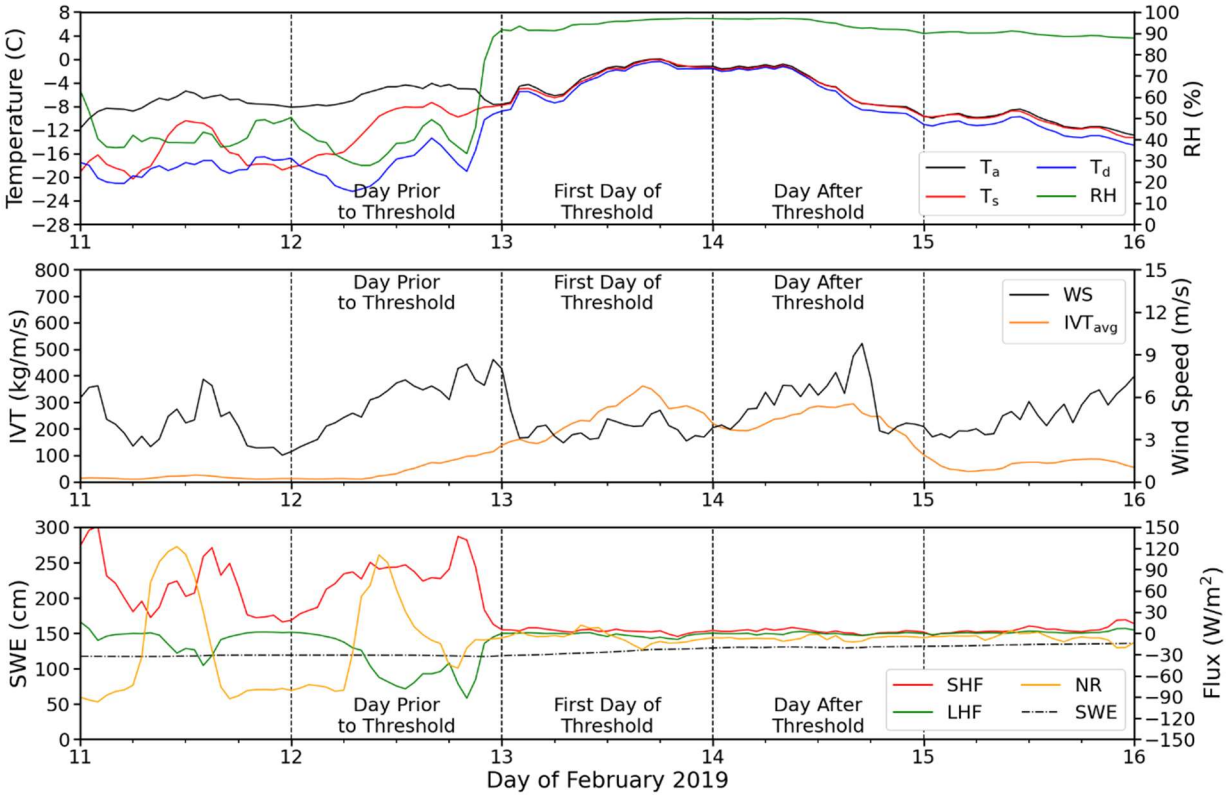

Figure 16: Hourly time series plot of data from CUES and estimated turbulent heat fluxes using the bulk-aerodynamic method from 11 February 2019 through 16 February 2019. Vertical dashed lines represent the beginning or end of the prior day, day of, or day after a given threshold is met.

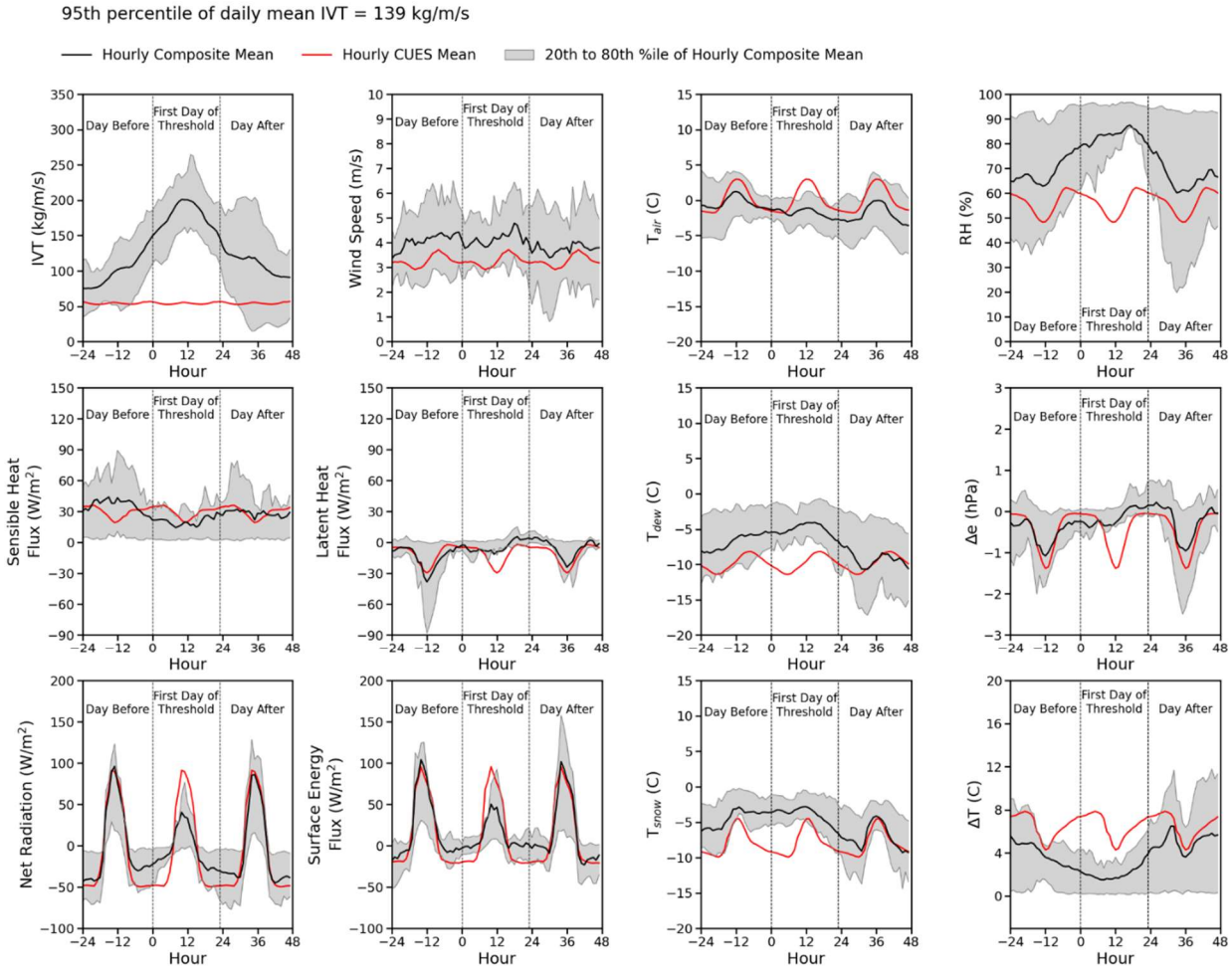

Figure 17: Hourly composite plots when daily mean integrated vapor transport exceeded the 95th percentile, with snow present. Turbulent heat fluxes were estimated using the bulk-aerodynamic method.

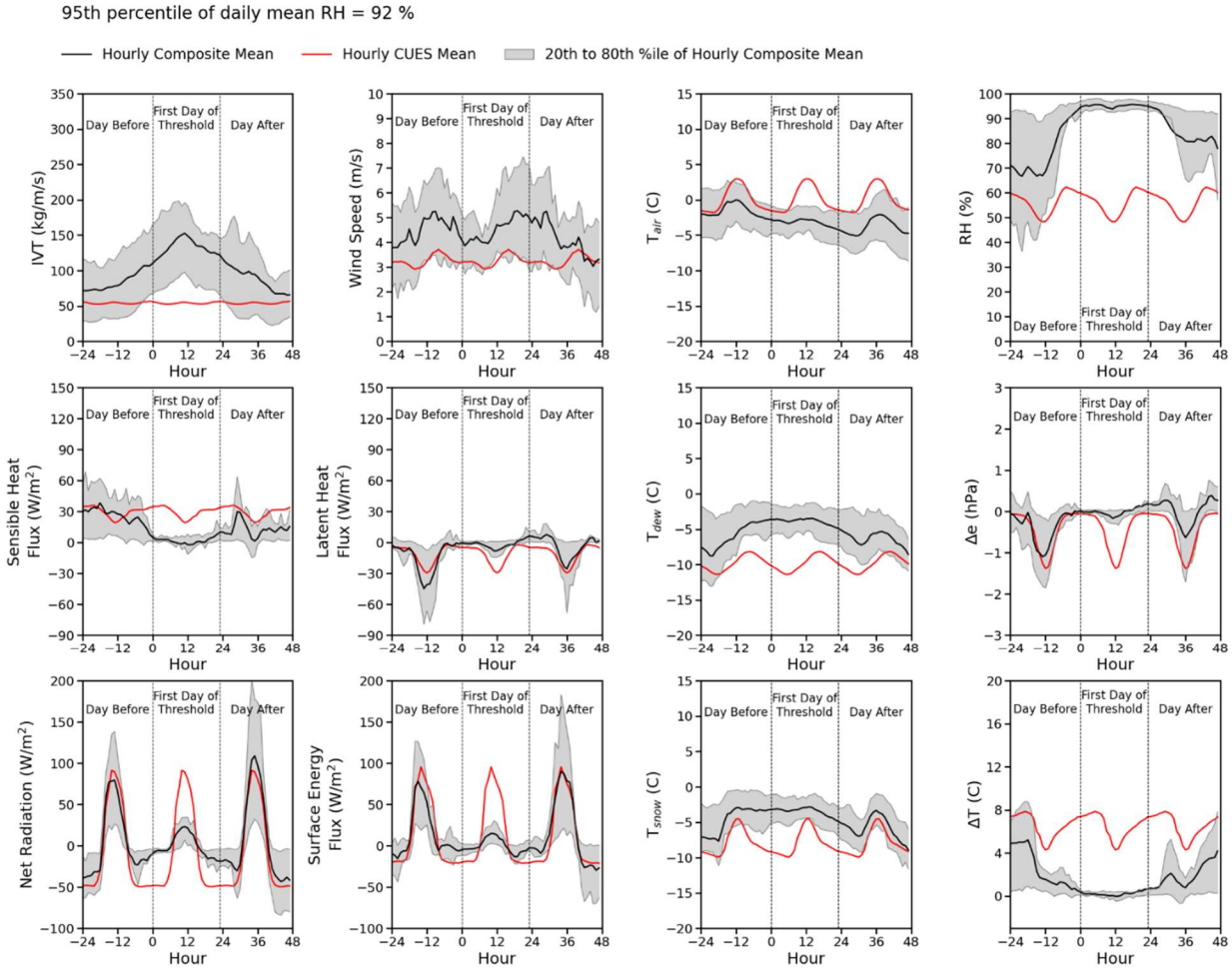

Figure 18: Same as Figure 17 but when relative humidity exceeded the 95th percentile.

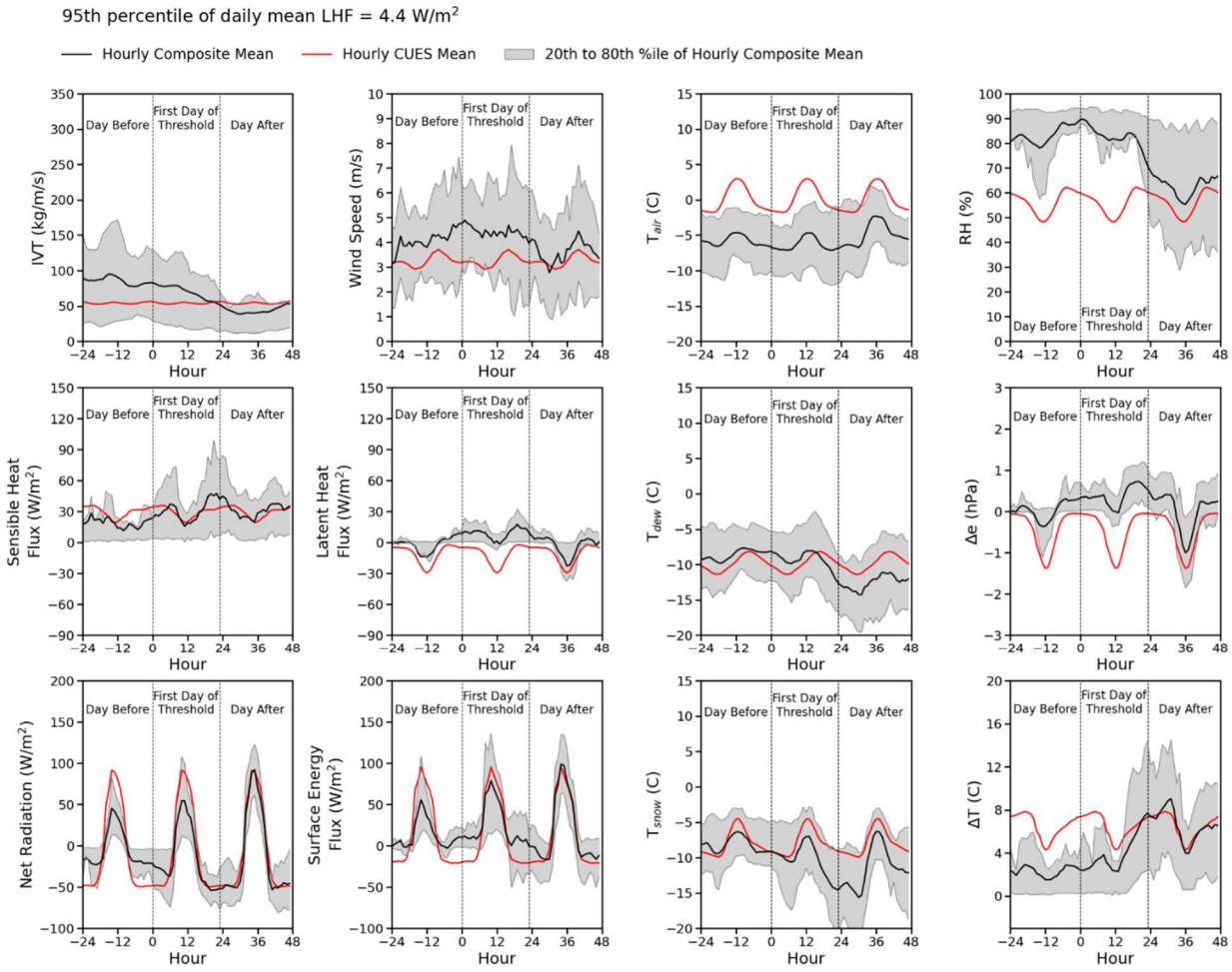

Figure 19: Same as Figure 17 but when latent heat flux exceeded the 95th percentile.

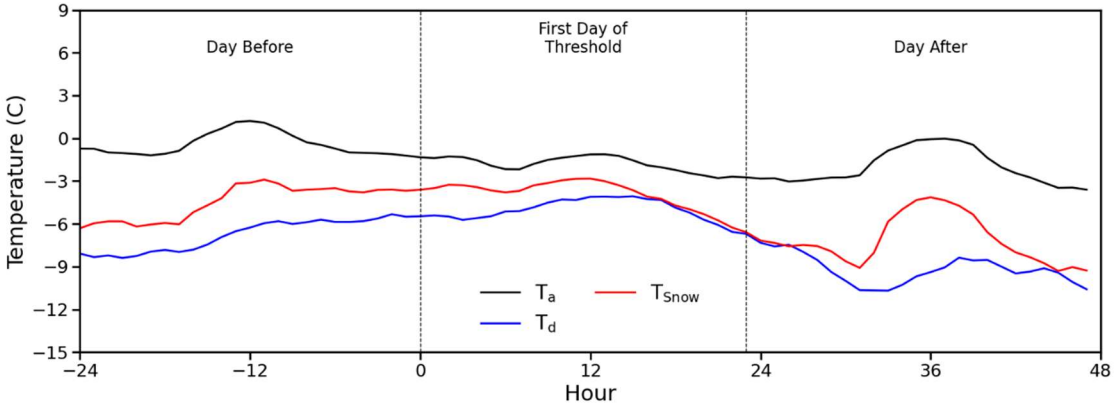

Figure 20: Combined hourly temperature composite plots from Figure 17.

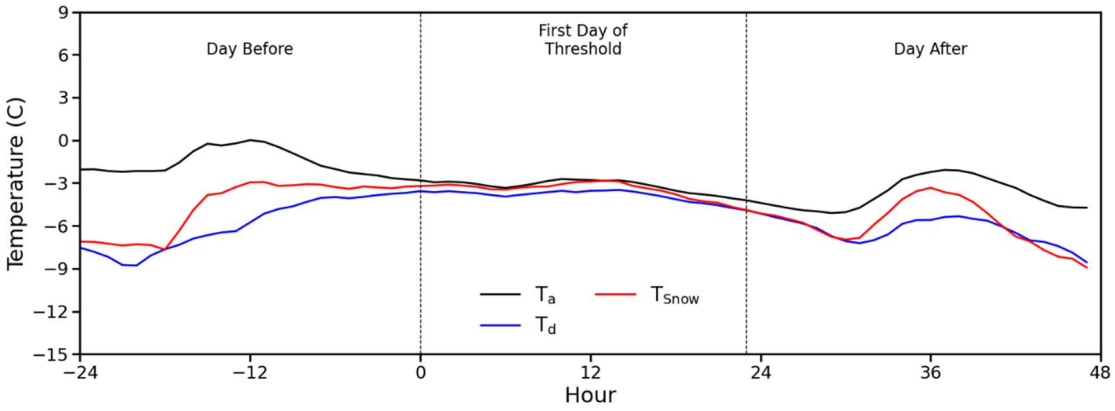

Figure 21: Combined hourly temperature composite plots from Figure 18.

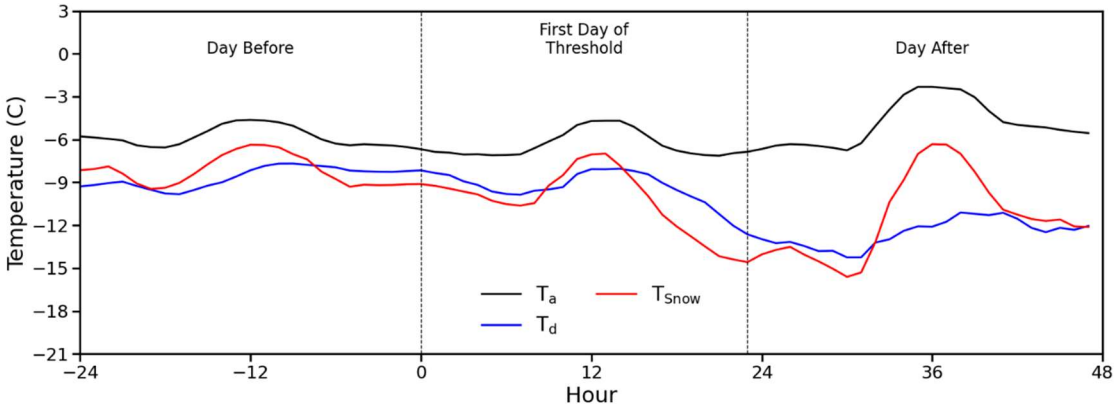

Figure 22: Combined hourly temperature composite plots from Figure 19.

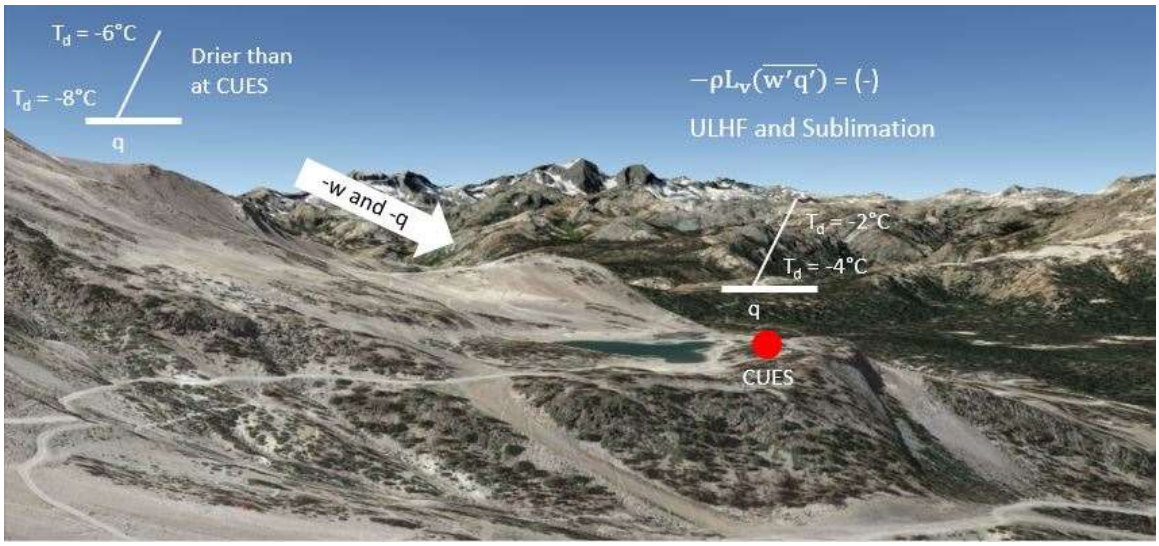

Figure 23: Schematic of how the eddy covariance method may be measuring countergradient fluxes at CUES.

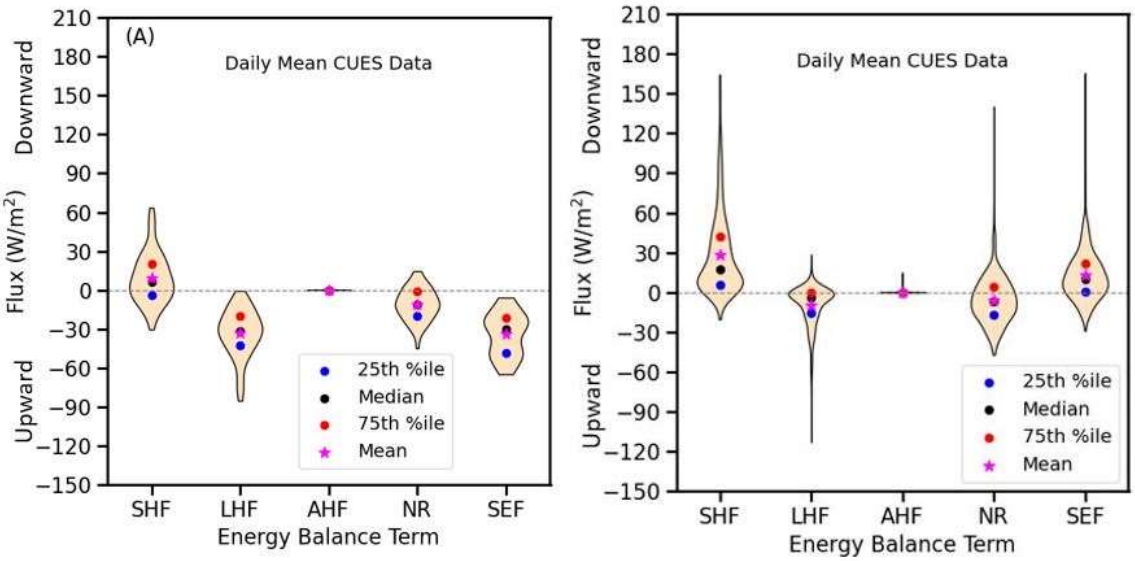

Figure 24: Violin distribution plots of each surface energy balance term with (A) Daily mean CUES data over snow. Turbulent heat fluxes were calculated using the eddy covariance method. (B) Same as Figure 12A.

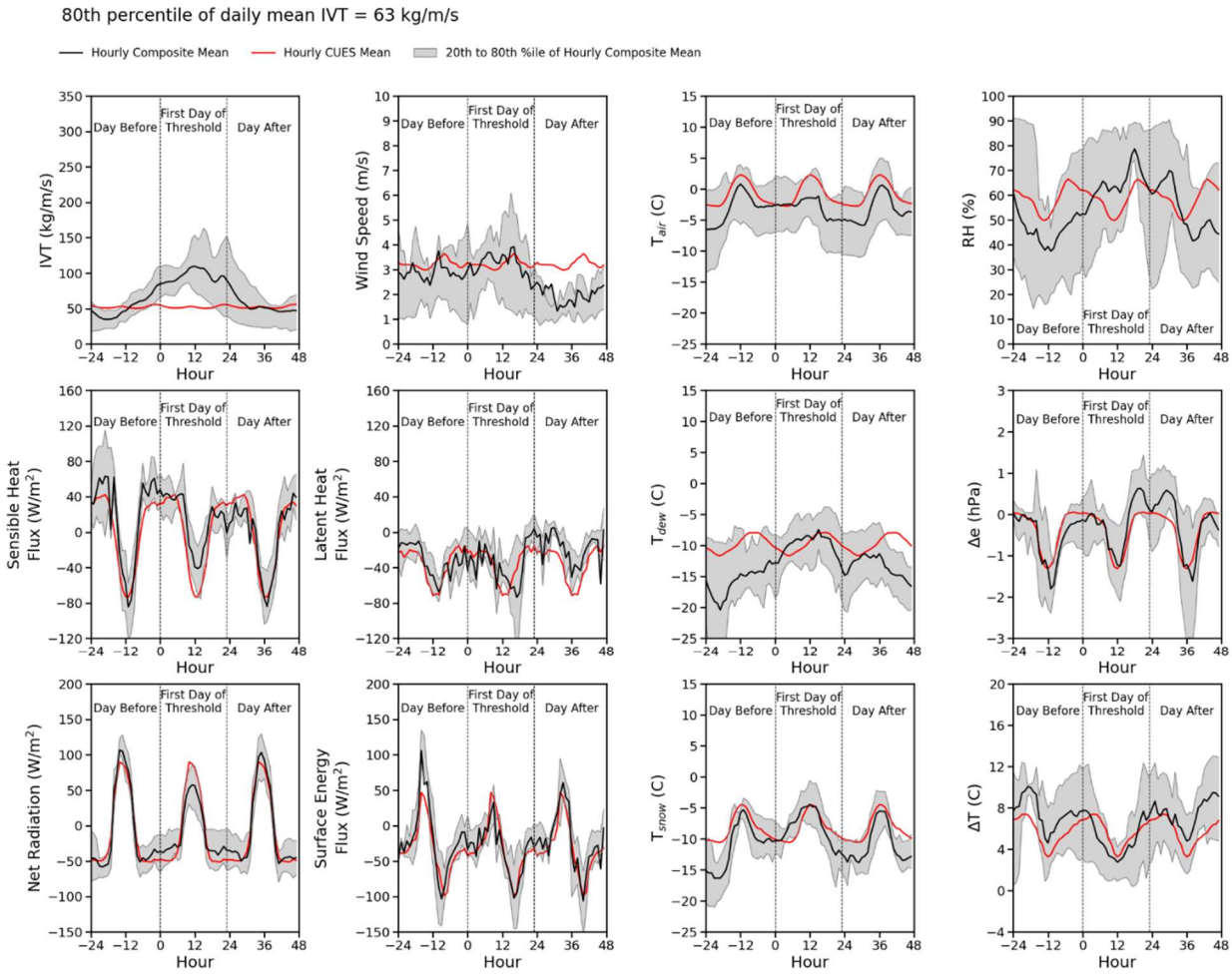

Figure 25: Hourly composite plots when daily mean integrated vapor transport exceeded the 80th percentile, with snow present. Turbulent heat fluxes were calculated using the eddy covariance method.

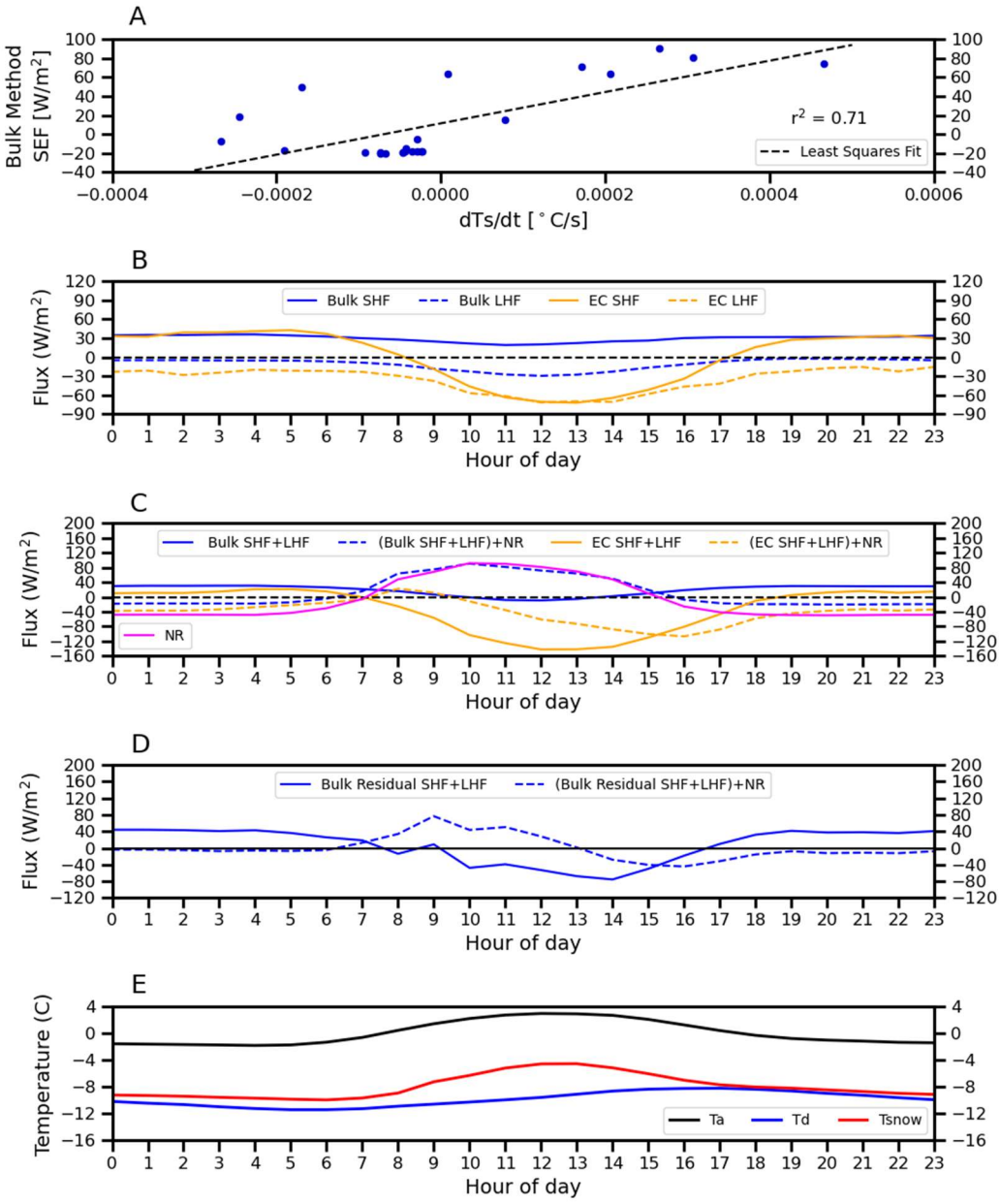

Figure 26: Comparison between hourly composite turbulent heat fluxes estimated from the bulk-aerodynamic method and calculated from the eddy covariance method. (A) Least squares fit between $\frac{dT_s}{dt}$ and total surface energy flux. (B) Turbulent heat flux comparisons. (C) Combined turbulent heat flux comparisons with net radiation added. (D) Residual combined turbulent heat fluxes after subtracting net radiation from the estimated surface energy flux using equation 21. The dashed blue line represents the estimated surface energy flux needed to achieve the snow surface temperature change in (E).

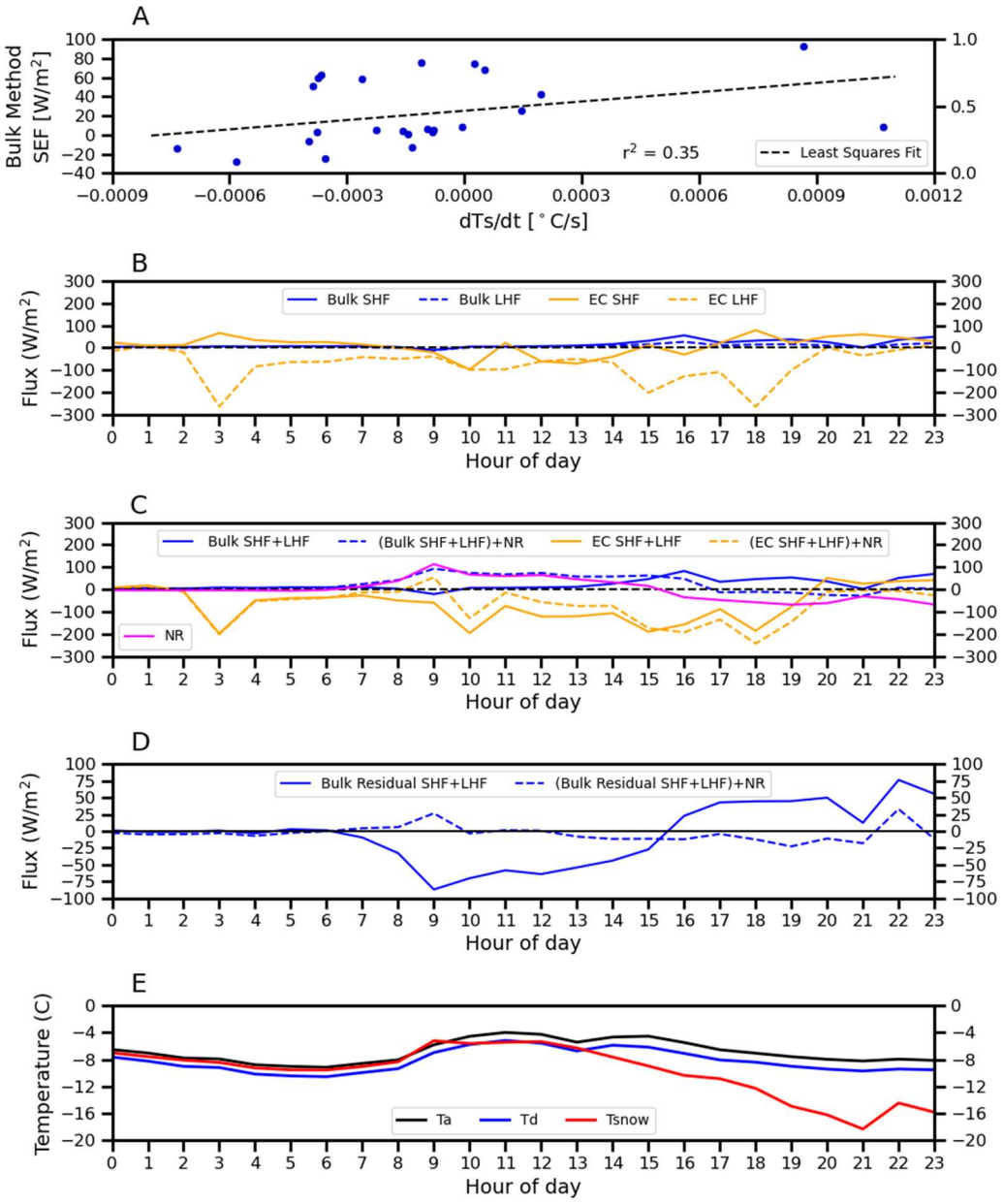

Figure 27: Same as Figure 26 but for 6 April 2020.

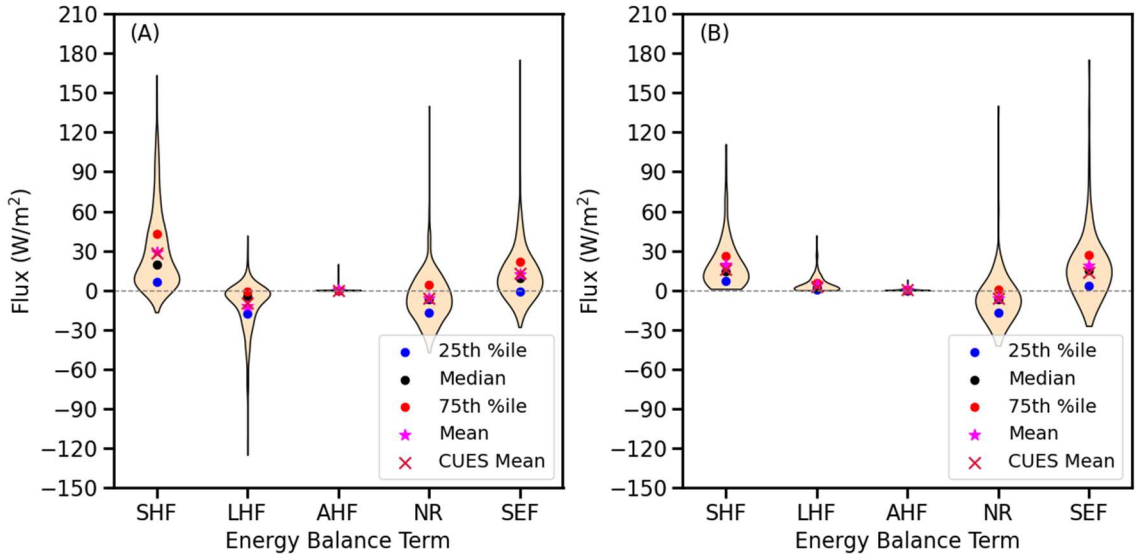

Figure 28: Same as Figure 13 but after the air and snow surface temperatures were raised by 2.5° C.

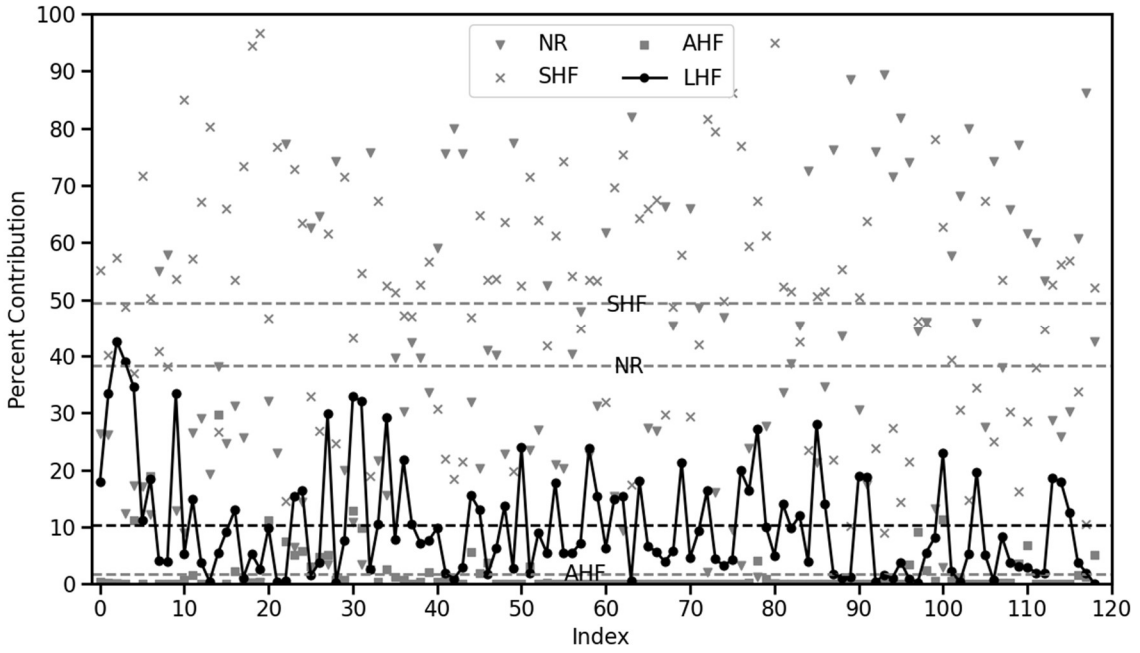

Figure 29: Same as Figure 14 but after the air and snow surface temperatures were raised by 2.5° C.

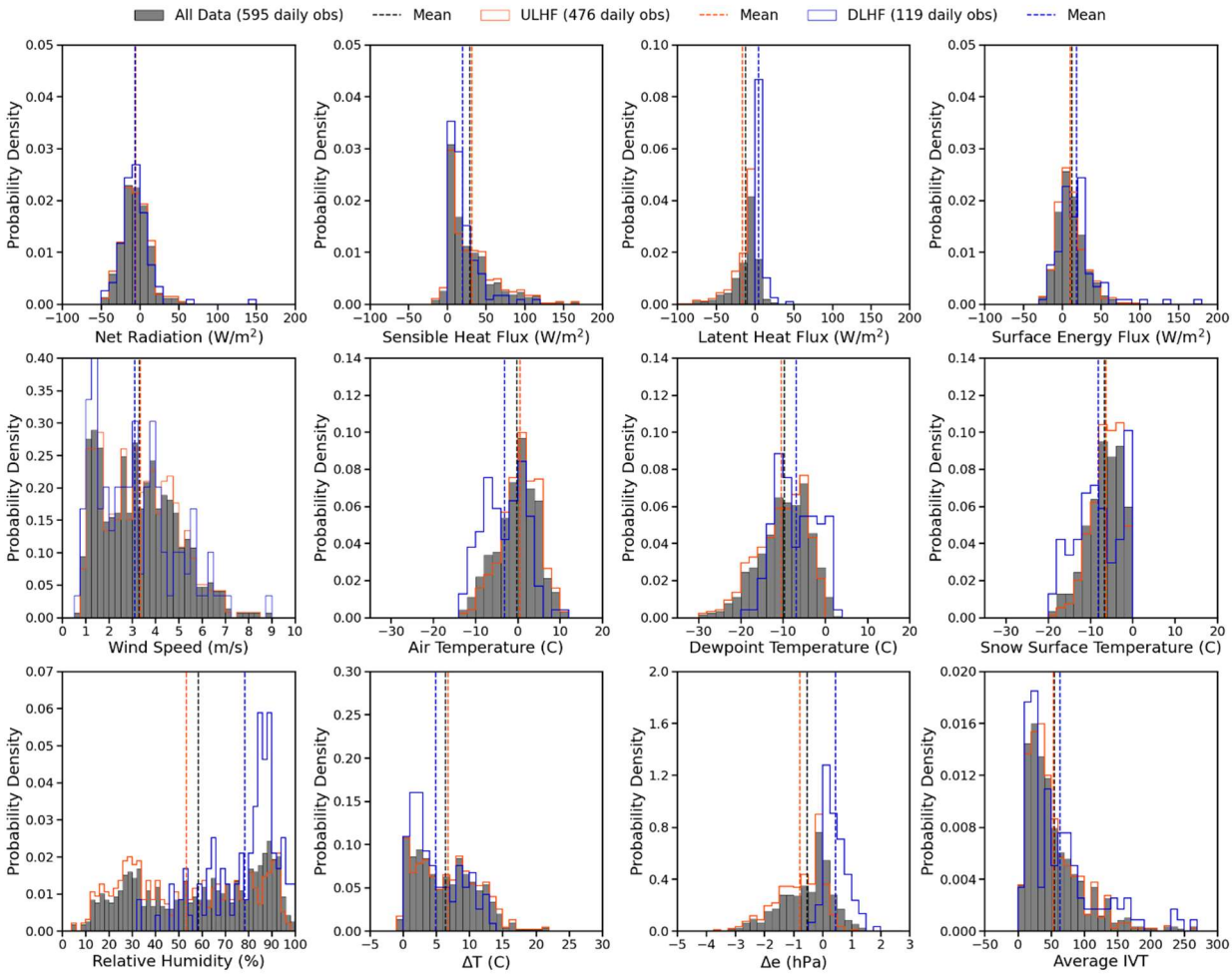

Figure 30: Same as Figure 15 but after the air and snow surface temperatures were raised by 2.5° C.

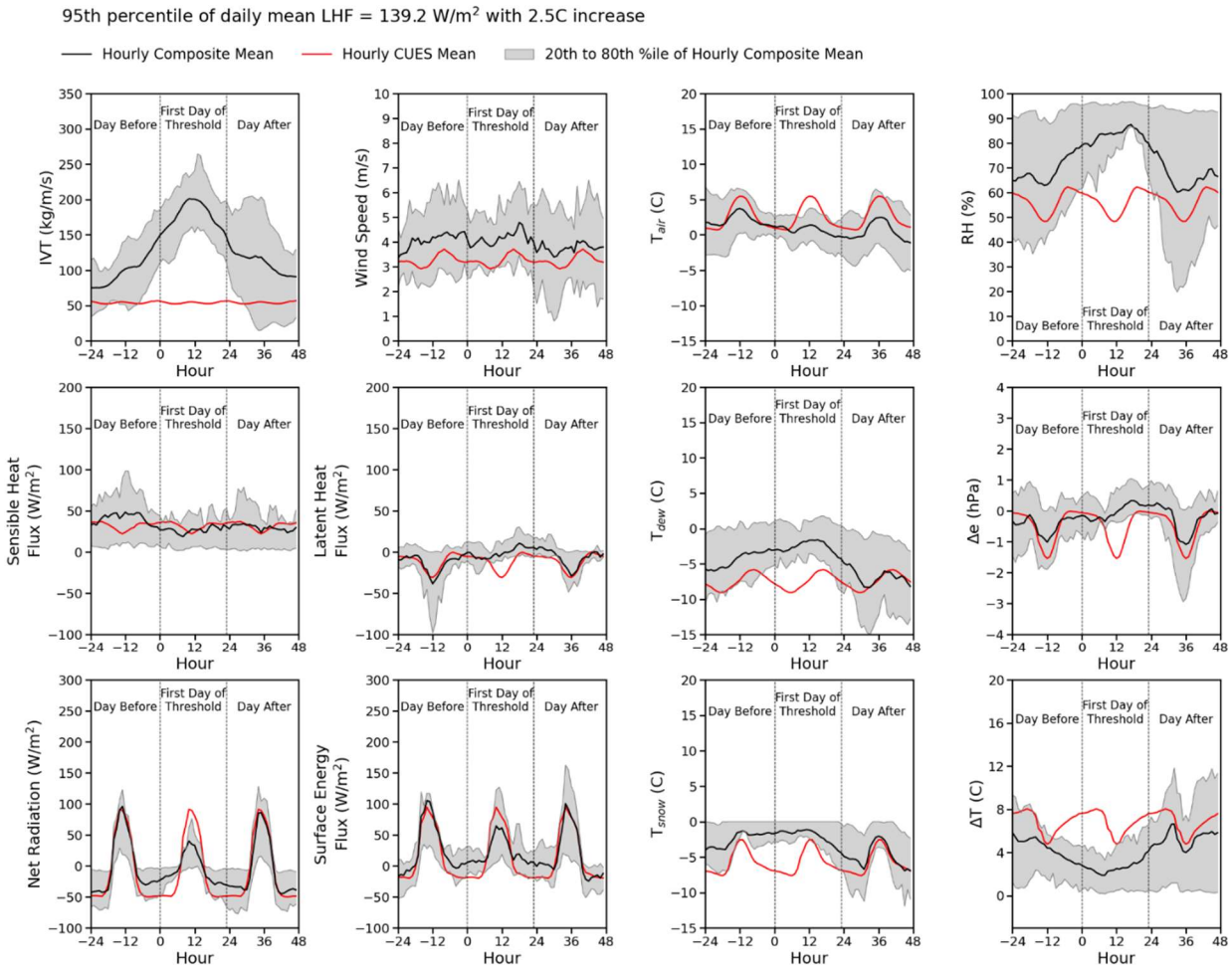

Figure 31: Hourly composite plots after the air and snow surface temperatures were raised by 2.5° C when daily mean integrated vapor transport exceeded the 95th percentile, with snow present. Turbulent heat fluxes were estimated using the bulk-aerodynamic method.

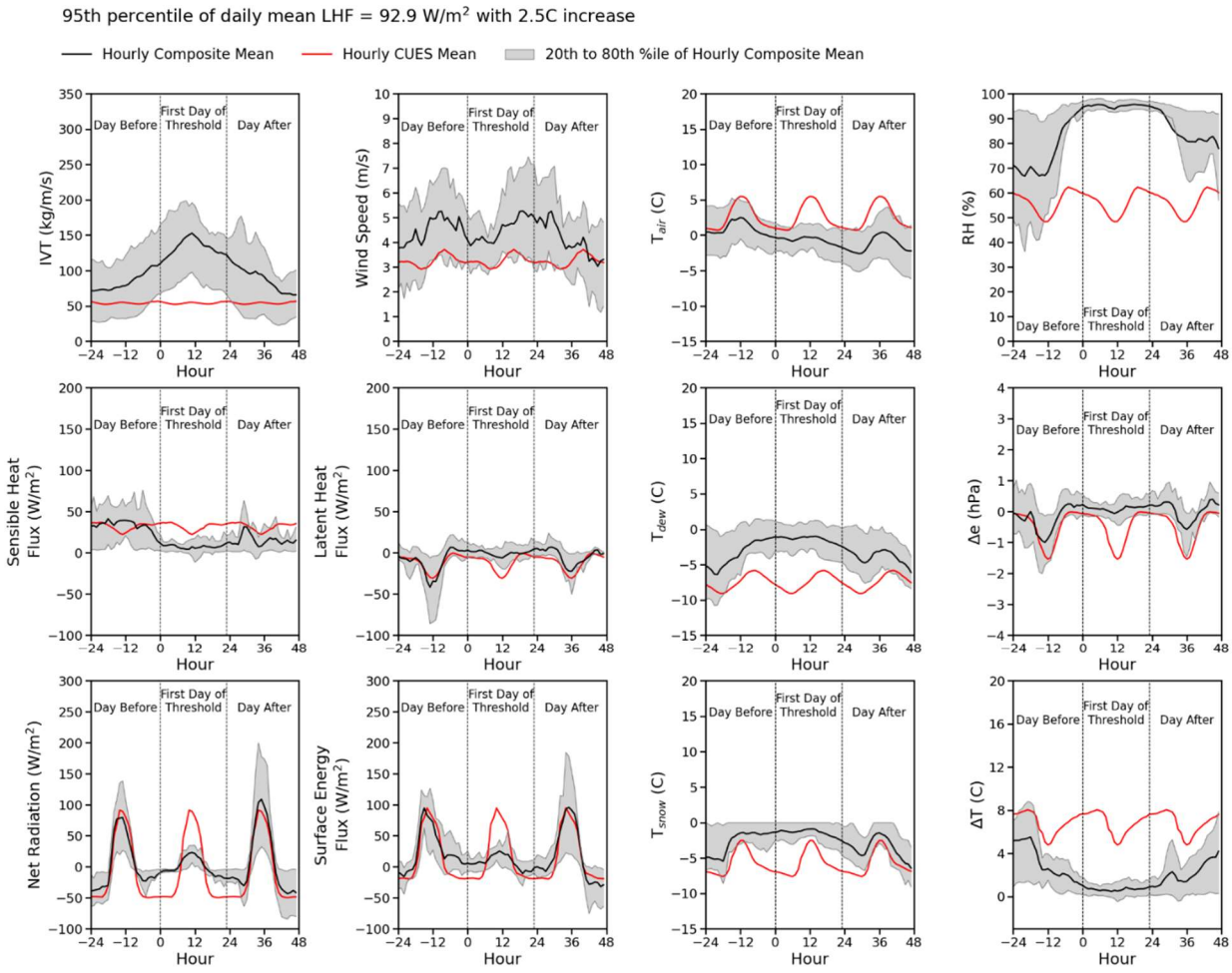

Figure 32: Same as Figure 31 but when relative humidity exceeded the 95th percentile.

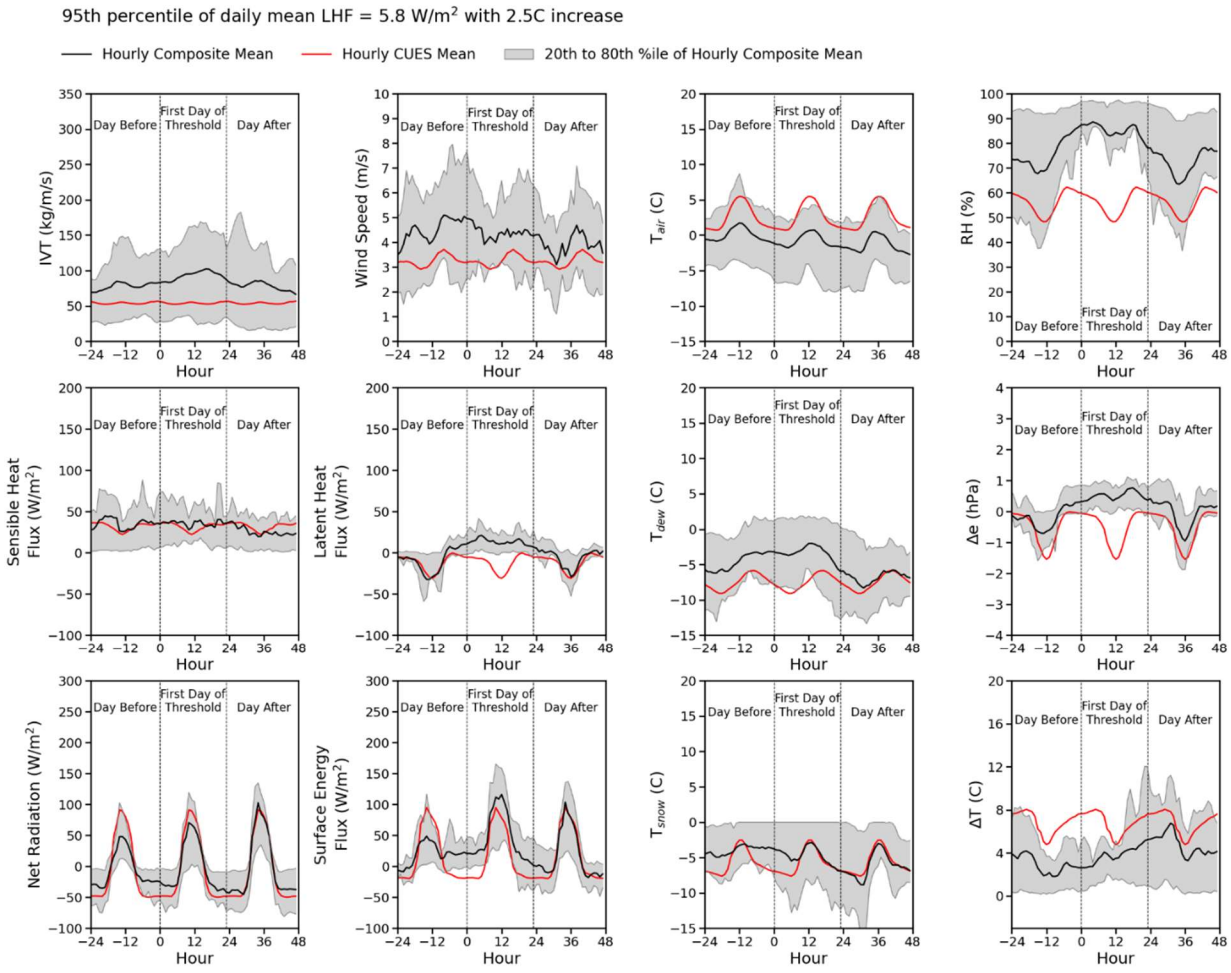

Figure 33: Same as Figure 31 but when latent heat flux exceeded the 95th percentile.

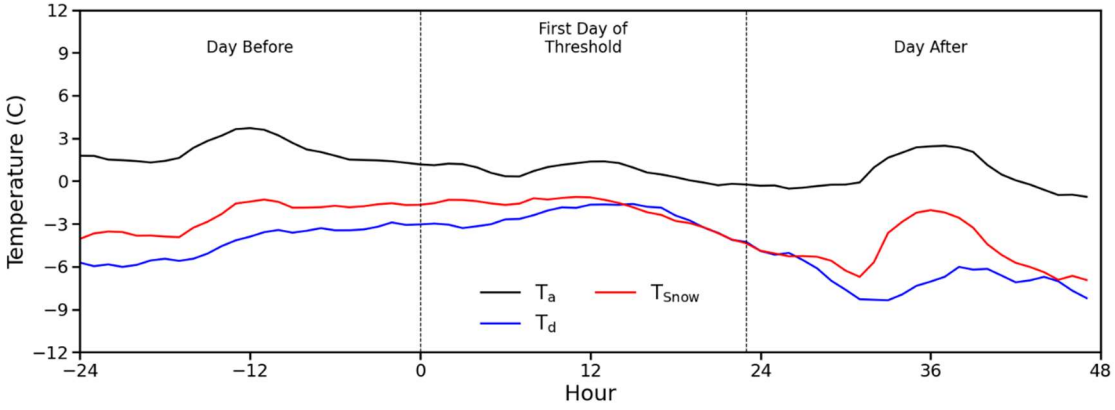

Figure 34: Combined hourly temperature composite plots from Figure 31.

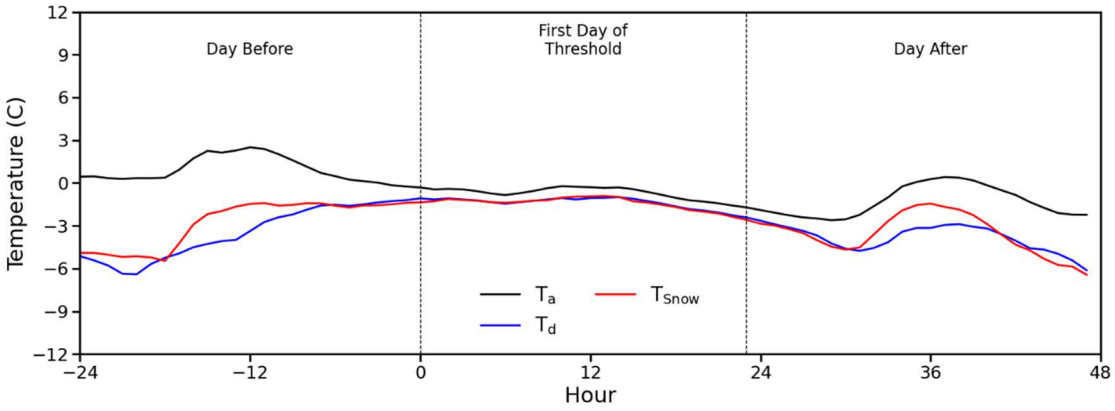

Figure 35: Combined hourly temperature composite plots from Figure 32.

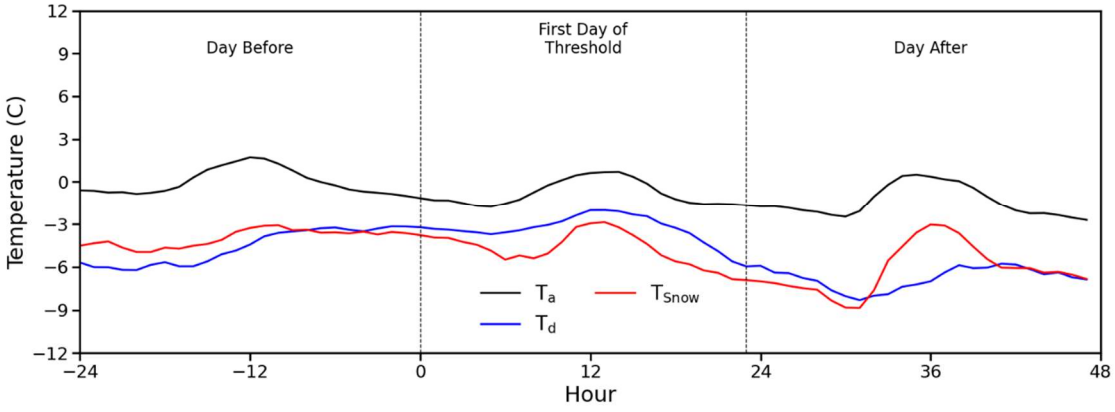

Figure 36: Combined hourly temperature composite plots from Figure 33.

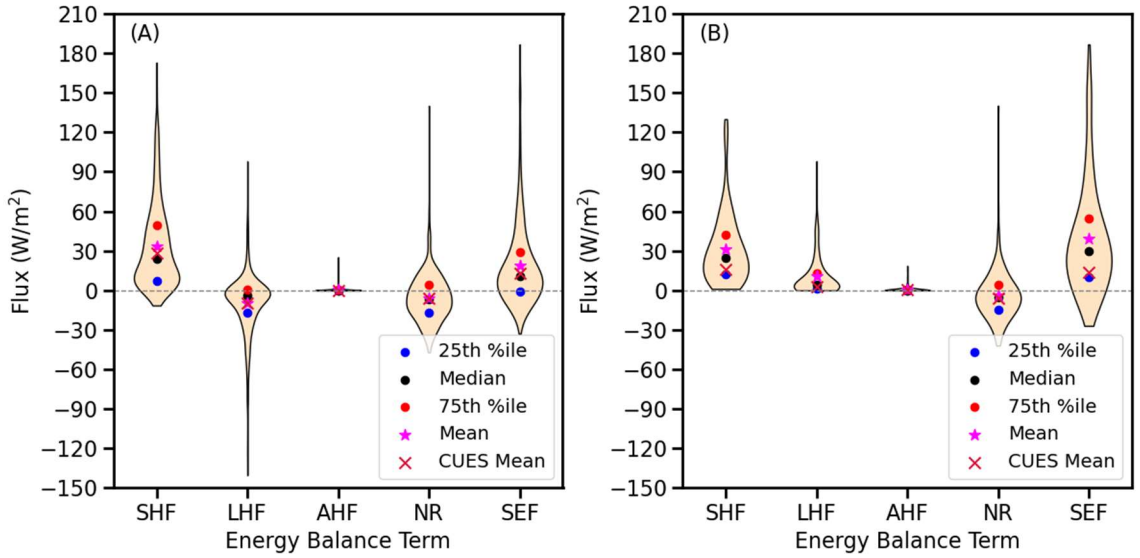

Figure 37: Same as Figure 13 but after the air and snow surface temperatures were raised by 5° C.

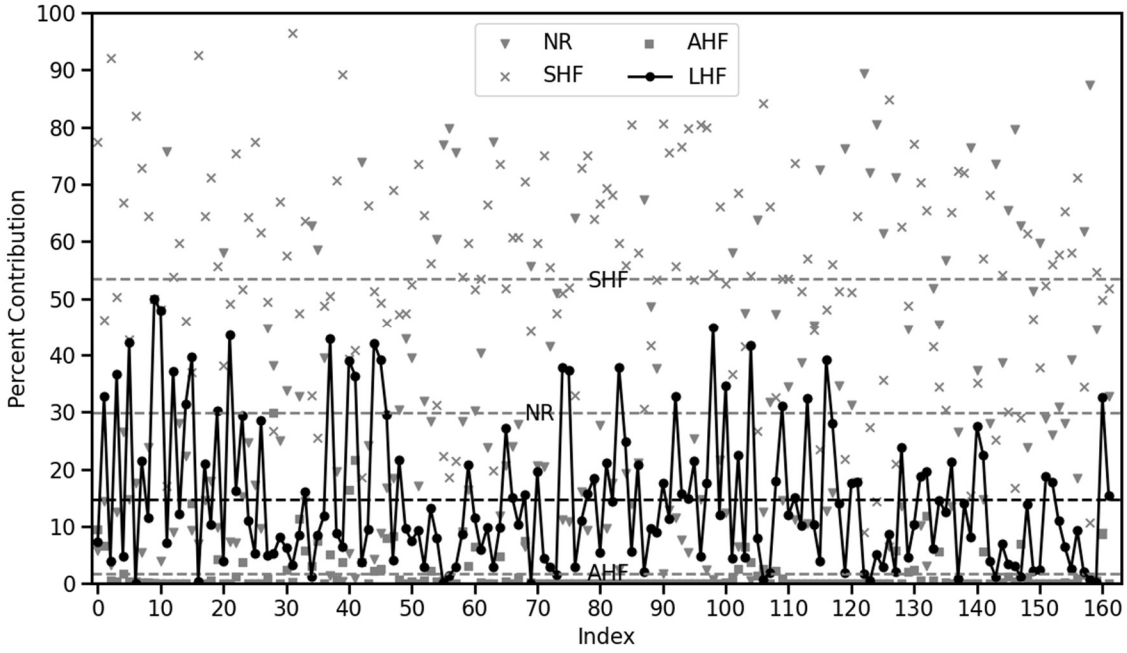

Figure 38: Same as Figure 14 but after the air and snow surface temperatures were raised by 5° C.

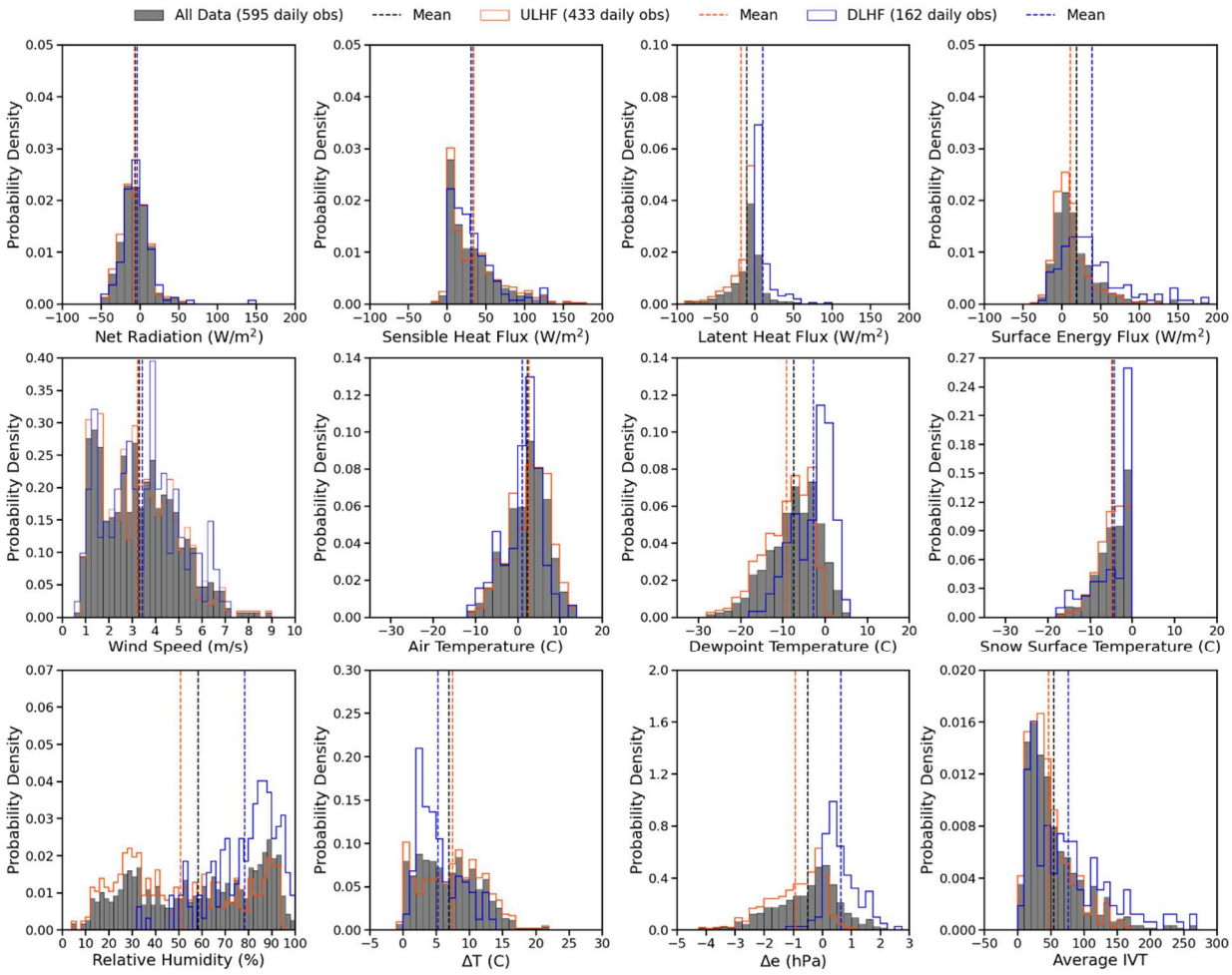

Figure 39: Same as Figure 15 but after the air and snow surface temperatures were raised by 5° C.

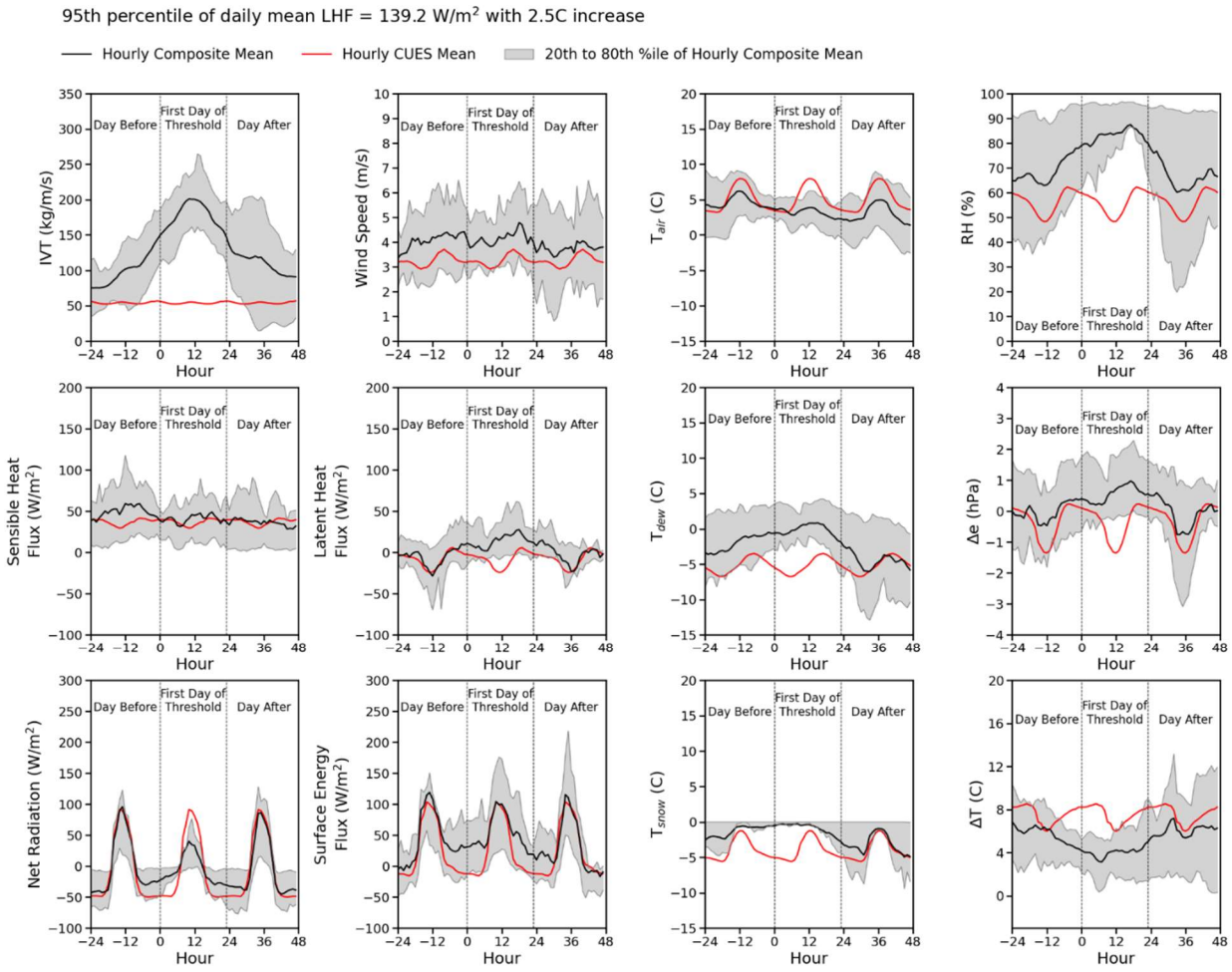

Figure 40: Hourly composite plots after the air and snow surface temperatures were raised by 5° C when daily mean integrated vapor transport exceeded the 95th percentile, with snow present. Turbulent heat fluxes were estimated using the bulk-aerodynamic method.

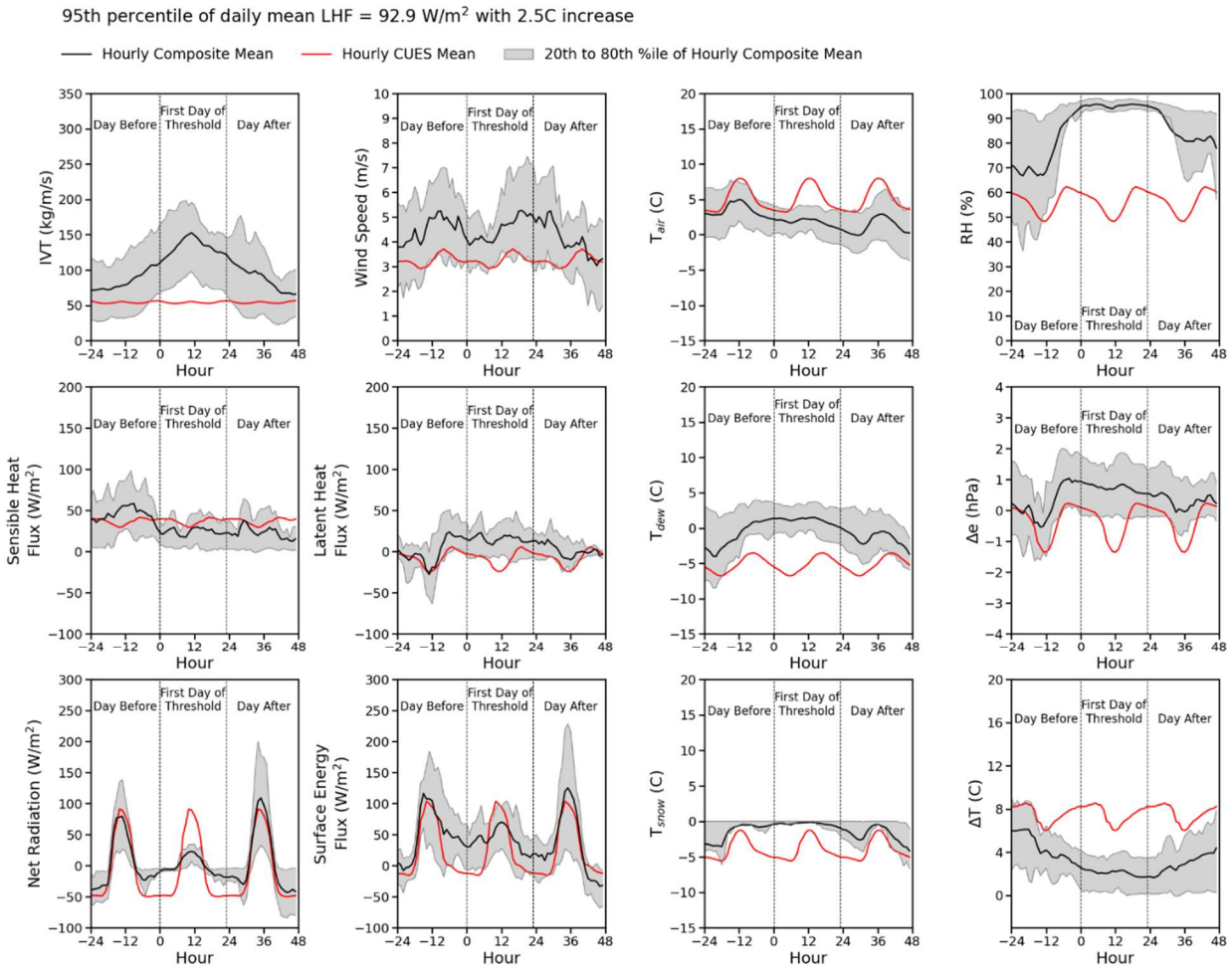

Figure 41: Same as Figure 40 but when relative humidity exceeded the 95th percentile.

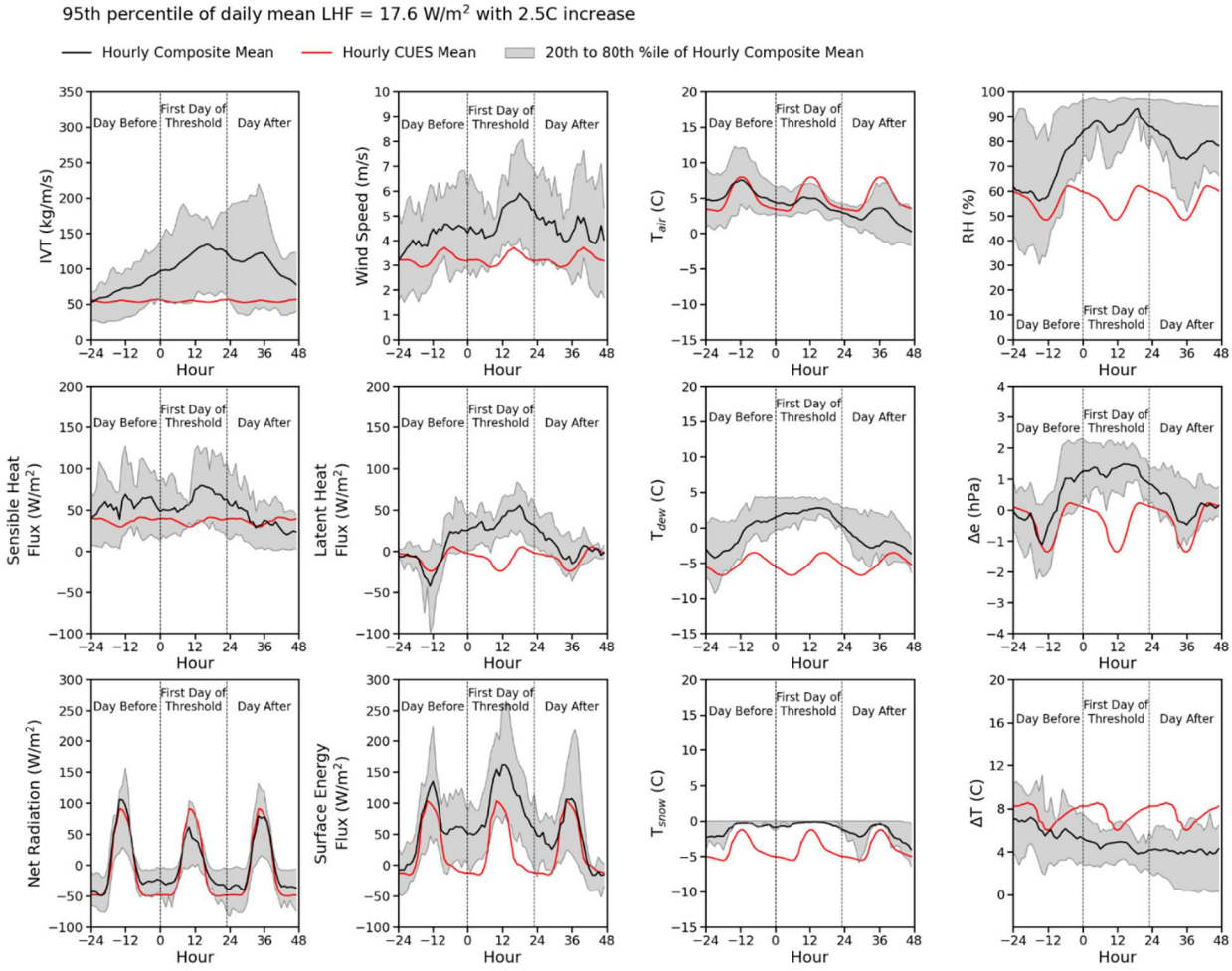

Figure 42: Same as Figure 41 but when latent heat flux exceeded the 95th percentile.

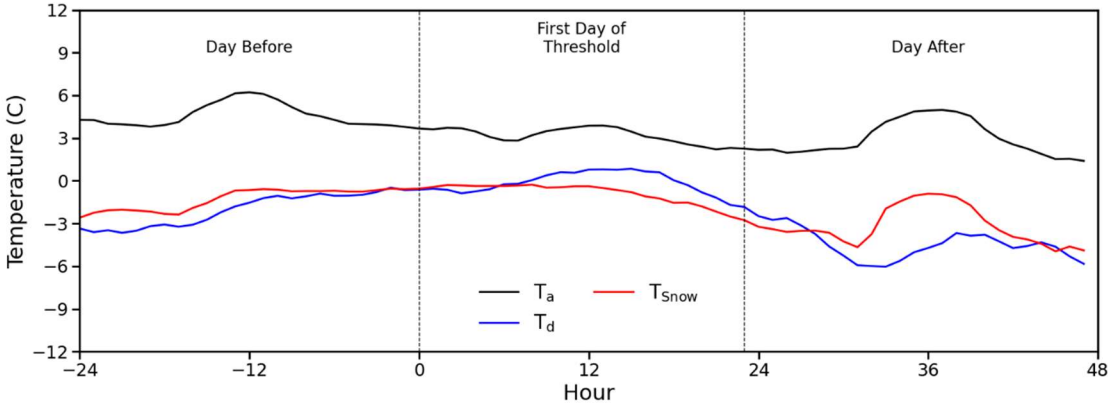

Figure 43: Same as Figure 19 but after the air and snow surface temperatures were raised by 5° C.

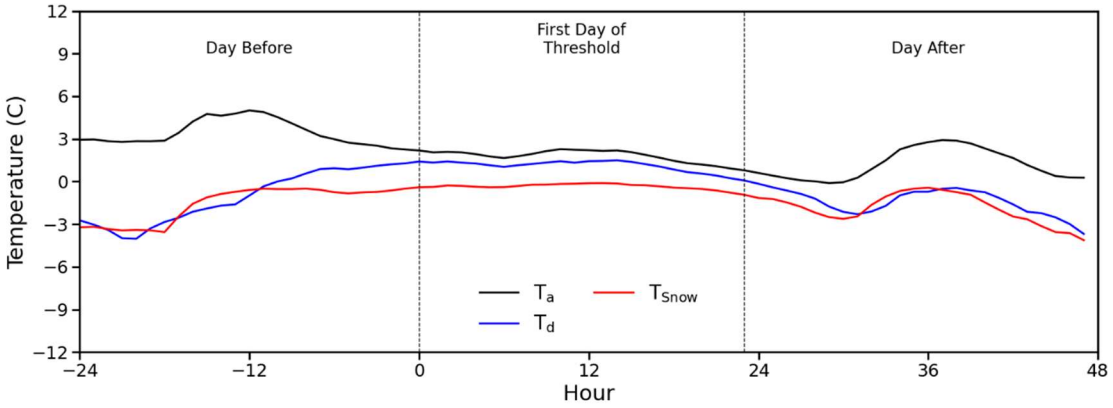

Figure 44: Same as Figure 20 but after the air and snow surface temperatures were raised by 5° C.

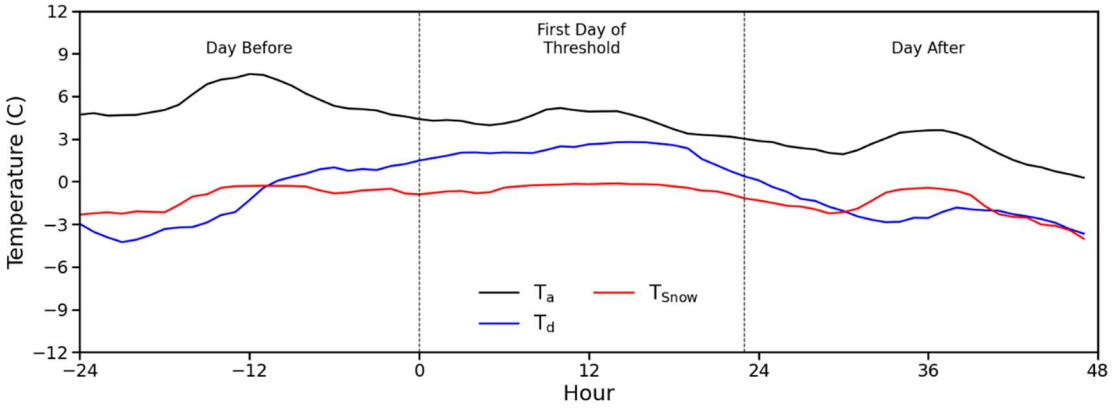

Figure 45: Same as Figure 21 but after the air and snow surface temperatures were raised by 5° C.

References

Bair, E. H., Dozier, J., Davis, R. E., Colee, M. T., & Claffey, K. J. (2015): CUES—A study site for measuring snowpack energy balance in the Sierra Nevada. *Frontiers in Earth Science*, 3, 58. doi:10.3389/feart.2015.00058.

Bales, R. C., Molotch, N. P., Painter, T. H., Dettinger, M. D., Rice, R., & Dozier, J. (2006): Mountain hydrology of the western United States. *Water Resources Research*, 42(8). doi:10.1029/2005WR004387.

Baldocchi, D. D., Hincks, B. B., & Meyers, T. P. (1988): Measuring biosphere-atmosphere exchanges of biologically related gases with micrometeorological methods. *Ecology*, 69(5), 1331-1340. doi.org/10.2307/1941631

Born, A., Imhof, M. A., & Stocker, T. F. (2019): An efficient surface energy–mass balance model for snow and ice. *The Cryosphere*, 13(5), 1529-1546. doi.org/10.5194/tc-13-1529-2019

Brock, B. W., Willis, I. C., & Sharp, M. J. (2006): Measurement and parameterization of aerodynamic roughness length variations at Haut Glacier d'Arolla, Switzerland. *Journal of Glaciology*, 52(177), 281-297. doi.org/10.3189/172756506781828746

Cayan, D. R. (1996): Interannual climate variability and snowpack in the western United States. *Journal of Climate*, 9(5), 928-948. doi.org/10.1175/1520-0477(2001)082<0399:CITOOS>2.3.CO;2

Curry, J. A., & Webster, P. J. (1998): Thermodynamics of atmospheres and oceans. Elsevier.

Dettinger M.D., Ralph F.M., Das T, Neiman P.J., Cayan D.R (2011): Atmospheric rivers, floods, and the water resources of California. *Water*. 3(2):445-478. doi.org/10.3390/w3020445

Dozier, J., & Warren, S. G. (1982): Effect of viewing angle on the infrared brightness temperature of snow. *Water Resources Research*, 18(5), 1424-1434. doi.org/10.1029/WR018i005p01424

Garvelmann, J., Pohl, S., & Weiler, M. (2014): Variability of observed energy fluxes during rain-on-snow and clear sky snowmelt in a midlatitude mountain environment. *Journal of Hydrometeorology*, 15(3), 1220-1237. doi.org/10.1175/JHM-D-13-0187.1

Goulden, M. L., Anderson, R. G., Bales, R. C., Kelly, A. E., Meadows, M., & Winston, G. C. (2012): Evapotranspiration along an elevation gradient in California's Sierra Nevada. *Journal of Geophysical Research: Biogeosciences*, 117(G3). https://doi.org/10.1029/2012JG002027

Guan, B., D. E. Waliser, F. M. Ralph, E. J. Fetzer, and P. J. Neiman (2016): Hydrometeorological characteristics of rain-on-snow events associated with atmospheric rivers, *Geophysical Research Letters*, 43, 2964–2973, doi:10.1002/2016GL067978.

Henn, B., Musselman, K. N., Lestak, L., Ralph, F. M., & Molotch, N. P. (2020): Extreme runoff generation from atmospheric river driven snowmelt during the 2017 Oroville dam spillways incident. *Geophysical Research Letters*, 47, e2020GL088189. doi.org/10.1029/2020GL088189

Heron, R. and Woo, M. (1978): Snowmelt computations for a high arctic site. Proc. 35th Eastern Snow Conf., Hanover, NH, Eastern Snow Conference, 162–172.

Hersbach, H., Bell, B., Berrisford, P., Biavati, G., Horányi, A., Muñoz Sabater, J., Nicolas, J., Peubey, C., Radu, R., Rozum, I., Schepers, D., Simmons, A., Soci, C., Dee, D., Thépaut, J-N. (2018): ERA5 hourly data on single levels from 1979 to present. Copernicus Climate Change Service (C3S) Climate Data Store (CDS). (Accessed on 22-Mar-2021 and 24-Jun-2021), 10.24381/cds.adbb2d47

Huang, J. (2018): A simple accurate formula for calculating saturation vapor pressure of water and ice. *Journal of Applied Meteorology and Climatology*, 57(6), 1265-1272. doi.org/10.1175/JAMC-D-17-0334.1

Jennings, K. S., Kittel, T. G., & Molotch, N. P. (2018): Observations and simulations of the seasonal evolution of snowpack cold content and its relation to snowmelt and the snowpack energy budget. *The Cryosphere*, 12(5), 1595-1614. doi.org/10.5194/tc-12-1595-2018

Jennings, K. S., and J. A. Jones (2015): Precipitation-snowmelt timing and snowmelt augmentation of large peak flow events, western Cascades, Oregon, *Water Resour. Res*., 51, 7649–7661, doi:10.1002/2014WR016877.

Kattelmann, R. (1996): Flooding from rain-on-snow events in the Sierra Nevada. *In North American Water and Environment Congress & Destructive Water* (pp. 1145-1146). ASCE.

Kim, J., Waliser, D. E., Neiman, P. J., Guan, B., Ryoo, J., Wick, G. A., (2013): Effects of atmospheric river landfalls on the cold season precipitation in California. *Climate Dynamics* 40, 465–474. doi.org/10.1007/s00382-012-1322-3

Lapo, K., Nijssen, B., & Lundquist, J. D. (2019): Evaluation of turbulence stability schemes of land models for stable conditions. *Journal of Geophysical Research: Atmospheres*, 124(6), 3072-3089. doi.org/10.1029/2018JD028970

Li, D., Lettenmaier, D. P., Margulis, S. A., & Andreadis, K. (2019): The role of rain-on-snow in flooding over the conterminous United States. *Water Resources Research*, 55, 8492–8513. doi.org/10.1029/2019WR024950

Male, D. H., & Granger, R. J. (1981): Snow surface energy exchange. *Water Resources Research*, 17(3), 609-627. doi.org/10.1029/WR017i003p00609

Marks, D., & Dozier, J. (1992): Climate and energy exchange at the snow surface in the alpine region of the Sierra Nevada: 2. Snow cover energy balance. *Water Resources Research*, 28(11), 3043-3054. doi.org/10.1029/92WR01483

Marks, D., Kimball, J., Tingey, D. and Link, T. (1998): The sensitivity of snowmelt processes to climate conditions and forest cover during rain-on-snow: a case study of the 1996 Pacific Northwest flood. *Hydrol. Process*., 12: 1569-1587. doi.org/10.1002/(SICI)1099-1085(199808/09)12:10/11<1569::AID-HYP682>3.0.CO;2-L

Moore, R. D., & Owens, I. F. (1984): Controls on advective snowmelt in a maritime alpine basin. *Journal of Applied Meteorology and Climatology*, 23(1), 135-142. doi.org/10.1175/1520-0450(1984)023<0135:COASIA>2.0.CO;2

Neiman, P. J., Ralph, F. M., Wick, G. A., Lundquist, J. D., & Dettinger, M. D. (2008): Meteorological characteristics and overland precipitation impacts of atmospheric rivers affecting the west coast of North America based on eight years of SSM/I satellite observations, *Journal of Hydrometeorology*, 9(1), 22-47. doi.org/10.1175/2007JHM855.1

Prueger, J. H. and Kustas, W. P. (2005): Aerodynamic methods for estimating turbulent fluxes. Publications from USDA-ARS / UNL Faculty. 1394. https://digitalcommons.unl.edu/usdaarsfacpub/1394

Price, A. G., Dunne, T. & Colbeck, S. C. (1976): Energy balance and runoff from a subarctic snowpack. CRREL Report 76-27, Cold Regions Research and Engineering Laboratory, Hanover, NH, USA, 1-29. https://hdl.handle.net/11681/9527

Prowse, T. D., & Owens, I. F. (1982): Energy balance over melting snow, Craigieburn Range, New Zealand. *Journal of Hydrology* (New Zealand), 133-147.

Ralph, F. M., Neiman, P. J., & Wick, G. A. (2004): Satellite and CALJET aircraft observations of atmospheric rivers over the eastern North Pacific Ocean during the winter of 1997/98, *Monthly Weather Review*, 132(7), 1721-1745. doi.org/10.1175/1520-0493(2004)132<1721:SACAOO>2.0.CO;2

Ralph, F. M., Neiman P. J., Wick G. A., Gutman S. I., Dettinger M. D., Cayan D. R., and White A. B. (2006): Flooding on California's Russian River: role of atmospheric rivers. *Geophysical Research Letters*, 33, L13801, doi:10.1029/2006GL026689.

Reba, M. L., Marks, D., Link, T. E., Pomeroy, J., & Winstral, A. (2014): Sensitivity of model parameterizations for simulated latent heat flux at the snow surface for complex mountain sites. *Hydrological Processes*, 28(3), 868-881. doi.org/10.1002/hyp.9619

Rutz, J. J., Steenburgh, W. J., & Ralph, F. M. (2014): Climatological characteristics of atmospheric rivers and their inland penetration over the western United States, *Monthly Weather Review*, 142(2), 905-921. doi:10.1175/MWR-D-13-00168.

Sexstone, G. A., Clow, D. W., Stannard, D. I., & Fassnacht, S. R. (2016): Comparison of methods for quantifying surface sublimation over seasonally snow-covered terrain. *Hydrological Processes*, 30(19), 3373-3389. doi.org/10.1002/hyp.10864

Smith, M. W. (2014): Roughness in the earth sciences. *Earth-Science Reviews*, 136, 202-225. doi.org/10.1016/j.earscirev.2014.05.016

Stigter, E. E., Litt, M., Steiner, J. F., Bonekamp, P. N., Shea, J. M., Bierkens, M. F., & Immerzeel, W. W. (2018). The importance of snow sublimation on a Himalayan glacier. *Frontiers in Earth Science*, 6, 108. doi.org/10.3389/feart.2018.00108

Tarboton D.G., Luce C.H. (1996): Utah energy balance snow accumulation and melt model (UEB) computer model technical description and users guide. Utah Water Research Laboratory and USDA Forest Service Intermountain Research Station: 64 p.

Trubilowicz, J.W., Moore, R.D. (2017): Quantifying the role of the snowpack in generating water available for run-off during rain-on-snow events from snow pillow records. *Hydrological Processes*, 31: 4136– 4150. https://doi.org/10.1002/hyp.11310. doi.org/10.1002/hyp.11310